UNIVERSITY OF CALIFORNIA
RIVERSIDE

Excitation, Propagation, and Control of Spin Waves in Magnetic Micro- and Nanostructures

A Dissertation submitted in partial satisfaction
of the requirements for the degree of

Doctor of Philosophy

in

Electrical Engineering

by

Howard Chiang

September 2018

Dissertation Committee:
Dr. Alexander Khitun, Co-Chairperson
Dr. Alexander A. Balandin, Co-Chairperson
Dr. Jianlin Liu

The Dissertation of Howard Chiang is approved:

_____

_____

_____

Committee Chairperson

University of California, Riverside

Acknowledgments

Foremost, I would like to express my utmost gratitude to my PhD advisor, Dr. Alexander Khitun, for his guidance throughout my research at UCR. I was very fortunate to have his encouragement and support to complete my studies. Under his supervision, I was motivated to learn about systematic research, publishing, and networking in an environment that inspired me to succeed. Dr. Khitun provided me the opportunities to become involved with several symposiums and conferences to strengthen my research background. I hope to take what I learned from Dr. Khitun with me and continue to thrive in my career.

I would also like to extend my appreciation to Dr. Alexander A. Balandin for serving as a member of my dissertation committee. I was very fortunate to have him as my co-advisor and to be given the chance to collaborate with him on so many projects. It was my pleasure to participate in his research and cooperate with his group members throughout my time in the graduate program.

Additionally, I want to thank Dr. Jianlin Liu for serving as a member of my dissertation committee. He has enlightened me about my research interests since I was in my undergraduate program. I am really appreciative of the personal time he devoted to so many useful discussions and advice.

Furthermore, I would like to thank Dr. Michael Balinskiy and Dr. Mojtaba Ranjbar, as they held irreplaceable roles and made indispensable contributions to our group. They would share their valuable knowledge and laboratory skills, helping me

grow to be an independent researcher. Thank you for all your help during my graduate program, I had a great time working with you.

I could not forget to thank David Gutierrez, the best colleague to work with along the way. I am thankful for his assistance in software and for shaping me to become better in programming. It was you who made the research life more enjoyable and wonderful. Thank you for lighting up our lab.

I extend many thanks also to Dr. Guanxiong Liu, Dr. Fariborz Kargar, and Ruben Salgado from Dr. Alexander Balandin's group. They have always been friendly and very helpful when working together on projects. Additionally, I would like to give special thanks to Dr. Yadong Xu, Dr. Zhisheng Lin, and Dr. Chi Tang from Dr. Jing Shi's group, as well as Dr. Aleksey Volodchenkov from Dr. Javier Garay's group. I appreciate their assistance and fruitful discussions when I encountered problems during experiments. I would like to also thank Dr. John Butler and Dr. Nissim Amos. Without their help, I could not have had such smooth experiences working in the cleanroom. Thanks to their full support for providing an excellent fabrication environment at UCR.

Finally but not least, I want to express my sincerest gratitude to my family for their support and encouragement while I pursued my PhD. I could not have successfully finish my educational path without you. Thank you.

The text of this dissertation, in part or in full, is a reprint of the material as it appears in the following journals:

- Journal of Physics D: Applied Physics. Reprinted with permission from Serga, A. A. et al. YIG magnonics. J. Phys. D Appl. Phys. 43(26), 264002 (2010). Copyright 2018 IOP Publishing Ltd.
- Applied Physics Letters. Reprinted with permission from Au, Y. et al. Resonant microwave-to-spin-wave transducer. Appl. Phys. Lett. 100, 182404 (2012). Copyright 2018 AIP Publishing LLC.
- Physical Review Letters. Reprinted with permission from Chumak, A. V. et al. Bose-Einstein condensation of magnons under incoherent pumping. Phys. Rev. Lett. 102, 187205 (2009). Copyright 2018 by the American Physical Society.
- Journal of Applied Physics. Reprinted with permission from Kalarickal, S. S. et al. Ferromagnetic resonance linewidth in metallic thin films: Comparison of measurement methods. J. Appl. Phys. 99(9), 093909 (2006). Copyright 2018 AIP Publishing LLC.
- Journal of Applied Physics. Reprinted with permission from Ordonez-Romero, C. L. et al. Mapping of spin wave propagation in a one-dimensional magnonic crystal. J. Appl. Phys. 120(4), 043901 (2016). Copyright 2018 AIP Publishing LLC.
- Journal of Applied Physics. Reprinted with permission from Smith, K. R. et al. Spin wave propagation in spatially nonuniform magnetic fields. J. Appl. Phys. 104(4), 043911 (2008). Copyright 2018 AIP Publishing LLC.

- IEEE Transactions on Magnetics. Reprinted with permission from Demidov, V. E. et al. Magnonic waveguides studied by microfocus Brillouin Light Scattering. IEEE Trans. Magn. 51(4), 0800215 (2015). Copyright 2018 IEEE.
- Applied Physics Letters. Reprinted with permission from Chumak, A. V. et al. Spin-wave propagation in a microstructured magnonic crystal. Appl. Phys. Lett. 95(26), 262508 (2009). Copyright 2018 AIP Publishing LLC.
- Applied Physics Letters. Reprinted with permission from Bauer, H. G. et al. Coupling of spinwave modes in wire structures. Appl. Phys. Lett. 104(10), 102404 (2014). Copyright 2018 AIP Publishing LLC.
- Applied Physics Letters. Reprinted with permission from Chumak, A. V. et al. Direct detection of magnon spin transport by the inverse spin Hall effect. Appl. Phys. Lett. 100(8), 082405 (2012). Copyright 2018 AIP Publishing LLC.
- Nature Communications. Reprinted with permission from Collet, M. et al. Generation of coherent spin-wave modes in yttrium iron garnet microdiscs by spin-orbit torque. Nat. Commun. 7, 10377 (2016). Copyright 2018 Springer Nature Limited.
- IEEE-NANO. Reprinted with permission from Zografos, O. et al. Design and Benchmarking of Hybrid CMOS-Spin Wave Device Circuits Compared to 10nm CMOS. 2015 IEEE-NANO, p.686-689 (2015). Copyright 2018 IEEE.

- Nature. Reprinted with permission from Rugar, D. et al. Single spin detection by magnetic resonance force microscopy. Nature, 430 (2004). Copyright 2018 Springer Nature Limited.
- Physical Review B. Reprinted with permission from Klein, O. et al. Ferromagnetic resonance force spectroscopy of individual submicron-size samples. Phys. Rev. B. 78(14), 144410 (2008). Copyright 2018 by the American Physical Society.
- Nature Materials. Reprinted with permission from An. T, et al. Unidirectional spin-wave heat conveyer. Nat. Mater. 12 (2013). Copyright 2018 Springer Nature Limited.
- Scientific Reports. Reprinted with permission from Jamali, M. et al. Spin wave nonreciprocity for logic device applications. Sci. Rep. 3, 3160 (2013). Copyright 2018 Springer Nature Limited.
- Physical Review Letters. Reprinted with permission from Covington, M. et al. Time resolved measurement of propagating spin waves in ferromagnetic thin films. Phys. Rev. Lett. 89(23), 237202 (2002). Copyright 2018 by the American Physical Society.
- Physical Review Letters. Reprinted with permission from Jungfleisch, M. B. et al. Large spin-wave bullet in a ferrimagnetic insulator driven by the spin Hall effect. Phys. Rev. Lett. 116(5), 057601 (2016). Copyright 2018 by the American Physical Society.

- Applied Physics Letters. Reprinted with permission from Cherepov, S. et al. Electric-field-induced spin wave generation using multiferroic magnetoelectric cells. Appl. Phys. Lett. 104(8), 082403 (2014). Copyright 2018 AIP Publishing LLC.
- AIP Advances. Reprinted with permission from Balinskiy, M. et al. Spin wave interference in YIG cross junction. AIP Adv. 7(5), 056633 (2017). Copyright 2018 AIP Publishing LLC.
- Journal of Applied Physics. Reprinted with permission from Balinskiy, M. et al. Spin wave excitation in sub-micrometer thick $Y_3Fe_5O_{12}$ films fabricated by pulsed laser deposition on garnet and silicon substrates: A comparative study. J. Appl. Phys. 122(12), 123904 (2017). Copyright 2018 AIP Publishing LLC.
- Journal of Magnetism and Magnetic Materials. Reprinted with permission from Gutierrez, D. et al. Magnonic holographic imaging of magnetic microstructures. J. Magn. Magn. Mater. 428 (2017). Copyright 2018 Elsevier B. V.
- Scientific Reports. Reprinted with permission from Balinskiy, M. et al. Magnetoelectric Spin Wave Modulator Based On Synthetic Multiferroic Structure. Sci. Rep. 8, 10867 (2018). Copyright 2018 Springer Nature Limited.

Dedication

To all my family members.

謹以此文獻給我所有的家人。

ABSTRACT OF THE DISSERTATION

Excitation, Propagation, and Control of Spin Waves in Magnetic Micro- and Nanostructures

by

Howard Chiang

Doctor of Philosophy, Graduate Program in Electrical Engineering
University of California, Riverside, September 2018
Dr. Alexander Khitun, Co-Chairperson
Dr. Alexander A. Balandin, Co-Chairperson

The anticipated end of Moore's law has accelerated the exploration and development of new approaches to more scalable and more functional logic devices that consume less power. Of the promising technologies that have emerged, magnon spintronics is innovative for its use of magnetic excitation called spin waves. There are several appealing properties inherent in spin waves. For instance, the spin wave can exhibit nanometer wavelengths and micrometer travel distances. This advantage brings spin-based devices with scalability, which can be a substitute and continues the trend of Moore's law for minimal sized devices. Importantly, spin waves provide Joule-heat-free transfer of information, since the spins do not involve the motion of electrons. This property can prevent excessive energy consumption compared to CMOS. Also, because spin wave devices utilize phase in addition to amplitude, their operations are based on

vectors instead of scalar variables, that makes spin waves devices more functional compared to the conventional digital circuitry.

I have dedicated myself to studying the excitation, propagation, and control of spin waves in magnetic micro- and nanostructures. This dissertation is based on my published works, where I contributed to make spin wave devices based on $Y_3Fe_5O_{12}$ (YIG) structures, as well as on more recent results based on $Ni_{80}Fe_{20}$ (Py) nanostructures. YIG and Py are the best materials for prototyping spin wave devices. YIG is an excellent material for building spin wave-based devices because of its extremely low magnetic damping and its status as an insulator. Then, I give results based on $Ni_{80}Fe_{20}$ (Py) nanostructures. Py has relatively low spin wave damping among conducting materials and is compatible with CMOS technology. Investigation of spin waves in Py nanostructures is expected to lead to the building of scalable and multi-functional devices with capabilities far beyond the scaled CMOS. In this dissertation, I presented spin wave excitation and propagation in magnetic ferrimagnetic and ferromagnetic materials, as well as innovative structural design and spin wave controls for novel applications. I believe this dissertation will contribute greatly to the community.

Contents

List of Figures

List of Tables

`

Chapter 1. Introduction

Magnon spintronics is an active, emergent field that could deliver a number of breakthrough developments towards applications in data processing in the near future [1]. I have been dedicated to exploring the physical properties of magnons in micro- and nanostructures and novel applications of spin wave-based devices. My research contributes to the spintronics community's hope of driving the research in spin waves forward and of inspiring new applications of use.

1.1. Background

A spin wave is a collective oscillation of spins in a lattice around the direction of magnetization. Spin waves appear in magnetically ordered structures, and a quantum of the spin wave is referred to as a magnon. The existence of spin waves was predicted by F. Bloch in 1929 and the term spin wave was used to refer to the collective excitations of the electron spin system in ferromagnetic metals and insulators. The wide variety of linear and nonlinear spin-wave phenomena boosted interest in the spin wave's fundamental properties while spin waves in the GHz frequency range were of great interest for applications in telecommunication systems and radars. Today, spin waves are considered potential data carriers for computing devices, as they may have nanometer wavelengths, can be in the low-THz frequency range, provide Joule-heat-free transfer of

`

spin information over macroscopic distances, and give access to wave-based computing concepts [1].

Two general types of interactions of couple electron spins define spin-wave's characteristics: strong but short-distance exchange interactions and relatively weak long-range dipole-dipole interactions. The waves with short wavelength λ (roughly, $\lambda < 1$ μm), whose properties are mostly governed by the exchange interaction, are named exchange spin waves. Correspondingly, the long-wavelength waves are named dipolar or magnetostatic waves (MSWs). Owing to the inherent anisotropy of the dipolar interaction, MSWs are classified according to the angle between the spin-wave wavevector $\boldsymbol{k}$ and the saturation magnetization $\boldsymbol{M}$. In an in-plane magnetized magnetic film, waves propagating along and transverse to $\boldsymbol{M}$ are named backward volume magnetostatic waves (BVMSWs) and magnetostatic surface waves (MSSWs, also known as Damon-Eshbach waves), respectively [2]. Dipolar waves in a normally magnetized film are called forward volume magnetostatic waves (FVMSWs). Historically, most of the magnon-based devices for microwave signal processing operate with dipolar spin waves, which can be excited and detected rather conveniently by inductive antennas [3, 4].

Hereafter, we consider the dipole-dipole magnetostatic spin waves in thin-film waveguides. It is important to stress that the word magnetostatic is used here simply to indicate that the waves present solutions to Maxwell's equations with a magnetostatic approximation, which assumes negligible displacement current and a spin-wave

`

wavelength significantly shorter than that of an electromagnetic wave of the same frequency [5].

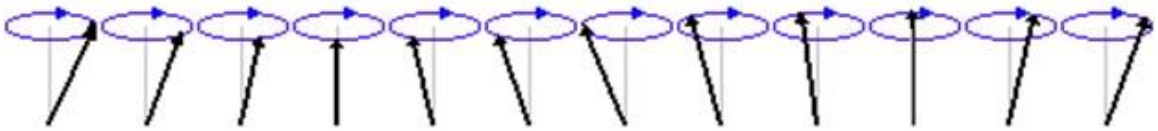

Figure 1 – An illustration of the precession of a spin wave over a wavelength. [6]

Magnetostatic waves can be defined as the regime in which the magnetic fields B and H have no time dependence, and can be derived from Maxwell's equation [2]:

$$\nabla \times H = \frac{4\pi}{c} J_{free} + \frac{1}{c} \cdot \frac{\partial D}{\partial t} \tag{1}$$

The free currents flow in closed loops, and that implies $\nabla \cdot J_{free} = 0$. Considering that there are no electric fields or boundary conditions to take into account, a good approximation of the magnetostatic spin waves results in:

$$\nabla \times H = 0 \tag{2}$$

Suppose a magnetic field lies in z direction, the magnetization would be [2]:

$$M = M_0 i_z + m e^{i\omega t} \tag{3}$$

Where M_0 is saturation magnetization with unit vector i in z direction, and m is the RF component of magnetization with x, y, z, components. Similar to magnetization, the magnetic field can be shown as [2]:

$$H = H_0 i_z + h e^{i\omega t} \tag{4}$$

`

In equation (4), *h* is the RF component of the magnetic field and has x, y, z components. Therefore, one can derive the equation of motion of the magnetization [2]:

$$\frac{dM}{dt} = \gamma(M \times H) \tag{5}$$

Finally, with properly defined boundary conditions and use of equation (5), the dispersion relation curves of magnetostatic spin waves corresponding to different magnetic field orientations will be obtained.

Forward volume magnetostatic spin waves (FVMSWs) are associated with a magnetic waveguide magnetized normally to its surface, perpendicular to the direction of spin-wave propagation. The dispersion curve for FVMSW is shown in **Figure 2**(A). The spin-wave frequency as the wavenumber *k* tends to zero and tends to the value $f_H = \gamma H_0$, where H_0 is the effective internal field (with the geometrically dependent demagnetizing field taken into account) and γ = 2.8 MHzOe^{-1}, the electron gyromagnetic ratio. With increasing *k*, the spin-wave frequency tends to:

$$f_1 = \sqrt{f_H(f_H + f_M)} \tag{6}$$

where

$$f_M = 4\pi\gamma M_0 \tag{7}$$

and M_0 is the saturation magnetization. The slope of the curve is determined mostly by the film thickness. An important and distinguishing feature of FVMSW is the invariance of their dispersion with direction of propagation in the plane of the film, which can easily be understood from the fact that the waves always propagate normally to the bias field.

`

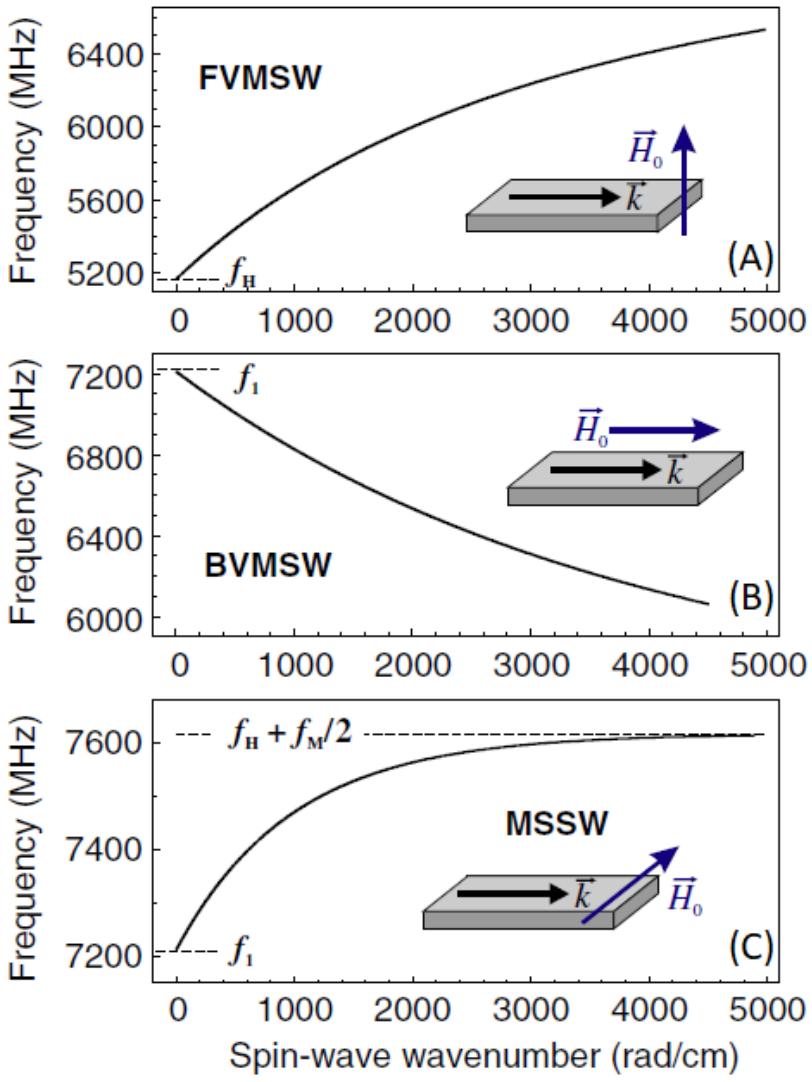

Figure 2 – (A) Forward volume magnetostatic spin wave (FVMSW) geometry. (B) Backward volume magnetostatic spin wave (BVMSW) geometry. (C) Magnetostatic surface spin wave (MSSW) geometry. Calculated dispersion relation using formula (8)-(10) corresponds to FVMSW, BVMSW, and MSSW, respectively. d_0 = 0.5 um, $4\pi M_0 = 1750\ Oe$, and $H_0 = 1845\ Oe$. [5] *J. Phys. D: Appl. Phys.* 43(26), 264002 (2010), with the permission of IOP publishing.

A useful approximation of the FVMSW dispersion relation is given by:

$$f_{FVMSW} = \sqrt{f_H\left(f_H + f_M\left(1 - \frac{1 - exp(-kd_0)}{kd_0}\right)\right)} \tag{8}$$

`

This expression is used to calculate the curve of **Figure 2**(A). Two different MSW mode-types can be excited in a thin film waveguide magnetized in-plane: backward volume magnetostatic waves (BVMSW), associated with propagation direction parallel to the applied bias field, and magnetostatic surface spin waves (MSSW) which occur when the bias field is perpendicular to the propagation direction. The dispersion curve for BVMSWs is shown in **Figure 2**(B) and can be approximated by:

$$f_{BVMSW} = \sqrt{f_H \left(f_H + f_M \frac{1 - \exp(-kd_0)}{kd_0} \right)} \tag{9}$$

The curve has the appearance of a mirrored version of the FVMSW characteristic: spanning the region between f_1 and f_H. Like FVMSW, BVMSWs are volume modes. This means that the amplitude of the magnetization precession has a cosinusoidal distribution across the film thickness. The main peculiarity of BVMSWs is the negative slope of their dispersion curve, and consequently the negative group velocity $v_{gr} = \partial f / \partial k$. The unusual physics of BVMSWs imply that the phase and group velocities of the waves are counter-propagating and that an increase in *k* is associated with a decrease in wave frequency [5].

Unlike backward and forward volume waves, magnetostatic surface spin waves (MSSWs) are localized to one surface of the film in which they propagate. The distribution of precessional amplitude across the film thickness is exponential, with a maximum at one surface of the film. For the particular orientation of the bias magnetic field and the MSSW propagation direction shown in **Figure 2**(C), this maximum is located

`

on the upper film surface. It can be switched to the lower surface by reversal (i.e. a 180° rotation) of either the field or the propagation direction. The dispersion curve for MSSW is shown in **Figure 2**(C), calculated using the formula:

$$f_{MSSW} = \sqrt{\left(f_H + \frac{f_M}{2}\right)^2 - \left(\frac{f_M}{2}\right)^2 exp(-2kd_0)} \quad (10)$$

In the small wavenumber limit, the spin-wave frequency is the same as that of BVMSW and is equal to equation (6), the ferromagnetic resonance frequency (FMR) for the film magnetized in-plane. With increasing *k*, the MSSW frequency tends to the value $f_H + f_M/2$ [5].

It should be noted that in **Figure 2**, the dispersion relationships are shown for the lowest (uniform) thickness modes. Higher-order thickness modes having nonuniform amplitude distribution across the film thickness are described by other dispersion laws, but are not so important for this review since they generally have lower excitation efficiencies. All three classes of waves may be excited in a thin-film waveguide [5].

Early spin wave were studies were focused mainly on MSSW and FVMSW [5], largely if not exclusively for practical reasons. It is technically much more straightforward to realize homogeneous bias magnetic fields oriented in the out-of-plane and transverse directions relative to a long, thin-film section, compared with along its axis. However, over the last decade, as experimental techniques have matured, interest in BVMSW has grown significantly [5]. In addition to being the most technically demanding, BVMSWs are in many ways the most interesting class of spin waves to

`

study, owing to their unique dispersion characteristics and nonlinear properties. Recently, attention has been given to short wavelength spin waves with properties influenced not only by the dipolar interaction, but by exchange. These waves, termed dipole exchange spin waves (DESW), have been the subject of several detailed studies [7, 8]. Dipole-dipole waves are defined when wavevector *k* is approximately less than $10^5\ cm^{-1}$. Because the device's structural dimensions provide a relatively small wavevector, most of my work has been in studying dipole-dipole waves.

1.2. Spin Wave Spectroscopy: Experimental Techniques for Spin Wave Excitation and Detection

Different techniques for spin wave excitation and detection can be broken down into a few categories: microwave techniques, optical techniques, spintronic based approaches, and others. **Table 1** summarizes the most widely used techniques [9].

`

	Techniques	Function	Features	Ref.
Microwave techniques	Conventional microstrip antenna based approach	Excitation, detection	Coherent excitation, high sensitivity, phase control, high frequency resolution	[5], [9], [10]
	Contactless antenna based approach	Excitation, detection	Simplified design without wiring, access to short-wavelength magnons	[11], [12]
	Parametric pumping technique	Amplification, excitation	Access to large magnon densities and short-wavelength magnons	[13], [14]
	Pulsed inductive microwave magne-tometer (PIMM)	Excitation, detection	Excitation of waves in a wide frequency range	[15], [16]
	Inductive magnetic probe (IMP) technique	Detection	Spatial resolution, high time- and frequency resolution	[17], [18]
Optical tech.	Brillouin Light Scattering (BLS) spectroscopy	Detection	Space, frequency, time, phase, and wavenumber resolved measurements	[9], [19], [20]
	Magneto optical Kerr effect (MOKE) spectroscopy	Excitation, detection	Space, frequency, time, and phase resolutions	[21], [22]
Spintronic tech.	Spin pumping (SP) based technique detection	Detection	Direct conversion from DC, is especially efficient at the nanoscale	[23], [24]
	Spin transfer torque (STT) based technique	Amplification, excitation	Direct conversion from DC, is efficient at the nanoscale	[25], [26], [27], [28], [29]
Other techniques	Magneto-electric cells	Excitation, detection	High spatial resolution, highly-suitable for magnon logic	[9], [30]
	Magnetic resonance force microsc. (MRFM)	Detection	High spatial resolution	[31], [32], [33], [34], [35]
	Detection of magnon-induced heat	Detection	Major opportunities for fundamental studies	[5], [29], [36], [37], [38]

Table 1 – General spin wave excitation and detection techniques. The data are compiled from Refs. [5], [9]-[38].

In this Chapter, we describe the essence of these techniques and outline their advantages and limits.

`

1.2.1. Conventional Micro-Strip Antenna Based Approach

The first category is microwave techniques based on all-electrical measurements. **Figure 3** shows an example of experimental setup and results for BVMSW using the conventional micro-strip technique. This technique provides both excitation and detection of spin waves. The sample has two micro-strips as waveguides on top of the surface. A microwave signal is injected through the input antenna and generates an alternating Oersted magnetic field [5]. There are torques exerted only in the vertical component, which results in an increase in precessional amplitude above the thermal level [5]. Furthermore, spins precess under the antenna interacts with their nearest neighbors, creating spin wave propagation when proper conditions of field and frequency are met [5]. As for the detection of spin wave signals, it is the inverse of the excitation process; the detection process collects the induced AC current at the output antenna when the spin waves arrive [5]. In **Figure 3**A, one can see the micro-strip antennas are fabricated on the YIG/GGG sample. The spin waves are propagating in the same direction as the applied bias magnetic field, which means it is in BVMSW configuration. For instance, in the curve in **Figure 3**B, the high frequency limit on spin wave excitation is the FMR frequency f_1 [5], which can be calculated from equation (6).

`

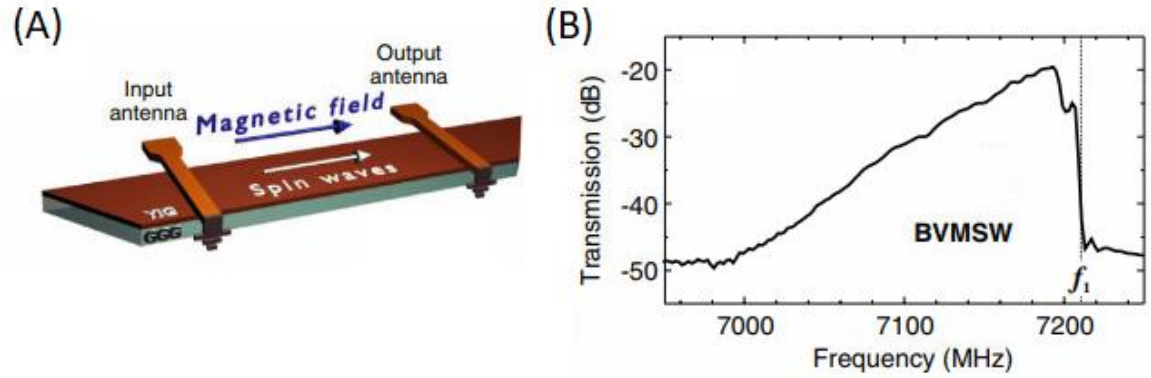

Figure 3 – (A) An illustration of BVMSW experimental setup. (B) Experimental results of BVMSW, showing transmission (S_{21}) spectrum signals. The bias magnetic field is at 1845 Oe. [5] *J. Phys. D: Appl. Phys.* 43(26), 264002 (2010), with the permission of IOP publishing.

Moreover, the maximum of the transmitted signal corresponds to spin waves in the limit $k \rightarrow 0$, meaning that with decreasing frequency (equivalent to increasing the wavenumber), the intensity of the transmitted signal decreases [5]. In conclusion, although this technique exhibits outstanding features such as coherent excitation, high sensitivity, phase control, and high frequency resolution, it requires conducting materials to be isolated from antennas with an extra layer of insulator.

1.2.2. Contactless Antenna Based Approach

From **Figure 4**, we can see an illustration of the contactless antenna technique. Due to the challenges of dealing with multiple impedance matched with electrical currents, wireless delivery of microwave signals to required locations is an attractive strategy [11]. The main idea is based on propagating spin wave excitation in which a uniform FMR

`

based antenna couples to free space microwaves, and then converts them into finite wavelength spin waves propagating in stripe magnonic wavelengths [12].

To perform spin wave excitation with this technique, there are some general steps to be followed. The device is prepared with multiple magnetic wires as transducers and placed on top of strip magnonic waveguides as sources of spin wave, consists of functional architecture of magnonic waveguides [11]. Next, each transducer generates a rotating magnetic field from dynamic magnetic charges induced on its surface. This results in a "magnonic chip" with a global uniform microwave field of wavelength that is much longer than the chip's dimensions [11]. The field drives multiple transducers that are in different locations into uniform precession, and the localization enables the coupling of the stray field to spin waves of short wavelength [11].

Once the spin wave is excited, time-resolved scanning Kerr microscopy (TRSKM) can be used for the spin wave signal detection [11]. Since the spatial resolution of the TRSKM technique is limited by the spot size of an optical instrument, it is better to perform the measurements by scaling up the physical sizes of the waveguide and transducer for longer spin wave excitation wavelengths [11].

`

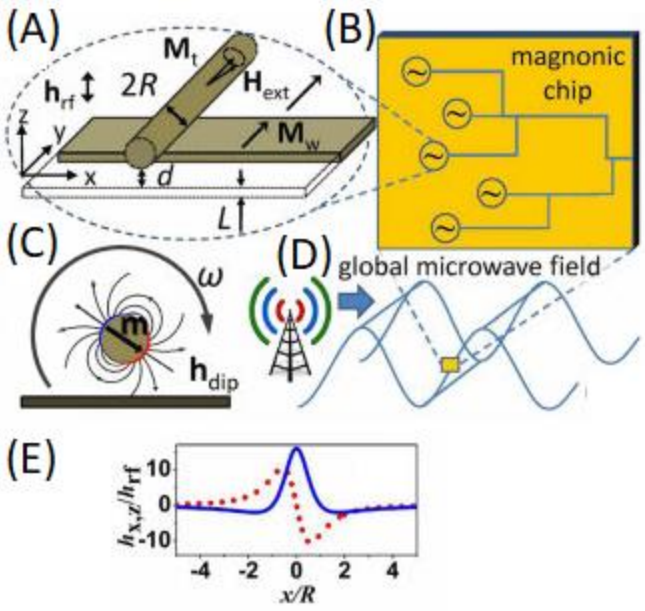

Figure 4 – (A) Schematic of transducer, which is one of the sources of spin waves. (B) A magnonic chip that has multiple spin wave sources. (C) The rotating magneto-dipole field induced by the magnetization precessing in the magnonic transducer. (D) An illustration that a magnonic chip is within microwave signals. (E) The spatial profiles of the magneto-dipole field produced by the x and z components of magnetization of the transducer on the waveguide top surface for d = 0. The x and z components are shown by a blue solid line and red dotted line, respectively. [11] *Appl. Phys. Lett.* 100, 182404 (2012), with the permission of AIP publishing under CC BY license, link: https://creativecommons.org/licenses/by/4.0/

1.2.3. Parametric Pumping Technique

Next, we consider the parametric pumping technique, where spin waves are excited within a dielectric resonator with some resonance frequency [13]. This technique is used for spin wave amplification and excitation. It provides access to large magnon densities and short-wavelength magnons. However, this technical approach does not suffice all implementations, due to the scale-dependent nature of a mechanical or electromechanical amplifier's dynamic range [39].

`

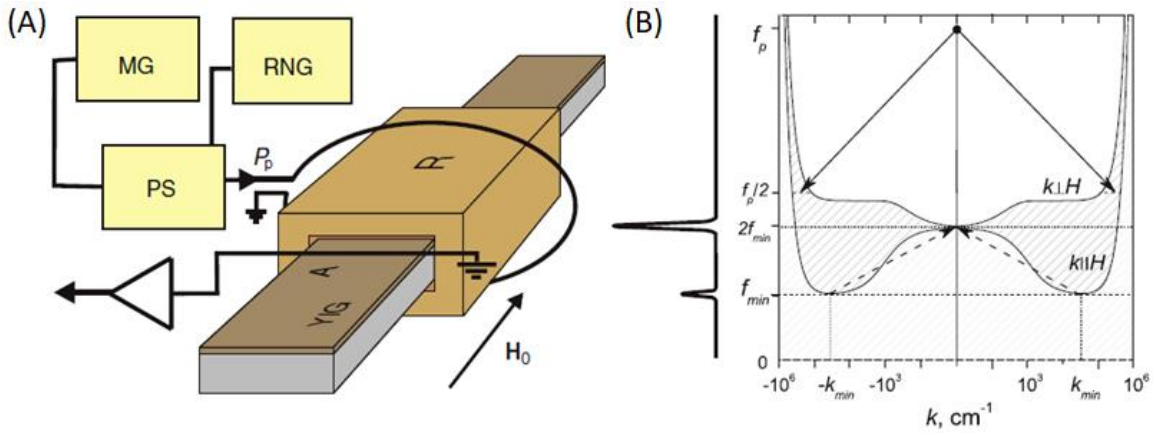

Figure 5 – (A) Schematic of experimental setup. A microwave generator (MG) sends pulses of input, while a phase shifter (PS) is controlled by a random number generator (RNG). A dielectric resonator (R) gets signals from microwave sources and an antenna (A) is used for detection signals. (B) The left part shows the signal spectrum detected by the antenna. The right part shows the magnon spectrum, with solid lines representing the parametric pumping process and the dashed line representing the confluence of the magnons from the bottom of the spectrum. [14] ***Phys. Rev. Lett.*** **102, 187205 (2009), with the permission of APS publishing.**

An example of setup is shown in **Figure 5**A. The microwave magnetic field is parallel to the magnetic field in order to achieve parallel pumping [14]. The YIG sample has an antenna placed on top of the surface as a waveguide. The microwave generator sends pulsed signals with a certain duration into the resonator. Next, the pulsed signals go through the antenna, which connects to the low-noise microwave amplifier. The detection of electromagnetic radiation is performed using the low-noise amplifier to strengthen the signal [14]. The phase shifter is controlled by the random number generator that randomizes the phase of the radiation, which determines the width of the frequency spectrum of the pumping power [14]. An experimental result is shown in **Figure 5**B, which shows the parametric pumping process and signal spectrum.

`

1.2.4. Pulsed Inductive Microwave Magnetometer

The main concept of the Pulsed Inductive Microwave Magnetometer (PIMM) technique is to use an excitation magnetic field transverse to the fixed static magnetic field in the form of pulses, then detect the response from the magnetization [15]. PIMM uses a broadband coplanar waveguide, and this strip line is used for both excitation and detection of spin waves [16]. The sample has a magnetic field applied in the direction of the strip line. Furthermore, the mutual inductance between the strip line and the sample ensures any change in the magnetization induces voltage in the strip line [16]. With the help of Fourier transform analysis, one can convert time domain to frequency domain and obtain linewidth from the profile [15]. An illustration of PIMM setup is shown in **Figure 6**. Additionally, the sensitivity of PIMM is constrained by the dynamic range of measurements. For instance, PIMM must be able to accept 10 V pulses from the pulse generator, while measuring inductive voltages in the range of tens of mV [40]. On the other hand, PIMM provides similar information as conventional measurement techniques while also offering several advantages [16]. First, PIMM has the capability to measure at lower frequency and field regimes, closer to the operating range for most technical devices [16]. Next, as opposed to the conventional FMR technique, the strip line geometry in inductive magnetometry allows for the measurement of the broadband of frequencies with one setup [16].

`

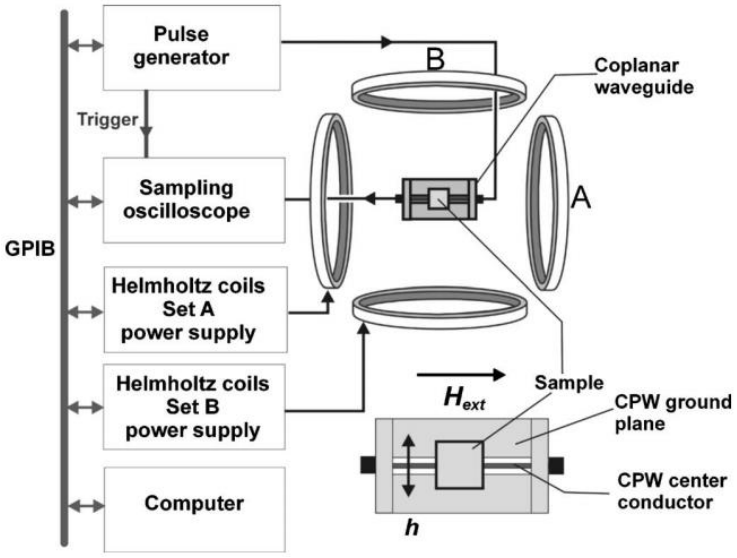

Figure 6 – A schematic of PIMM technique setup. A sample is placed on top of the coplanar waveguide (CPW) while the external magnetic field is applied in plane of the film. [15] *J. Appl. Phys.* 99(9), 093909 (2006), with the permission of AIP publishing.

1.2.5. Inductive Magnetic Probe Technique

The last technique in the microwave category is the Inductive Magnetic Probe (IMP) technique. This technique utilized a motorized magneto inductive probing system to map the energy of the spin waves in a magnonic crystal [17]. Based on Faraday's law of induction, the magneto-inductive probe consists of a wire forming a circular loop as a tip for detection [17]. First, a pulsed microwave is injected with the spatial profile of the pulses shorter than the magnonic crystal length and with no overlapping of pulses to achieve the propagating spin waves in the input antenna [17]. Then, detection is performed using the magneto-inductive probe and oscilloscope to obtain the temporal

`

profile of a transmitted pulse along the propagation path within the range of frequencies [17] An illustration of IMP technique setup is shown in **Figure 7**A.

Figure 7 shows an example of experimental results using the IMP technique. The color indicates the voltage induced in the inductive probe, with the red and blue colors representing the positive and negative induced voltages, respectively [18]. The dashed lines that show vertically and horizontally represent the slice of space and time, respectively [18]. The left box shows the spatial waveform for the vertical slice, and the top box shows the temporal waveform of the slice indicated by the horizontal line [18]. To further analyze the data, Fourier transform can be applied to either the vertical or horizontal slice in order to extract the peak that tells the wave number and the carrier frequency at a certain space and time [18]. Although this technique has the penetration depth limited < 1 cm, this technique provides remarkable spatial resolution, high time- and frequency resolution of spin waves [18].

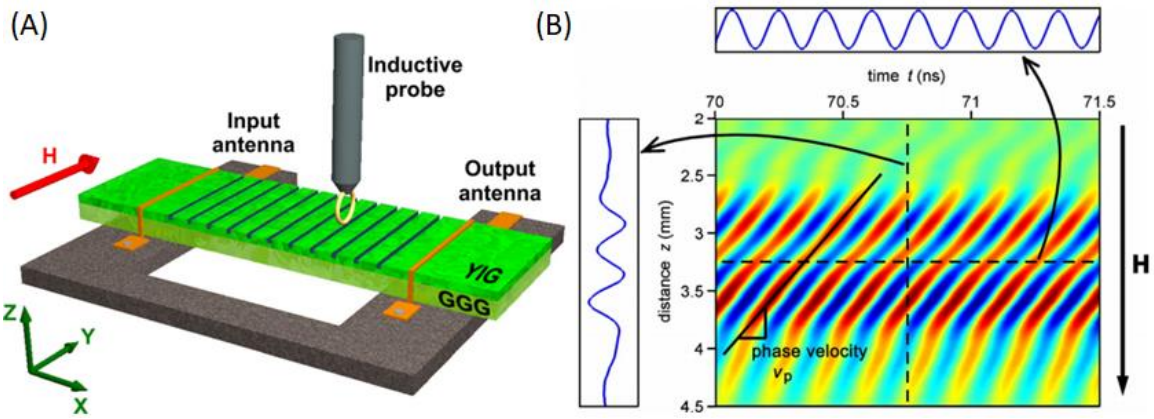

Figure 7 – (A) A schematic of experimental setup. The inductive probe is scanning the surface of the sample while the magnetic field is applied. (B) shows an example of an experimental result. [17, 18] *J. Appl. Phys.* 120(4), 043901 (2016), with the permission of AIP publishing. *J. Appl. Phys.* 104(4), 043911 (2008), with the permission of AIP publishing.

`

1.2.6. Brillouin Light Scattering Spectroscopy

The second category is based on optical instruments, and the first technique is called Brillouin Light Scattering (BLS) spectroscopy. BLS exhibits high sensitivity that permits the detection of thermal spin waves, which are naturally existing inside the ferromagnetic materials, and in addition to externally excited spin waves [41]. The general principle of BLS is based on the interaction between the magnon (quanta of spin waves) and photon [42]. In a general quantum mechanical point of view, the inelastic scattering mechanism as photon-magnon collision follows the total energy and momentum conservation law [41]. This leads to two phenomena: the Stokes process and the anti-Stokes process. The Stokes process is when energy is transferred from the photon to the spin wave to create magnon, while the anti-Stokes process is when energy is transferred from the spin wave to the photon which magnon is annihilated [42]. **Figure 8**A shows an example of BLS spectroscopy setup. Spin waves are excited while a microwave goes through striped antenna patterned above the magnonic waveguide (e.g. Py) [19]. The microwave current creates a local dynamic magnetic field, and couples to the magnetization of the magnonic waveguide. Then, a spin wave propagates from the striped region [19]. The detection process is achieved with the help of probing light interaction with the magnetization oscillations in the magnetic material, which causes phase modulation of the scattered light [19]. Next comes analysis of the collected BLS intensity, which is proportional to the intensity of magnetization oscillations at the

`

probing spot. The obtained intensity provides information about the characteristics of spin waves in the material [19].

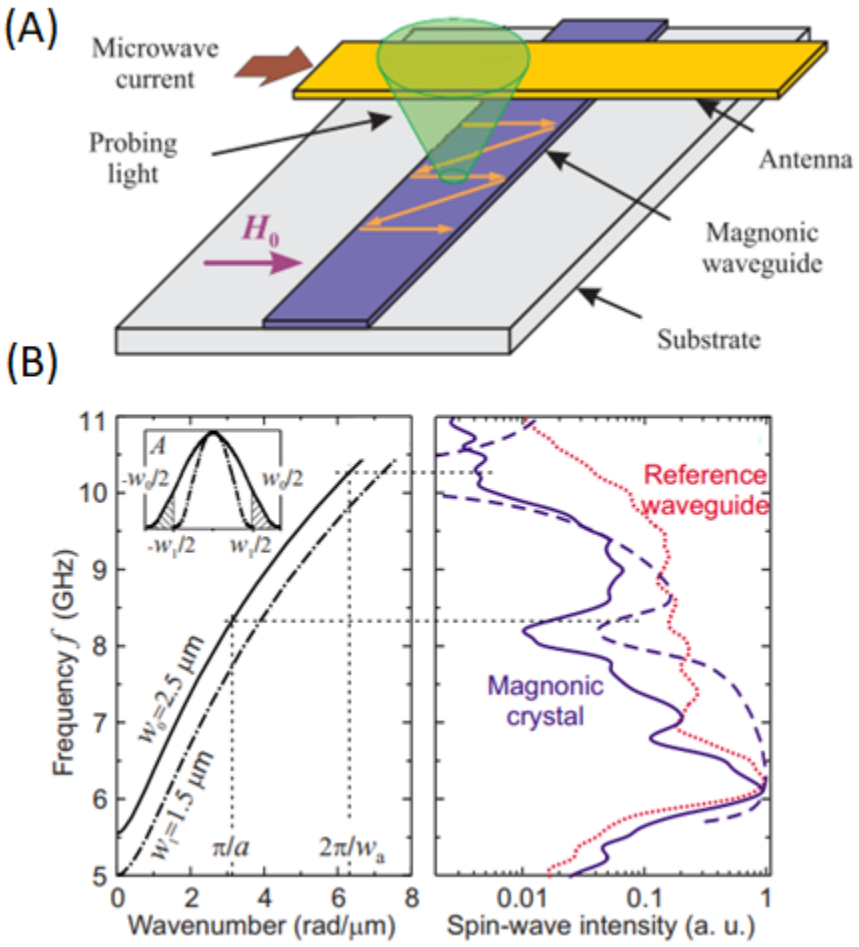

Figure 8 – (A) A schematic diagram of BLS spectroscopy setup. The spin waves are excited and the light source is pointed at the sample. (B) The left part shows the calculated spin wave dispersion curves. The right part shows normalized spin wave intensity of experimental results. [19, 20] ***IEEE Trans. Magn.*** **51(4), 0800215 (2015), with the permission of IEEE publishing.** ***Appl. Phys. Lett.*** **95(26), 262508 (2009), with the permission of AIP publishing.**

With the BLS spectroscopy technique, it is possible to obtain space, frequency, time, phase, and wavenumber resolved measurements [9]. **Figure 8**B shows an example of collected results. The experimental results are shown with a solid line, with spin wave

`

maximum intensity corresponding to spin waves with wavenumbers larger than $k = 0$ because of the highest excitation efficiency and the highest spin wave group velocity [20]. Therefore, as frequency increases, which leads to increasing wavenumbers, the excitation efficiency decreases [20]. Moreover, conventional BLS exhibits poor lateral resolution and the lack of phase sensitivity as major limitations [41]. Further development in experimental techniques such as micro and nano BLS spectroscopy will help attract more attention to studying spin waves at the nanoscale [19].

1.2.7. Magneto Optical Kerr Effect Spectroscopy

Another optical based technique is Magneto Optical Kerr Effect (MOKE) spectroscopy. In **Figure 9**, the microwave is injected through a coplanar waveguide for spin wave excitation and then recorded by spatially scanning the magnetic sample under the objective lens with magnetic field applied, resulting in a measurement of spin wave dispersion relations [21]. In general, the MOKE starts with a diode pumped solid state laser at a certain operating wavelength – for example, $\lambda = 532$ nm [22]. For better stability, it is recommended to have the laser at high outputs and to use a half wave polarizer system and neutral density filters [22]. That way, the laser will be focused on the desired sample and get reflected onto the lens. Then, the laser passes through the objective lens and is adjusted until the focus spot has a sufficiently high central intensity without higher order modes [22]. Lastly, the laser is directed to photodiode for detecting signals.

`

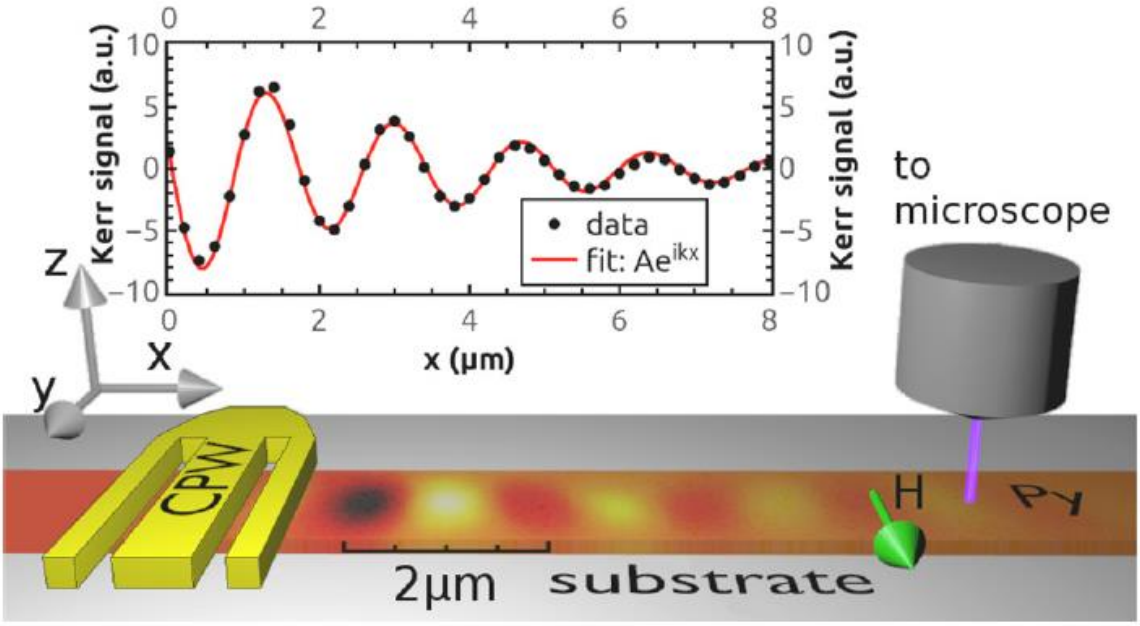

Figure 9 – The spatial map of an out-of-plane component of the dynamic magnetization with the MOKE system. A microwave current is injected through a coplanar waveguide and spin waves were generated with the help of a magnetic field. [21] *Appl. Phys. Lett.* 104(10), 102404 (2014), with the permission of AIP publishing.

Figure 9 also shows the experimental results collected by using the MOKE system. In the data, the spatial decay is extracted and fitted to an exponentially decaying wave, as shown in the inset [21]. Next, by performing this procedure as a function of microwave frequency for a fixed magnetic field applied perpendicular to the long axis of the Py substrate, the complex spin wave dispersion relation can be obtained [21]. Since MOKE is an optical based detection technique, the spot size of the laser may affect the sensitivity of measurements. Overall, MOKE allows users to obtain space, frequency, time and phase resolutions for spin waves.

`

1.2.8. Spin Pumping Based Technique Detection

The next category is spintronic approaches, the first technique of which is the Spin Pumping (SP) based technique for detection. This technique is one of the key mechanisms that allows the conversion of spin to be excited in ferromagnetic materials into electron carried spin current and charge current in an attached nonmagnetic metal layer [23]. Spin waves in spintronics can transfer a spin angular momentum over macroscopic distances because the spin wave free path has orders of magnitude larger than the spin diffusion length in metals [24]. The schematic of experiment setup is shown in **Figure 10**A. The YIG sample is magnetized with a magnetic field combined with a microwave going through a micro-strip antenna for spin wave excitation [23]. Then, the transmitted signals are detected at Pt layer and measured in AC and DC signals with the help of an oscilloscope [23]. AC signals represent as inductive microwave signals similar to detection using conventional micro-strip antennas, while DC signals represent Inverse Spin Hall Effect (ISHE) voltages [23]. The experimental setup was designed for time-resolved measurements to demonstrate magnon spin transport between the spatially separated inductive spin wave source and the ISHE detector [23]. **Figure 10**B shows the experimental results using the SP-ISHE technique. The results have both spin wave intensity (upper row) and ISHE voltage (lower row) for opposite directions of magnetic fields.

`

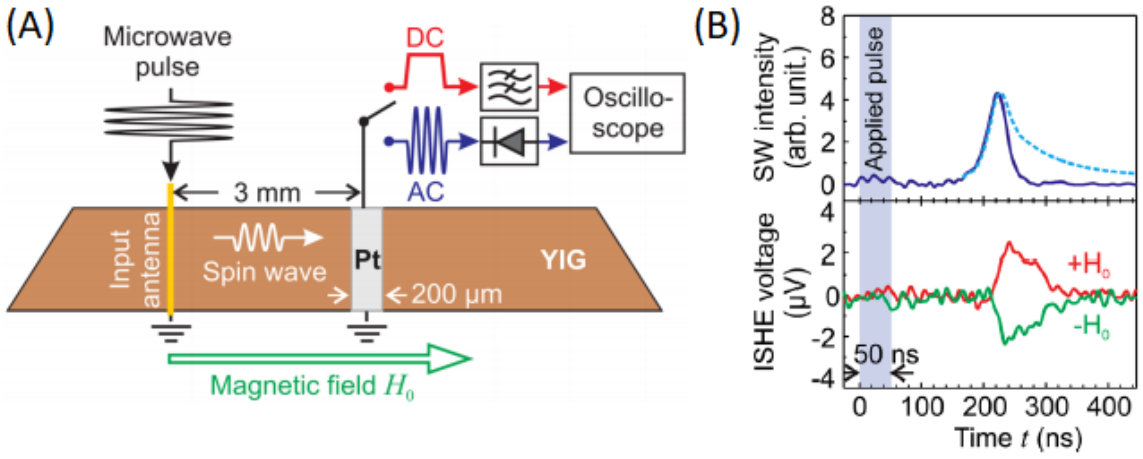

Figure 10 – (A) Schematic diagram of experimental setup. The Pt strip detects induced AC and ISHE DC signals. (B) Experimental results of SP-ISHE technique. In the top row, the solid lines are experimental data and dashed line is the calculated data. The bottom row has a red colored line, which shows a magnetic field applied in a positive direction, and a green colored line, which shows a magnetic field applied in a negative direction. [23] *Appl. Phys. Lett.* 100(8), 082405 (2012), with the permission of AIP publishing.

1.2.9. Spin Transfer Torque Based Technique

The Spin Transfer Torque (STT) based technique is another method for measurement of spin waves [9]. There have been many proposed methods for spin wave excitation and amplification with a spin torque based approach [25-29, 43]. For example, recent studies have shown that it is well established that a spin polarized electric current injected into a ferromagnetic layer through a nano-contact exerts a torque on the magnetization, leading to microwave frequency precession detectable through the magnetoresistance effect [25]. Although thermally excited magnons have attracted much attention, thermal excitation is a nonlinear and relatively slow process that does not have high fidelity transport or conversion of information [26]. One of the ideal methods for

`

magnonic devices operating with a linear response would be the use of the STT based technique.

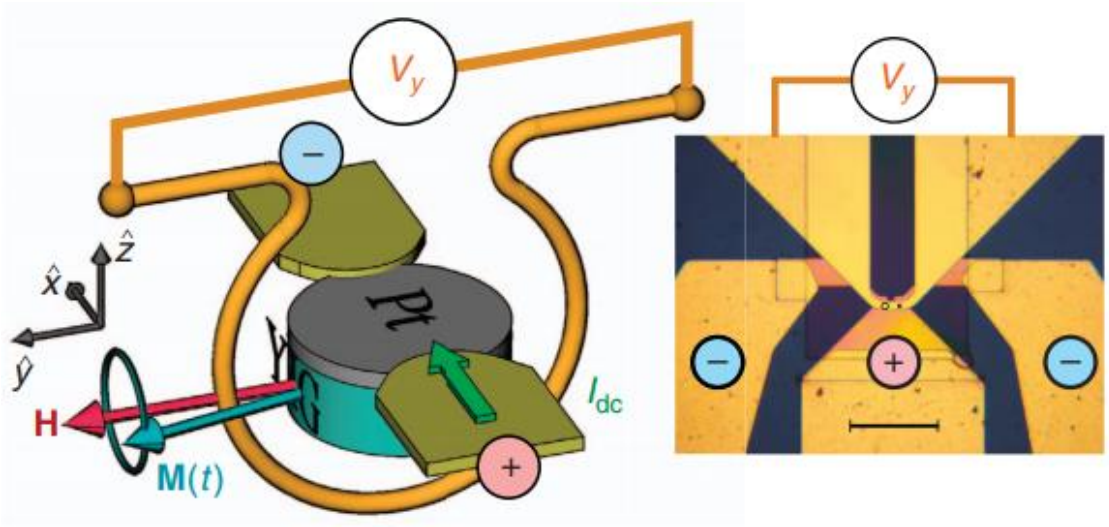

Figure 11 – Left: schematic design of experimental setup. The magnetic field is applied perpendicular to the DC current, which flows through the Pt layer. The inductive voltage is generated in the antenna by the precessing magnetization (M(t)) of YIG. Right: optical image of device. [27] *Nat. Commun.* 7, 10377 (2016), with the permission of Springer Nature publishing under CC BY license, link: https://creativecommons.org/licenses/by/4.0/

The STT technique utilizes charge current to transfer angular momentum to create spin currents in normal metals based on the Spin Hall Effect (SHE) [27]. Pt has a large spin Hall angle, which provides a high efficiency of producing spin currents [27]. The charge current flows through the plane and produces spin current flowing transversely to the plane (and the charge current). Then, the spin current is transferred through the interface with ferromagnetic metals, which gives coherent emission of spin waves [28]. Non-metals such as YIG are also suitable for this method [29]. **Figure 11** shows the Pt layer connected with electrodes for DC current injection with a microwave antenna around it for inductive coupling with the YIG magnetization [27]. The detection is

`

performed with a spectrum analyzer to see the voltage produced in the antenna by potential auto-oscillations of YIG as a function of DC current injected in the Pt layer while the magnetic field is applied [27]. Due to the Spin Hall Effect (SHE), the spins accumulated at the YIG and Pt interface, and spin transfer signal peaks can be observed [27].

1.2.10. Magneto-Electric Cells

The last category consists of several unique and remarkable techniques for spin wave excitation and detection. The first technique is called magneto-electric (ME) cells, a technique used for both excitation and detection purposes. The schematic of the ME cell is shown in **Figure 12**. The ferromagnetic material NiFe serves as a spin wave bus and is defined to have out-of-plane magnetic anisotropy, while the Ni layer has in-plane magnetic anisotropy [30]. The ME cell generates a spin wave by injecting RF voltage from the top contact layer into the piezoelectric layer (PE), which creates a strain that is introduced to the magnetostrictive layer (Ni) and is translated into the changes of magnetization. The inverse process enables the detection of spin waves. The spin wave propagates through the spin wave bus and reaches the Ni layer, in which the spin wave produces a strain that in turn is translated into voltage through the PE layer and is read out via the top contact layer [30]. As result, the transition of magnetization moving from the spin wave bus to the magnetostrictive layer can be achieved [30]. Moreover, the

`

magnetization of the magnetostrictive layer is bi-stable and can switch between two canted magnetization states [30].

One of the outstanding features using the ME cell for spin wave generation and detection is the ability to encode the information in the phase of the waves. The phase of the spin wave is dependent on the canted state, in which at state "0," the generated spin wave has a phase equal to 0, and at state "1," the spin wave has a phase equal to π [30]. Therefore, this technique provides high spatial resolution and is highly suitable for magnon logics [9]. Further description of the ME cell's operation and potential application will be discussed in Section 1.4.

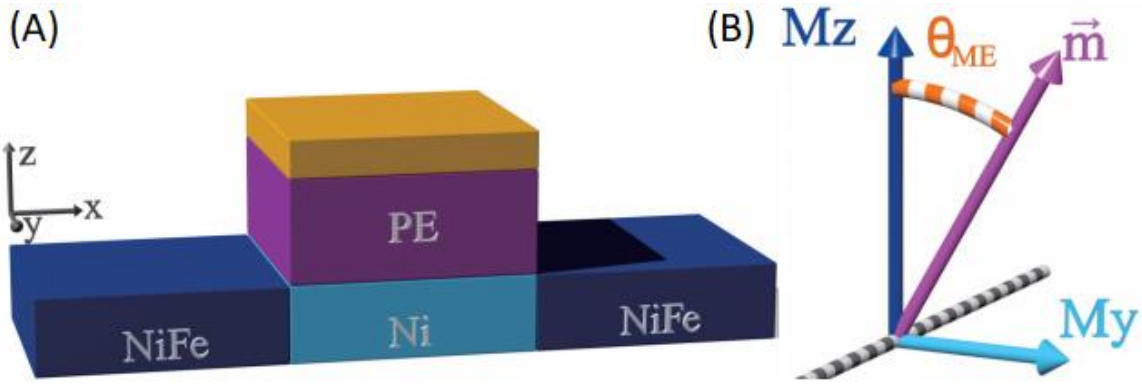

Figure 12 – (A) Schematic of ME cell. (B) An illustration of canted magnetization in the Ni layer of the ME cell. m is the canting of magnetization, and θ represents the phase differences of the titled magnetization. [30] ***2015 IEEE-NANO,*** **p.686-689 (2015), with the permission of IEEE publishing.**

1.2.11. Magnetic Resonance Force Microscopy

The next technique is Magnetic Resonance Force Microscopy (MRFM). This technique is similar to the magnetic resonance imaging (MRI) technique. Although MRI

`

is powerful for visualizing sub-scale structures with three-dimensional spatial resolutions, it has sensitivity limitation, so MRFM was proposed to overcome this detection limitation [31]. Achieving single spin sensitivity is challenging because the force from a single spin is extremely small [31]. Many studies have proposed the development of ultrasensitive cantilever based force sensors, a deeper understanding of spin relaxation processes, and the detection of polarization in spin ensembles [32-34].

The MRFM technique can be divided into three steps: excitation, detection, and imaging. **Figure 13** shows the experimental setup. The spin waves are produced with the micro-strip antenna that is underneath the sample, with microwave magnetic field input through the antenna [35]. As for detection, the concept is based on Magnetic Force Microscopy (MFM), which uses a magnetic tip for scanning and reads the reflection of the cantilever beam [35]. MRFM utilizes the magnetic force between a ferromagnetic tip and spins in the sample [31]. The difference between MRFM and conventional FMR techniques is that MRFM detects the static (longitudinal) components of magnetization only, components which have much longer relaxation time than others in the spin system [35]. Therefore, while conventional FMR measures absorb energy, MRFM measures store energy [35]. As for the imaging step, the advantages of MFM are incorporated through the spatial resolution, which is defined with the probe size [35].

`

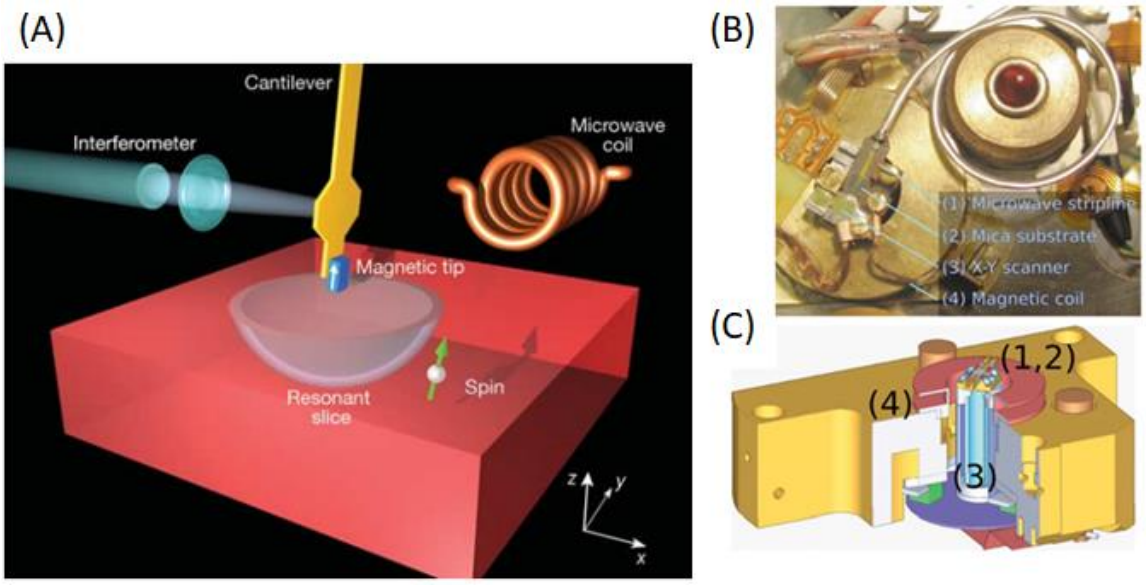

Figure 13 – (A) An illustration of MRFM setup. The magnetic tip is placed at the end of the cantilever and positioned 125 nm above the sample. The sample contains low density of electron spins for scanning. The resonant slice represents as the locations in the sample where magnetic fields from both the magnetic tip and external fields match with the resonance condition. (B) An actual MRFM design setup. (C) The cross-section view of MRFM design. [31, 35] ***Nature,*** **430 (2004), with the permission of Springer Nature publishing.** ***Phys. Rev. B.*** **78(14), 144410 (2008), with the permission of APS publishing.**

1.2.12. Detection of Magnon-Induced Heat

Detection of magnon-induced heat is one of the techniques that has opened routes for further research. Recent studies have explored heat and spin effects coupled by the dissipation and noise associated with magnetization dynamics, including, for instance, magnetic domain wall motion and spin waves [36, 37]. The experimental setup for this technique is shown in **Figure 14**. In **Figure 14**A, there is a polycrystalline $Y_3Fe_5O_{12}$ (YIG) placed on top of a microwave injected antenna [38]. The microwave frequency has been tuned to YIG disk's Damon-Eshbach mode (DEM) with the help of magnetic fields [38].

`

Due to the inhomogeneous microwave source, the top and bottom surface spin waves intensities are different, resulting in a plane spin current perpendicular to the external magnetic field [29]. In addition, as this current displaces the location of heat generation, the local temperature can be detected to indicate this effect [38]. For detection purposes, an infrared camera can be used for measuring temperature distribution on the YIG sample.

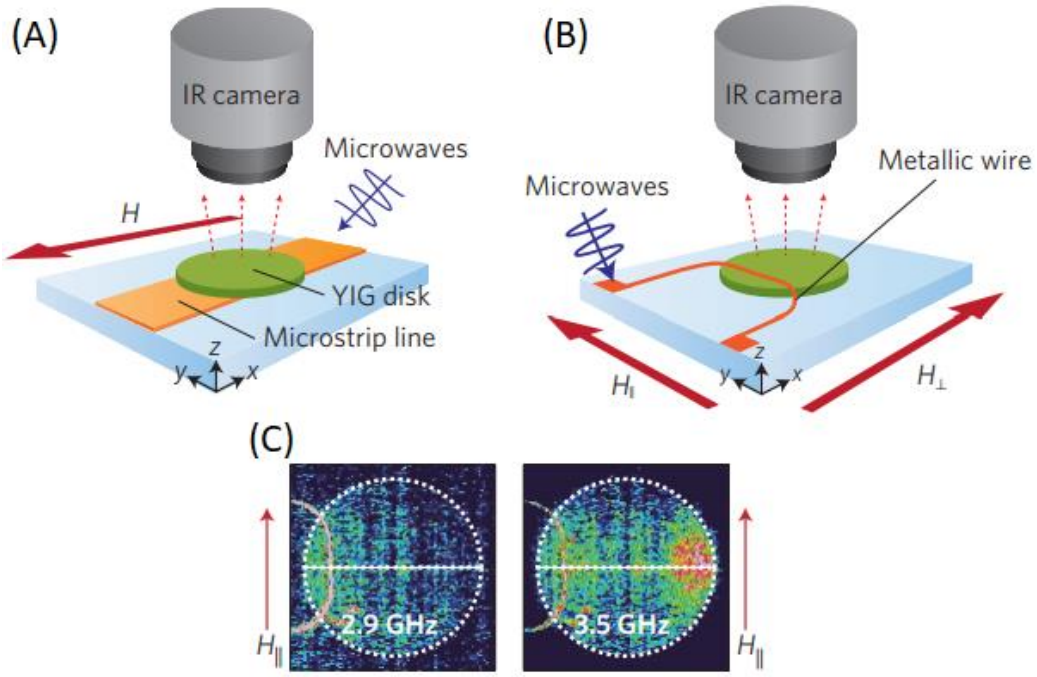

Figure 14 – (A) Schematic of experiment setup, using a magnetic field and a relatively large micro-strip line for spin wave excitation. An infrared camera is used for temperature detections. (B) A similar experimental setup for temperature distribution measurements, but using a smaller microwave antenna for spin wave generation. (C) Damon-Eshbach mode excitation geometry. The temperature distribution is shown in a color scale. [38] *Nat. Mater.* 12 (2013), with the permission of Springer Nature publishing.

For a better spin wave-induced heat conveyer effect in the YIG sample, it is good to use a local energy injection method by using relatively smaller antennas [5]. **Figure 14**B

`

shows this improved setup for the effect. With similar spin wave excitation as a previous experiment, the microwave is injected into the antenna while the magnetic field is applied. That way, the excited spin waves will propagate from the position of generation to the other side of the sample. The detection of temperature from the infrared camera shows that the location near the antenna of spin wave generation has a lower temperature than the other side of the sample. This means that there is a temperature gradient, indicating unidirectional spin wave propagation [38].

1.3. Spin Wave Spectroscopy: Time Domain and Frequency Domain Methods

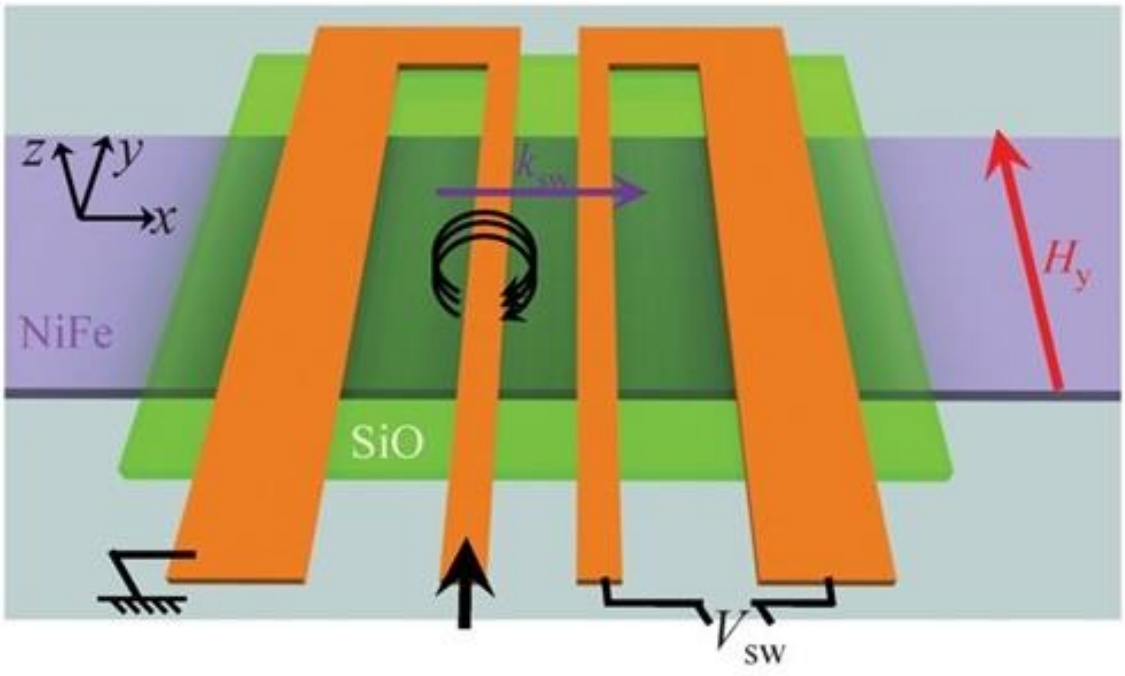

Figure 15 – Schematic illustration of the device structure. The striplines are in an asymmetric coplanar waveguide configuration. The bias magnetic field is applied in the y-direction and propagating spin wave in the x-direction is detected by the antenna using an inductive technique. [46] *Sci. Rep.* 3, 3160 (2013), with the permission of Springer Nature publishing.

`

The essence of spin wave spectroscopy is illustrated in **Figure 15**. Spin waves are excited and detected by a pair of microscale conductors (e.g., micro-antennas for transmission, or coplanar transmission lines for reflection) placed in the vicinity of the sample, such as NiFe (Py) thin film. These conductors are separated from Py with a layer of SiO_2, an insulator. An electric current passed through the input conductor generates a magnetic field around the current-carrying wires. This excites spin waves in the magnetic material under the resonant conditions corresponding to the propagating spin wave modes as illustrated in **Figure 2**. A propagating spin wave induces a disturbance of local magnetization and changes the magnetic flux from the sample. According to Faraday's law, the change of the magnetic flux creates an inductive voltage in the detector conductor loop. The magnitude of the inductive voltage is proportional to the rate of change of the magnetic flux. This approach has been applied for spin-wave transport study in a variety of magnetic micro- and nanostructures [44, 45].

There are two major types of measurements accomplished with the set of micro-antennas and associated with detection of the inductive voltage produced by the propagating spin waves in the time domain or in the frequency domain. The time domain method is illustrated in **Figure 16**. This method consists of an electromagnet for providing a uniform bias magnetic field, a source generator for the RF current input signal, and an oscilloscope for inductive voltage detection. The main concept of this method is to excite spin waves with pulsed magnetic fields from current carrying wires and to measure the dynamic magnetization by inductive voltage [44].

`

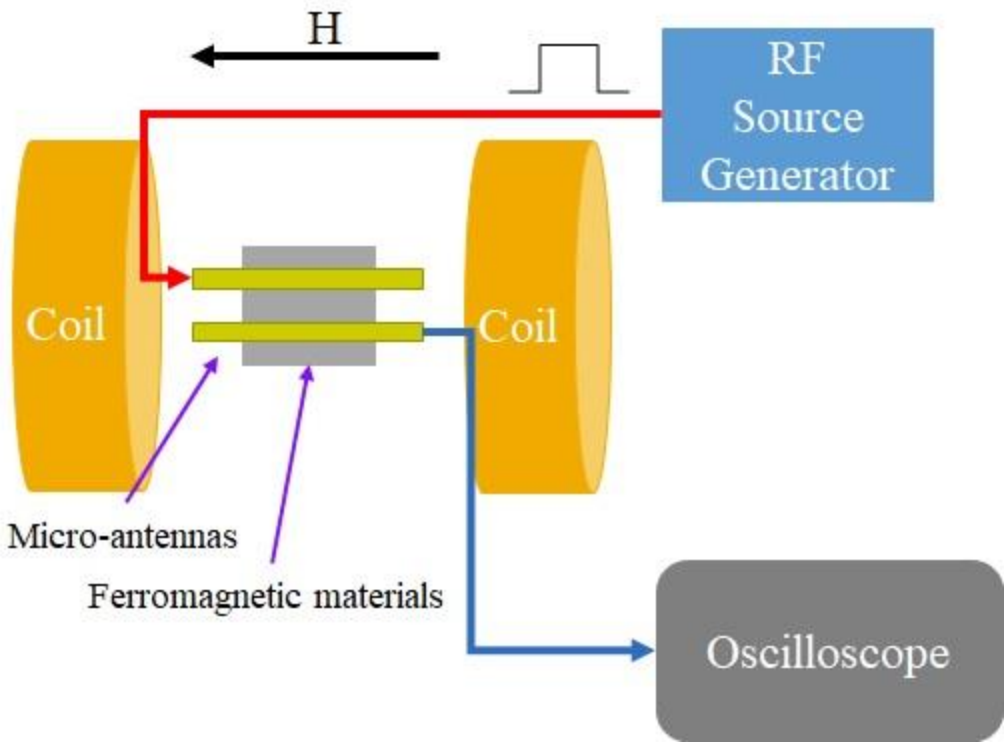

Figure 16 – Time domain method for spin wave excitation and detection. The setup consists of electromagnets, a RF source generator, and an oscilloscope. Spin waves are excited by injecting a pulse RF current through a micro-antenna, which results in magnetic flux variation. The changes of magnetic flux are measured as inductive voltages, and are detected by oscilloscope.

To begin the experiment, fabricate a set of micro-strip antennas on top of the sample for transmitting and receiving the signals, then place the sample in between the electromagnets for the uniform bias magnetic field. Next, send a pulsed RF signal from the source generator into the micro-strip antenna. The RF current will create a magnetic field around the current carrying wires. This created magnetic field will affect the magnetic material, resulting in magnetic disturbances. These disturbances will change the magnetic flux of the magnetic material and can travel distances that depend on the magnetic material's damping. As mentioned previously, changes in magnetic flux can be

`

detected by measuring the inductive voltage. An oscilloscope is connected to the detection antenna and is used for the inductive voltage measurements. At this point, the excitation and propagation of spin waves have been achieved.

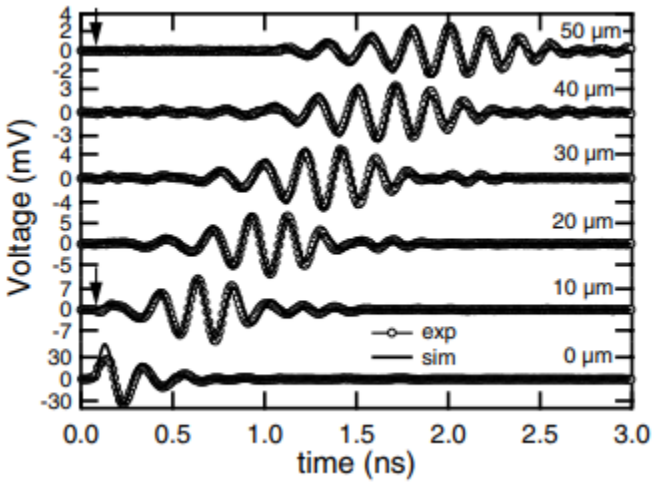

Figure 17 – An example of spin waves' response using the time domain technique. Inductive voltage is shown as a function of distance from the excitation waveguide for a sample with 100 nm NiFe, with magnetic field at 100 Oe. [44] *Phys. Rev. Lett.* 89(23), 237202 (2002), with the permission of APS publishing.

For confirmation of spin waves' response, **Figure 17** shows an example of the experimental result using the time domain method. The waveforms exhibit a delay before the magnetization begins to precess, with the delay time increasing as the separation of waveguides increases [44]. In addition, the rise time to reach maximum amplitude also increases with the increase of the separation of waveguides [44]. Therefore, based on these phenomena of spin waves, we can confidently conclude that there are spin wave excitation and propagation responses.

For the frequency domain method, the experimental setup is similar to the time domain method described previously. This experiment requires an electromagnet to

`

provide a uniform bias magnetic field and a network analyzer for injection and detection of RF signals. The network analyzer has two ports – port one (P1) is used to inject the signal, while port two (P2) is used to detect the signal. To prepare the sample, micro-strip antennas are fabricated on the sample.

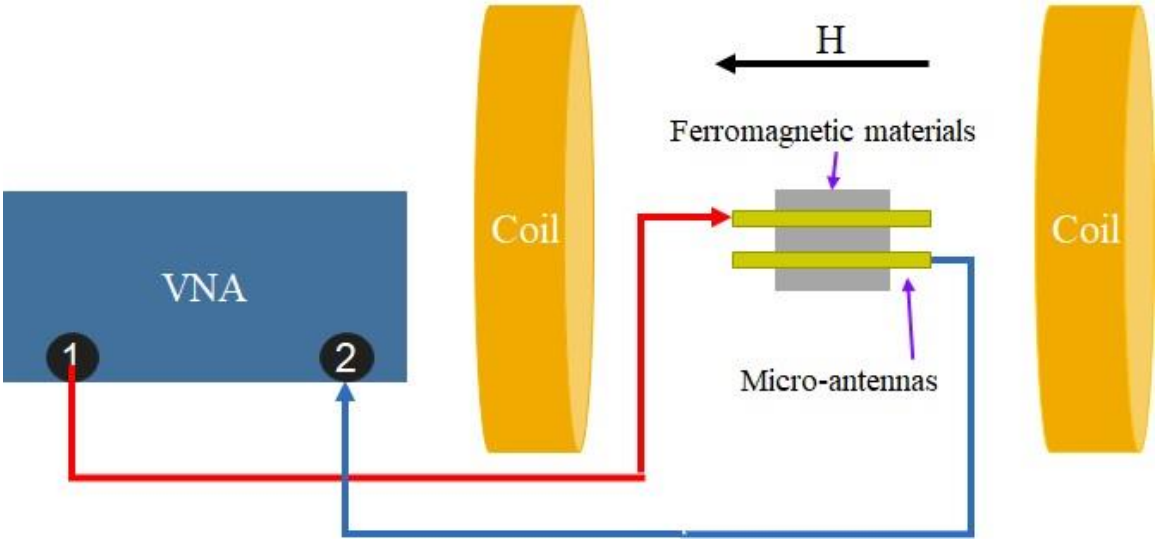

Figure 18 – Frequency domain method for spin wave excitation and detection. The experiment setup consists of electromagnets and a Vector network analyzer (VNA). Ferromagnetic material is placed in between electromagnets. Spin waves are generated by one of the micro-antennas (input antenna) connected to the VNA. In this MSSW configuration, the spin waves propagate perpendicular to the direction of external magnetic fields. Another micro-antenna is used for the detection of the inductive voltage.

Figure 18 shows the schematic of experimental setup using the frequency domain method. First, place the sample in between the electromagnets to apply the bias magnetic field, with the magnetic field sweeping in a range (e.g. -2000 Oe to +2000 Oe). Next, connect P1 of the network analyzer with one of the micro-strip antennas and inject the RF current through the wire. The network analyzer has the function of applying RF signal at a certain range of frequency. The spin wave will be excited at a frequency with a

`

corresponding magnetic field, and it will travel to the detection antenna, which is connected to P2 of the network analyzer. Finally, the network analyzer will display the collected results in decibels (dB) to represent the power ratio between the injected signal at input and the detected signal at output.

By extracting and plotting the collected data, the evidence of spin waves' excitation and propagation will be observed. **Figure 19** shows an example of plotted data for spin waves' response.

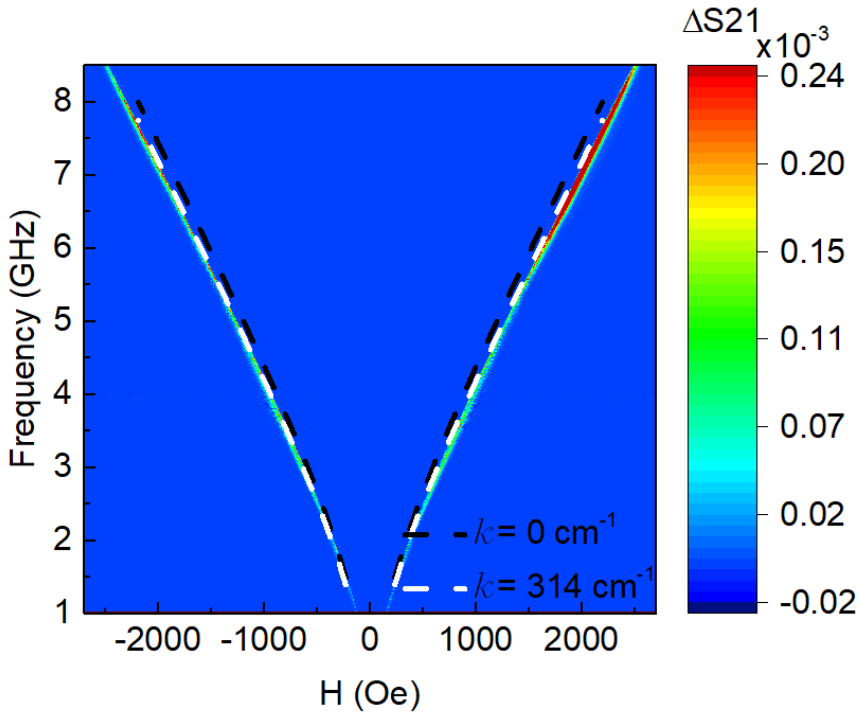

Figure 19 – Colormap of spin waves' response; the result is from the BVMSW configuration setup. The results of spin waves are represented in light blue and red colors. The experiment results are fitted with Kittel's formula at different mode *k*, shown in dashed white and black colors.

`

The colormap shows the x-axis with a range of magnetic fields while the y-axis has a range of frequencies. The light blue and red colors indicate the resonant frequencies at certain corresponding magnetic fields. The location of resonant frequency changes as the magnetic field changes. By fitting the spin waves' pattern (light blue and red colors) with Kittel's formula, we can confirm the existence of spin waves. Therefore, by using the frequency domain method, we have solid proof of spin waves' excitation and propagation.

In summary, there are many spin wave excitation and detection techniques developing rapidly and based on a wide range of instrumentation [9]. Most of our experiments require coherent excitation, high sensitivity, phase control, and high frequency resolution. To explore spin wave excitation and propagation in the samples, we make use of spin wave spectroscopy [44, 47]. Because it exhibits both features of spin wave excitation and detection, spin wave spectroscopy has the edge over other techniques and is one of the best candidates for our research experiments.

1.4. Recent Advances and the State of Art

In M. B. Junfleisch et al [48], the authors performed an experiment of spin-torque ferromagnetic resonance (ST-FMR) on YIG, a ferrimagnetic insulator, by using the Spin Hall Effect for spin wave excitation and detection. **Figure 20** shows the schematic of ST-FMR setup. Spin Hall effects provide the possibility of exciting and detecting spin currents and magnetization dynamics in magnetic insulators [48]. In addition to having

`

low damping, which enables low power data transmission and processing by using magnons, YIG also has nonlinear dynamics that attract much research attention [48].

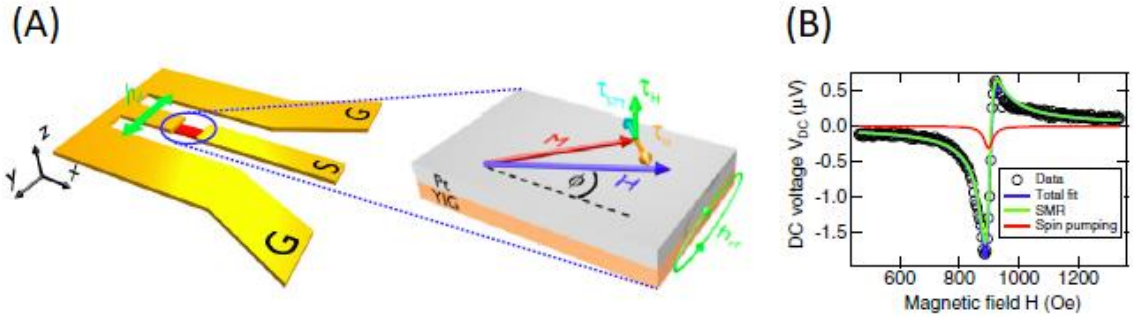

Figure 20 – (A) Schematic of the ST-FMR experimental setup with a zoom in the regions of YIG/Pt structure. The alternating RF current drives magnetic field h_{rf} and creates torque τ_H on magnetization M. Then, spin accumulation is generated by the Spin Hall Effect and has torque τ_{STT}. (B) Output voltage as a function of magnetic field at Φ=30˚. [48] *Phys. Rev. Lett.* 116(5), 057601 (2016), with the permission of APS publishing.

After alternating current was applied to electrically drive ST-FMR in the YIG/Pt sample, resonance peaks were detected. For better analysis, electrical measurements were compared using BLS imaging. This work has demonstrated the formation of a nonlinear, self-localized spin wave intensity driven by alternating current in a magnetic insulator (YIG) using the ST-FMR technique [48]. Since magnetic insulators exhibit extremely low Gilbert damping, they are outstanding materials for novel low power devices [48]. Therefore, this is a significant development for building spintronics applications using magnetic insulators.

Aside from previous literature using alternating current for spin wave excitation, alternating voltage has been proposed and demonstrated to drive spin waves as well. In S. Cherepov et al [49], due to CMOS transistors at small length scales having larger power

`

dissipation, the authors have demonstrated the application of magnetoelectric (ME) cells as a solution [49]. Moreover, the commonly used current-driven transducers such as inductive antennas and spin transfer torque-based techniques require relative large currents to operate, thus resulting in high power consumption [49].

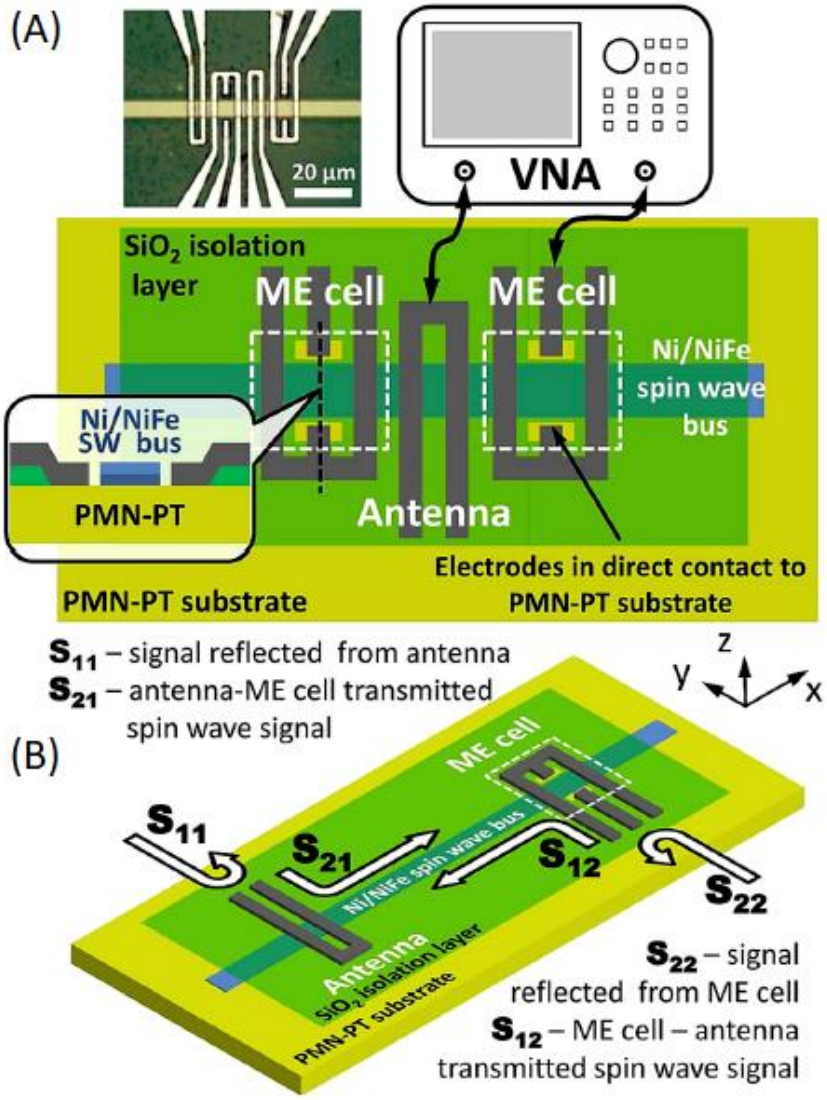

Figure 21 – (A) The device schematic. The optical image of spin wave bus and antennas are on the top-left side. Spin wave excitation and detection were performed with a network analyzer (VNA). Structure is started with PMN-PT substrate then Ni/NiFe spin wave bus. (B) An illustration of reflection and transmission signals measurements. [49] ***Appl. Phys. Lett.*** **104(8), 082403 (2014), with the permission of AIP publishing.**

`

ME cells are spin wave transducers where spin waves are generated by alternating voltages, and they are part of the heterostructure with piezo-electric $[Pb(Mg_{1/3}Nb_{2/3})O_3]_{(1-X)}$-$[PbTiO_3]_X$ (PMN-PT) as the substrate. In addition, ME cells do not suffer from Ohmic losses intrinsic to current driven spin wave excitation mechanisms [49]. Therefore, the power consumption of ME cells is determined by negligible AC current flow, caused by RF driving of the device capacitance, during the operation [49].

Figure 21 shows the complete design of the device. ME cells serve as electrodes and are connected to the alternating electric field. Next, the RF voltage is applied to the PMN-PT substrate to generate strain. Then, the generated oscillating strain causes magnetoelastic spin wave excitation in the magnetostrictive Ni layer due to alternating strain induced anisotropy [49]. Finally, spin waves propagate in the Ni/NiFe spin wave bus and are detected on the other side of the device. Although a generated spin wave has relatively small amplitude, this problem can be improved with lower damping and better geometric design [49], or vice versa: spin waves can be used to produce strain and translate to the PMN-PT layer, reading out voltages at the contact layer.

Moreover, one of the most promising concepts of circuit design using ME cells has been presented in [50]. Spin wave devices (SWD) are logic components that utilize the oscillation of magnetization in ferromagnetic materials [50]. The magnetization states can be used for information storage and are controlled by a bias electric field [50]. With multiple ME cells, it is possible to create an array of magnonic logic circuits [50]. Overall, this device has opened a new route for spin wave logic circuits and lower power dissipation, with the potential of future research in this area.

`

1.5. Research Objectives

Spin waves possess a unique combination of properties, which allows us to build scalable devices compatible with conventional magnetic memory [51]. It is important to investigate spin wave excitation and transport in micro- and nanostructures. Therefore, my research objectives are the following:

- Investigation of spin wave excitation, propagation, and interference in magnetic waveguides
- Study of spin wave transport in curved waveguides
- Further experimental knowledge in understanding spin waves control in synthetic multiferroic devices and its possible applications
- Advance the study of spin wave excitation, propagation, and control in Py thin film and nanowires for possible novel design

`

Chapter 2. Device Fabrication and Characterization Techniques

The advances in integrated circuits (IC) technology has thrived because of the semiconductor device fabrication process [52]. Micro- and nano-electronics demands have helped to drive the research and development of fabrication methods. Germanium was one of the first dominate materials for semiconductor device fabrication, but silicon surpassed it in the early 1960s [52]. Silicon is one of the most abundant materials and has a larger bandgap, making it lower cost and easier for fabrication processes [47].

As for my research, the main substrates for my samples and devices are silicon and gadolinium gallium garnet (GGG). My research topics focus on $Ni_{80}Fe_{20}$ (Py) and $Y_3Fe_5O_{12}$ (YIG), because they possess relatively low spin wave damping, making them great candidates for spin wave excitation and propagation. Py is widely used in the field of magnetism, because it has high permeability, low coercivity, and low magnetic anisotropy [53]. Most importantly, Py has good compatibility with silicon. Silicon is frequently used in the semiconductor technology industry, and silicon based fabrication processes have been explored and developed by many [52]. In the mid-1940s, silicon started to emerge in communication technology. This was due to silicon's small dimensions and high cut-off frequencies, which made it a good candidate for microwave applications [54]. Since then, fabrication techniques based on silicon substrates have been accelerated for research and application purposes.

Furthermore, Py films can have spin wave propagation distances up to tens of micrometers range, while YIG films allow spin waves to travel up to tens of millimeters

`

[55]. This makes YIG a good material for my research. Compared with metallic superlattices, magnetic oxides superlattices have not been studied as much, but iron garnets are a large class of ferro-magnetic oxides with wide applications in magnetic optical and memory devices [56]. For materials like YIG, GGG is a great candidate as a substrate, due to its small lattice mismatch and because YIG can be grown on GGG using pulsed laser deposition (PLD) or liquid phase epitaxial methods [56].

After samples and devices have been completed and are ready for measurements, it would be beneficial to perform some characterization for better understanding. There are various characterization techniques to analyze and confirm the properties of samples. For instances, scanning electron microscope (SEM) is one of the techniques that I used very often to check the dimensions of our samples and devices. In this section, I will introduce some of the fabrication and characterization techniques that I used frequently for our lab.

2.1. Fabrication Process Techniques

Lithography processes are the most common fabrication techniques, and include photolithography and electron-beam lithography (EBL) processes. Photolithography is widely used in semiconductor industries, because of its high throughput, low cost, simplicity, and reproducibility [57]. The main concept of photolithography is to transfer a photomask's patterns onto desired materials. **Figure 22** shows the general steps for

`

photolithography process, and all procedures are done in cleanroom facility for ultraclean conditions. Details of photolithography process are included in the caption of **Figure 22.**

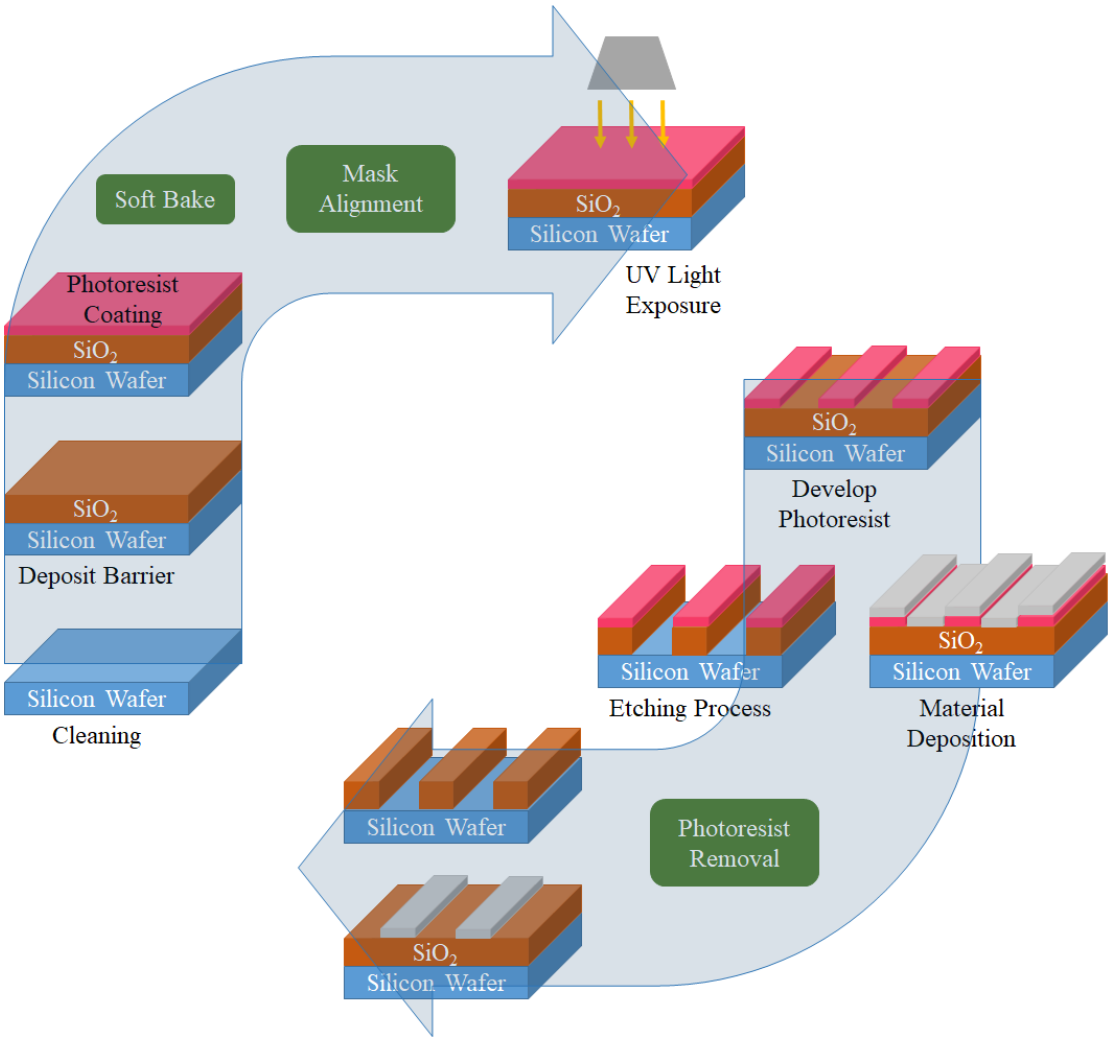

Figure 22 – Flowchart of photolithography process. The first step is to clean the substrate (e.g. Si wafer), rinse it in the order of acetone, isopropanol (IPA), and de-ionized (DI) water. Next, SiO_2 can be deposited on the Si substrate as an insulator layer, and then spin-coated with photoresist (p-type or n-type). After the photoresist is evenly spread on the surface, use a hot plate for baking to remove solvent from the photoresist and to ensure adhesion. Then, place the photomask and sample in the mask aligner instrument and align both accurately. Once all necessary parameters are adjusted, expose the sample with ultraviolet (UV) light. Submerge the sample into the developer after exposure to remove unwanted areas of photoresist. Depending on the needs, one may either etch the sample or deposit materials after developing the sample. Finally, perform the lift-off process to remove the rest of the photoresist, completing the photolithography technique.

`

It uses optical light (UV light) to go through the photomask's windows and reacts with photoresists that are coated on the surface of the sample. I have performed photolithography at UC Riverside and UCLA, and both campuses have a Karl Suss model MA-6 mask aligner. **Figure 23**A shows the mask aligner that I operated.

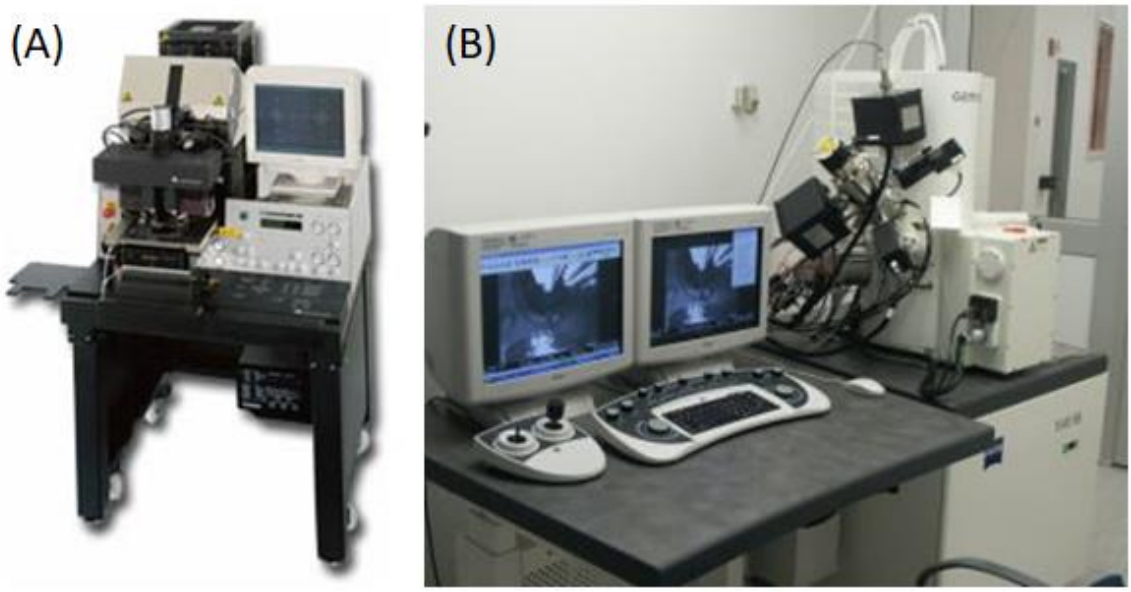

Figure 23 – (A) Karl Suss model MA-6 mask aligner, for photolithography processes. (B) Focused ion beam (FIB) milling system can also be used for E-beam lithography or as an SEM system [58].

After developing the samples, there are two choices depending on the goal with the sample. First, the sample may be etched with inductively coupled plasma (ICP), and to make trenches or contact gates. Another way is to deposit other materials using electron beam evaporator or sputtering system. When both choices are completed, it is important to remove the remaining photoresist. The process of photoresist removal is called the lift-off process, and I have been using either acetone or PG remover to remove

`

the photoresist. Once the lift-off process is finished, the cleaning process is repeated to ensure the sample is without any chemical residuals.

EBL is another main lithography that I used often, and **Figure 23**B shows the EBL system from UCR's cleanroom. Since the dawn of semiconductor research, many types of particle beams have been studied and used for lithography process, and due to photolithography, they have diffraction limitations, as the use of conventional or UV light is becoming increasingly inadequate [59]. The electron source has the benefit of extremely high diffraction-limited resolution and is one of the best methods for nanoscale feature sizes [59]. EBL is a popular selection for nanoscale structures and is favored in making photomasks and reticles from computer-aided design (CAD) files in the semiconductor industry and in academic research by using both direct writing and projection printing techniques [60]. A brief illustration of the EBL process is shown in **Figure 24**.

Like the photolithography process, EBL will be spin coated with e-beam resists and then placed inside of a vacuum system. There are two methods for writing patterns onto a sample: design patterns using an e-beam manually or load patterns' files through the nanometer pattern generation system (NPGS). Before uploading design files to NPGS, I use AutoCAD software to design patterns and convert the files with KLayout into GDS format. Once the pattern files are uploaded in NPGS, and the control parameters (e.g. exposure time and pattern layers' order) are set, the system will prompt a series of commands to assist in setting the alignment markers. Next, NPGS will have total control of the E-beam system and will start to expose the resist with electrons. After

`

exposure, the rest of the processes are the same as photolithography: develop the sample, deposit the materials (or etch materials), and complete the lift-off process.

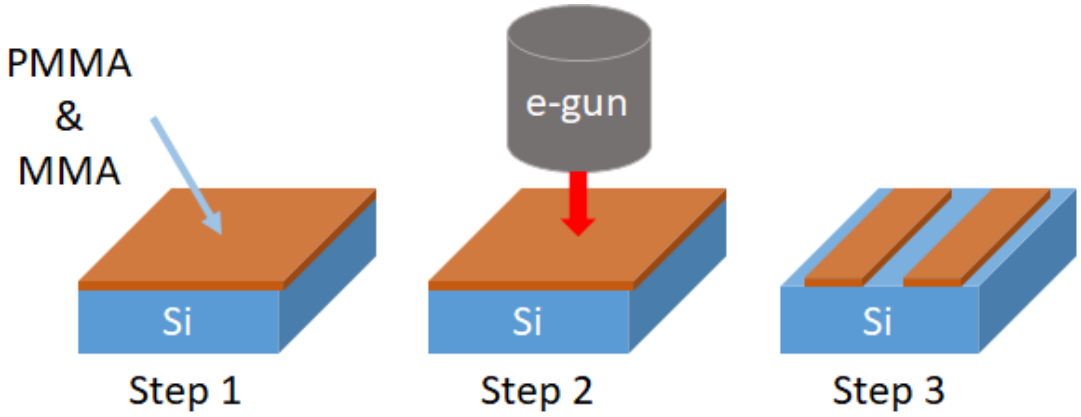

Figure 24 – Schematic of EBL process.

The etching process is an important step during micro- and nanofabrication. Most of the time, the dry etching techniques were used due to their advantages over wet etching techniques. Dry etching techniques are widely used for Very-Large-Scale Integration (VLSI) fabrication [52]. The reason is that in comparison to wet etching techniques, dry etching techniques can offer better anisotropic etching profiles and avoid the undercutting problems. The etching profiles of wet and dry etching techniques are shown in **Figure 25**. Moreover, wet etching techniques produce large amounts of liquid chemical wastes that need to be disposed properly, while dry etching techniques only use small amounts of reactant gases [52]. There are several sources for dry etching process, with ICP etching system being one of the dry etching techniques that is based on a plasma source [61]. ICP plasmas are formed by applying RF power into an inductive coil that circled a dielectric vessel, and a magnetic field is applied to generate plasma inside

`

the chamber [61]. **Figure 26** illustrates an ICP system and its chamber. Inside of the vacuum chamber, the plasma diffuses from the generation region and drifts to the substrate at a low ion energy, then the plasma starts to create low damage when achieving high etching rates [61]. **Table 2** shows a sample of frequently etched materials with corresponding reactant gases.

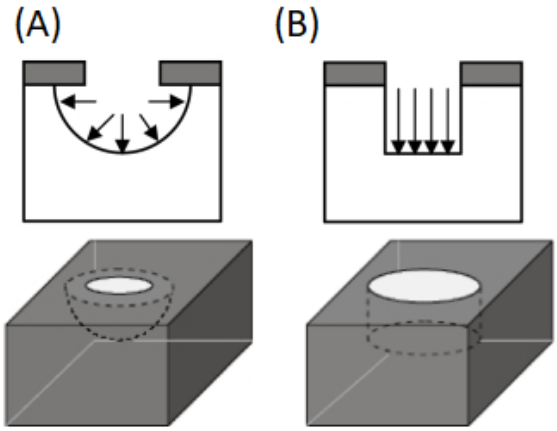

Figure 25 – (A) Isotropic etching profile with wet chemical etching technique. The material under etching mask (top layer) is undercut. (B) Anisotropic etching profile with dry plasma etching techniques [62].

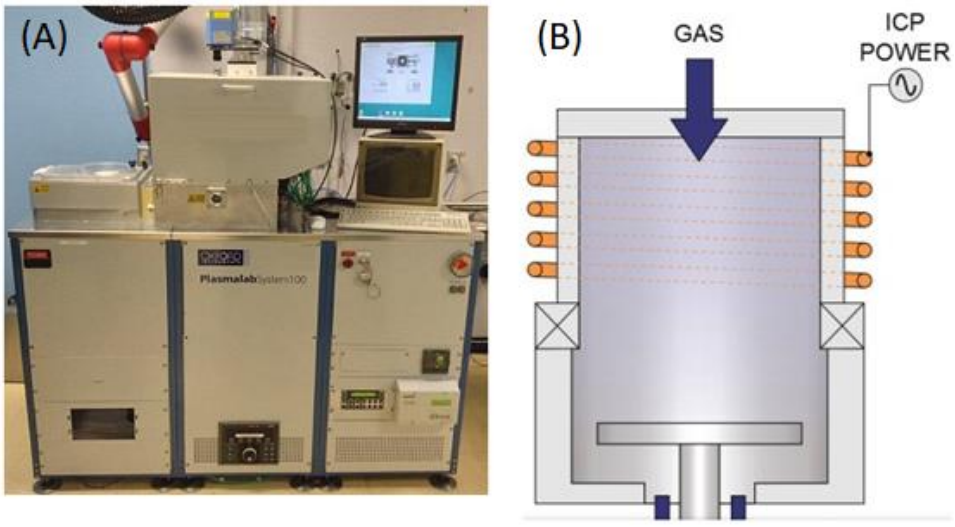

Figure 26 – (A) Oxford Plasmalab model 100/180 Inductively Coupled Plasma (ICP) system. (B) Schematic of ICP system [58, 63].

`

Materials	Source Gases
Organic Materials	O_2, SF_6, CF_4
Polysilicon	CCl_4, CF_4, NF_3, SF_6
Silicon Dioxide	CF_4, C_2F_6, C_3F_8, CHF_3
Silicon Nitride	CF_4, C_2F_6, CHF_3, SF_6
Aluminum	CCl_4, Cl_2, BCl_3
Titanium	$C_2Cl_2F_4$, CF_4
YIG	Ar
Py	Cl_2, He, Ar, Xe

Table 2 – Plasma etching sources [52].

Another etching method that I used for my research projects is ion milling, which is performed with the FIB system. **Figure 23**B shows the FIB instrument that I used for micro- and nano-device fabrication. As with performing the EBL process, the sample will be placed inside of a vacuum chamber for low pressure operation and a confined plasma will be used to generate ions. Ion milling uses energetic noble gas ions such as Ar^+ to bombard the material's surface [52]. The etching process can be achieved by physically knocking atoms off the surface of the material, easily making the design of the desired pattern or structure [52]. Although the FIB system provides an extremely anisotropic, higher than ICP etching technique, ion milling has disadvantages such as poor selectivity and residue on the sample. **Figure 27** shows the SEM image of Py nanowires milled with FIB that was made in UCLA.

`

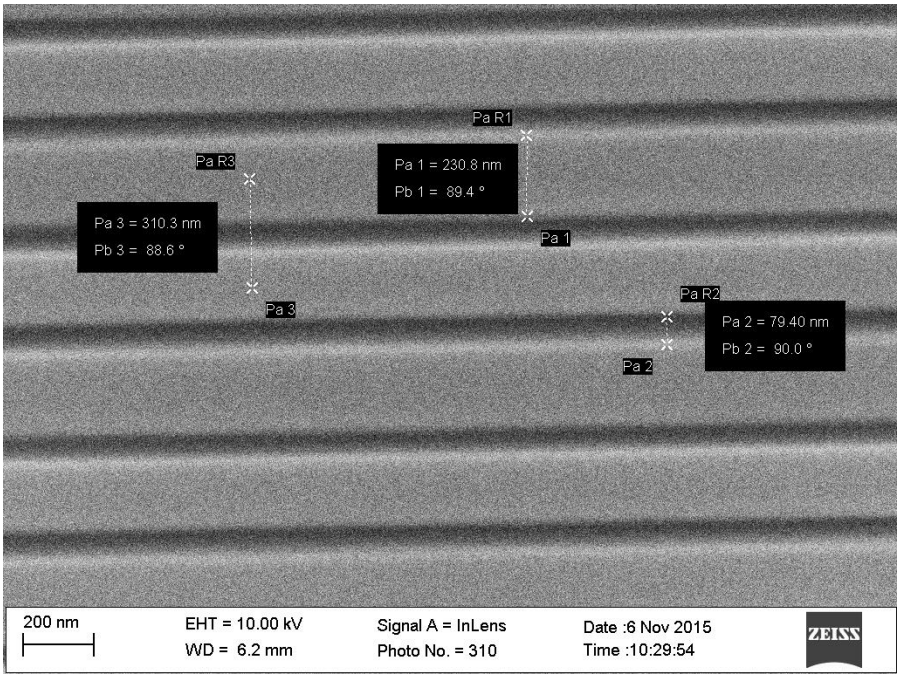

Figure 27 – SEM image of Py nanowires made by FIB. Each nanowire has width about 230 nm with 50 µm length, and gaps between wires is about 80 nm. There are in total about 2200 nanowires for the sample.

After performing the photolithography or EBL process, material deposition is one of the methods that I used very often. There two techniques for film deposition: the electron-beam (E-beam) evaporator and the sputtering system. **Figure 28**A shows an actual image of an E-beam evaporator. Most of the time, I deposited materials for micro-antennas with either Ti/Au or Co/Au. The operation of the E-beam evaporator started by placing the sample inside of a vacuumed chamber and loading the source material's parameters, such as density and impedance. Once the pressure has reached operating pressure, the electron beam will be generated from a filament and steered via electric and magnetic fields to strike source material, then vaporize it within a vacuum environment [52]. Since thermal energy is low, the pressure inside of the chamber should be below the

`

point where the mean free path (evaporated source material's atom) is longer than the distance between the E-beam and the substrate, and typically lower than $3.0*10^{-4}$ Torr [64]. This is the reason that I always started the deposition process at $5.0*10^{-6}$ Torr to ensure the quality.

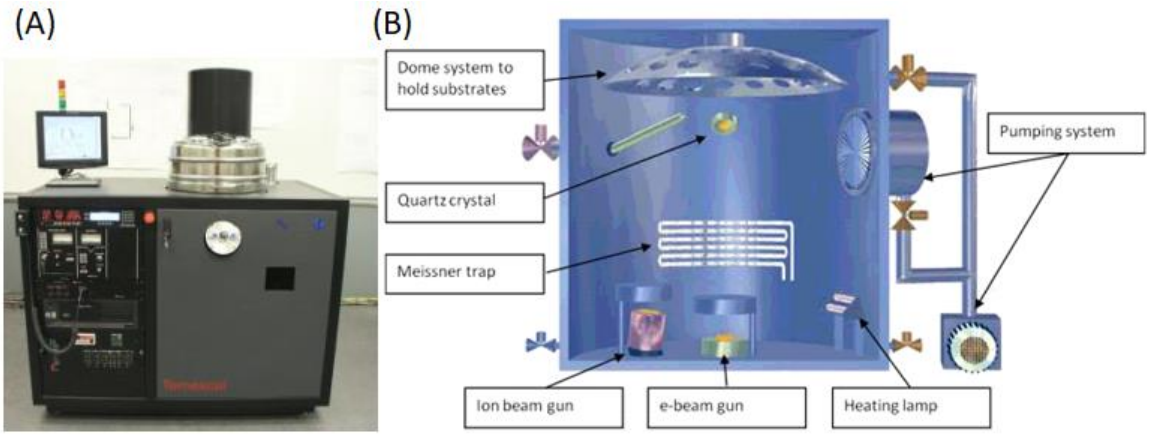

Figure 28 – (A) E-beam evaporator, TES Themescal BJD 1800 system. (B) A detailed schematic illustration of E-beam evaporator's chamber. [58, 65]

Our cleanroom at UCR has two different types of E-beam evaporators: one uses manual control and another uses an automated system. The automated system is not ideal for the precise growth of materials, due to the E-beam overshooting the set-up deposing rate, and could affect the attachment between the growth layer and the substrate (sample). When operating an E-beam evaporator, monitoring the deposition rate is an important step that must always be kept in mind, because this will affect the thickness of deposition. One method of monitoring the deposition rate is to use a quartz crystal, which is covered by the evaporating material during deposition [52]. The resonant frequency of the crystal shifts in proportion to the thickness of the deposing material, so monitoring the resonant

`

frequency of the crystal will be able to measure the deposition rate with accuracy around 1 Å/sec [52].

Different from E-beam evaporation, sputtering does not create evaporated atoms, but rather creates a plasma of charged particles with high energy, which enables much more energetic particles to organize themselves to have high density of thin films [65]. To ensure optimized quality for spin wave excitation and propagation, a sputtering system was used for Py and SiO_2 materials deposition. One of the most common sputtering techniques is magnetron sputtering [65]. It has magnets placed at the area of the target (source material) to keep the density of ions high, increasing sputtering efficiency [65]. Before every deposition with the sputtering system, it would be beneficial to use it as sputter etching. Sputter etching can be viewed as a reversal of the sputter deposition process, because this process is used to clean the substrate and to clean contact windows prior to film deposition [52]. This etching process helps to remove residual oxide, which can improve the contact between deposited thin film and the substrate [52]. The sputtering is achieved by using ions such as Ar^+ and bombarding a target, then knocking the surface atoms off and transporting to the substrate for deposition [52]. There are two types of power source for Ar^+ energy supply: DC and RF power sources. Electrically conductive materials such as Al, W, and Ti can use a DC power source, as these targets are acting as the cathode in a diode system [52]. Dielectric materials such as SiO_2 and Al_2O_3 can use an RF power source [52]. An AJA sputtering system is shown in **Figure 29**A.

`

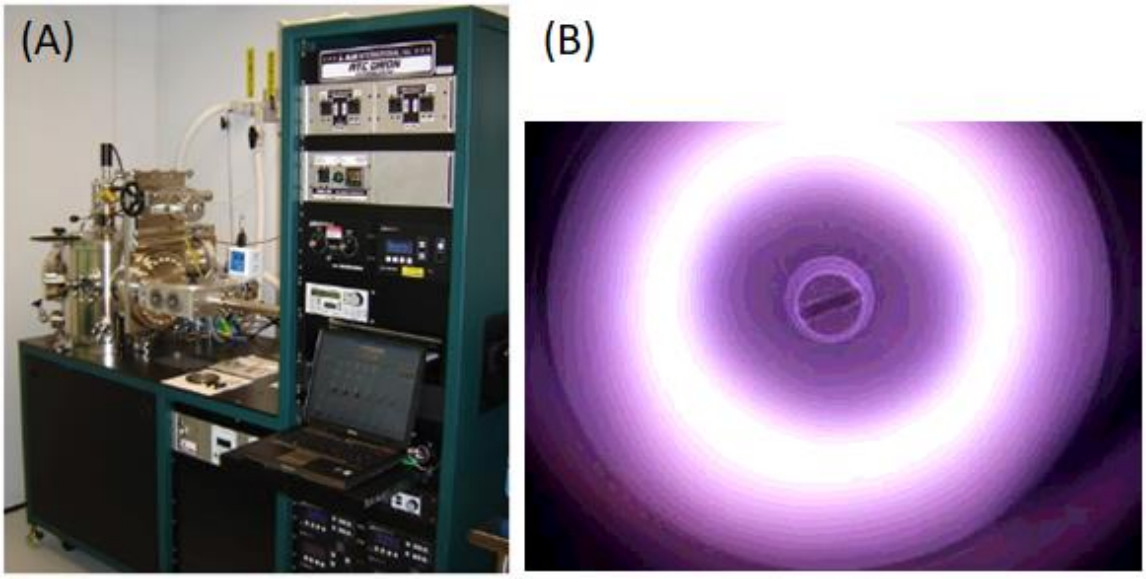

Figure 29 – (A) The load-locked AJA ORION 5 sputtering system. (B) Inside of a sputtering chamber, the plasma from the circular silicon target under Ar^+ ion bombardment. The white light represents the highest density of the ions and corresponds to the permanent magnetic field. [58, 65]

2.2. Characterization Techniques

Scanning electron microscope (SEM) is an instrument that has been used widely in industrial, commercial, and research applications [66]. A schematic of SEM is shown in **Figure 30**. SEM can provide images of micro- and nanoscale structures in topography, morphology, and composition. Inside of an SEM vacuum chamber, the surface of the sample is bombarded with accelerated electrons with energy from 500 to 40,000 eV [52]. Next, the injected electrons make secondary electrons to be ejected from the inner shells of the atoms, whose images of the sample are formed by scanning the surface of the sample and detecting the intensity of the secondary electron current [52]. The electron beam comes with an electromagnetic lens that is used to control the path of the electrons;

`

for instance, the condenser lens controls the size of an electron beam, which defines the resolution [66]. During the SEM imaging, there are many parameters that need to be adjusted to produce the optimized results. One of the critical parameters is selecting the contrast ratio when imaging. This adjustment could affect if the image is visible or not, due to the intensity only representing in white and black (bright and dark) colors. In addition, images with contrast information between areas with different chemical compositions as heavier elements (relatively higher atomic numbers) will appear in brighter color [66].

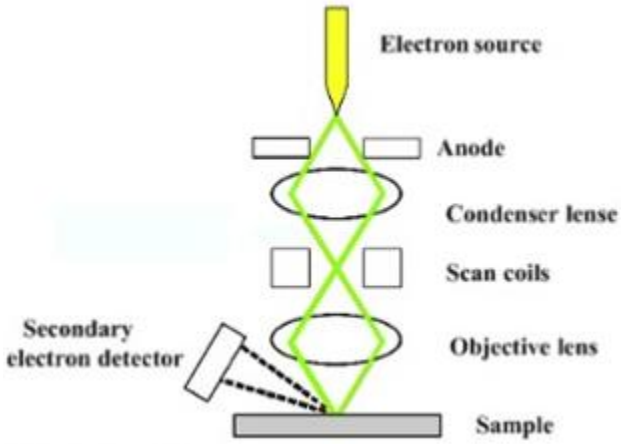

Figure 30 – Schematic design of SEM. Electron Condenser lens determines the resolution, and the objective lens is used to focus the electron beam onto the sample. The scan coils guide the electron beam to the sample. The secondary electron detector is placed at an angle, because this way it can increase the efficiency of detection. [66]

A typical SEM has a minimum resolution limit of 2 – 3 nm with magnification up to 300,000, qualities that have made SEM a great instrument for the IC industry [52]. Finally, one of the problems that most SEM users face is the charging effect. This is caused by electrical charge-up of the sample from the electron beam, and occurs

`

frequently in insulating materials [52]. The charging effect can be eliminated by coating the surface with a conducting layer of gold [52], or by simply attaching the edge of the surface with copper tape to the ground (e.g. SEM sample holder).

When it comes to measuring magnetic moments, there are three general categories of methods: measurement of a force on a material in a non-uniform magnetic field, measurement of magnetic induction in the vicinity of the sample, and indirect measurement of phenomena which involve the magnetic properties [67]. However, all these methods possess one major disadvantage, which is that the detection coil is symmetrically distributed about the sample with the axis of the detection coil parallel to the applied magnetic field [67]. Although a laboratory magnet can be modified to solve this issue, it still could not provide an extremely uniform magnetic field for measurements [67]. Vibrating sample magnetometer (VSM) was invented by Simon Foner with the purpose of introducing a simple, versatile, and inexpensive magnetometer capable of measuring magnetic properties with high accuracy [68]. An actual VSM system is shown in **Figure 31**A. VSM is used to characterize the DC magnetic properties of materials as a function of magnetic field, temperature, and time [69]. In VSM, the sample for magnetization characterization is placed at the tip of the sample holder, and the sample holder is in between the electromagnets, as illustrated in **Figure 31**B. Then, the sample is magnetized by a uniform magnetic field created between the electromagnets' poles. This causes the sample to generate its own magnetic fields. Next, by vibrating the sample in the vicinity of the detection coils, an electrical current is induced in these coils. The induced electric current is proportional to the sample's magnetic moment, but does

`

not depend on the strength of the applied magnetic field [67]. Therefore, the sample's magnetic moment is determined by measuring the electric current induced in the detection coils.

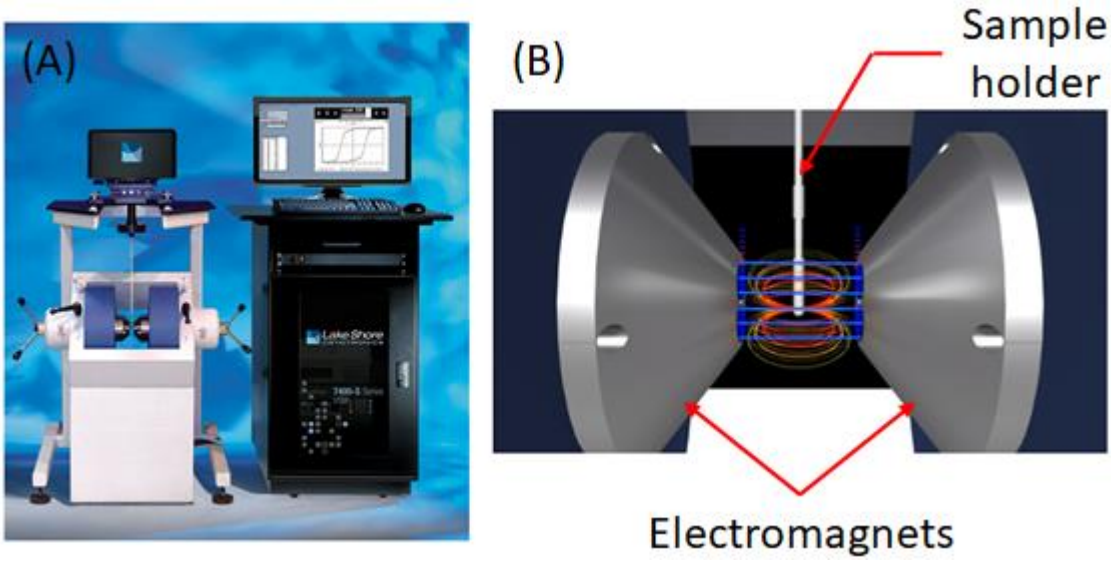

Figure 31 – (A) A complete system of VSM. (B) An illustration of VSM measurement. The sample is on the sample holder, which is in between electromagnets for uniform magnetic fields. During the measurements, the sample holder will be moving up and down to induce electrical current in detection coils, and then the signals are measured by the detection coils. [69]

Atomic force microscope (AFM) and magnetic force microscope (MFM) are the same instruments that have very similar principles of operations. In 1986, Gerd Binning and Heinrich Rohrer won the Nobel Prize in Physics for the invention of scanning tunneling microscope (STM) and for discovering that it can image surfaces at the atomic scale with unprecedented resolution [70]. AFM was then developed by Binning, Quate, and Gerber as a collaboration between IBM and Stanford University. There are three primary modes for AFM: contact mode, non-contact mode, and tapping mode [71]. **Figure**

`

32A shows the SPM system that can be used for both AFM and MFM, depending on the types of scanning probe.

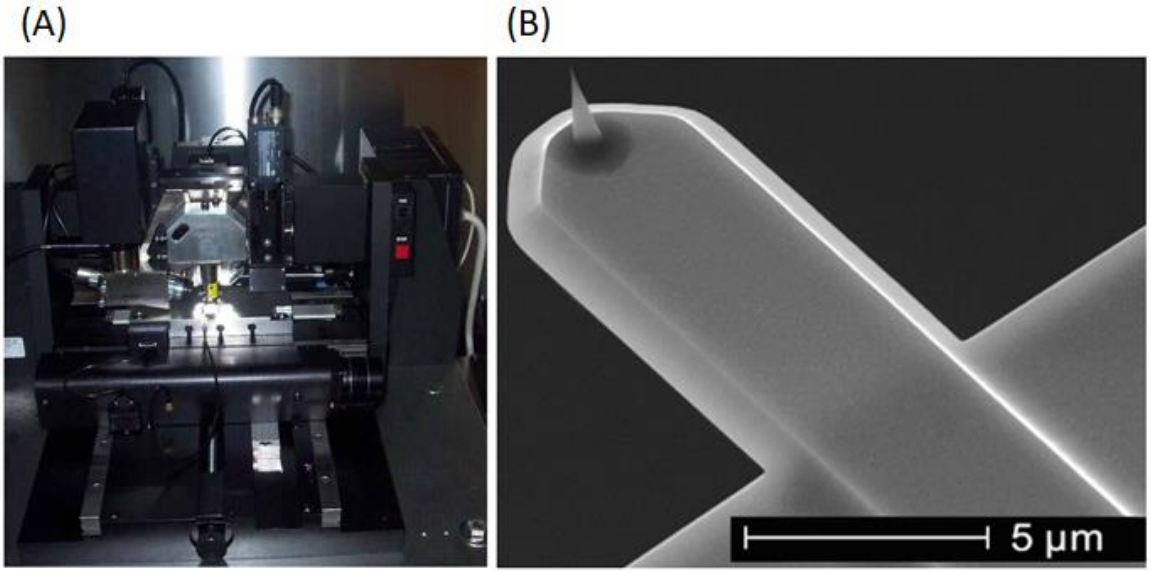

Figure 32 – (A) Veeco Dimension 5000 SPM system. This system also comes with vibration isolation table and acoustic enclosure. (B) An SEM image of an AFM scanning probe. High quality AFM probe for high speed AFM (HS-AFM). [58, 74]

AFM has a sharp tip (scanning probe) attached to a flexible spring-like cantilever that mechanically senses the force between the tip and the sample [72]. A laser is constantly pointing at the back of cantilever, and the cantilever deflection is monitored by the reflected laser beam back to the photodiodes [73]. These forces will cause the cantilever to bend when the tip moves through the surface of the sample and the scanner moves vertically at each x- and y-axis data point, which are stored by the computer to form the topographic image of sample surface [71]. **Figure 33** shows the illustration of how AFM works.

`

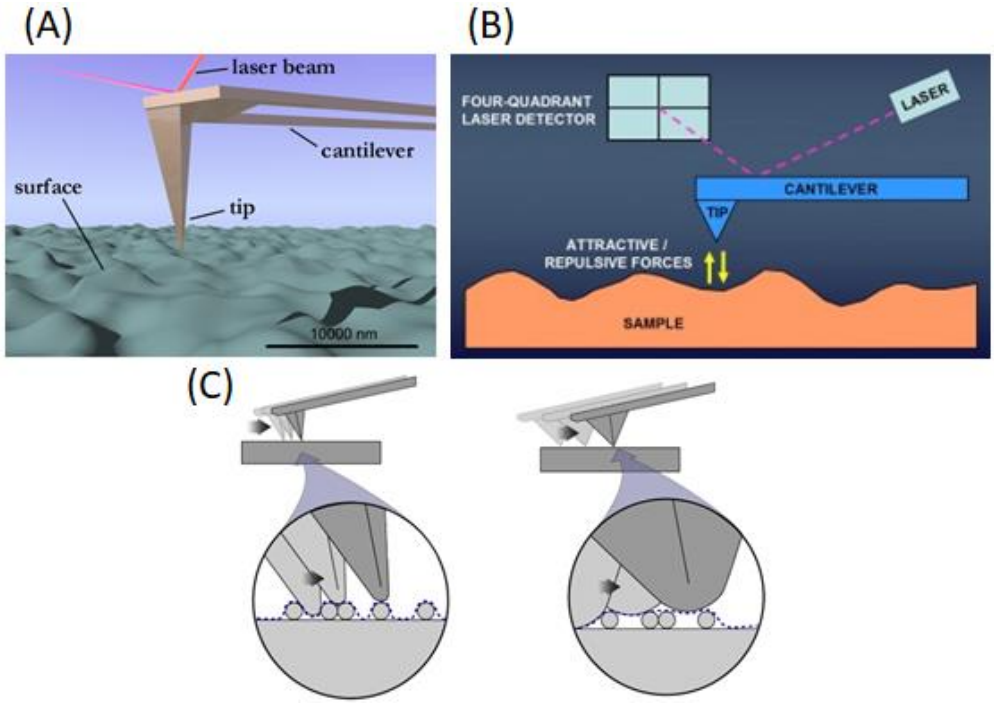

Figure 33 – (A) An illustration of scanning probe moving over the surface of sample. (B) The laser is reflected to a four-quadrant photodiode detector. When imaging the surface of the sample, the tip is constantly repelling or attracting to the surface, and the cantilever is bending up or down by the force. (C) The graph on the left has smaller radius of tip curvature, which is better for smaller features. Normally this is an AFM tip. The graph on the right has larger tip curvature radius, and this could be due to material coating. For instance, MFM tips have a layer of Co coating for magnetic property. [72, 73, 75]

In addition, AFM can be operated in liquid and under physiological conditions, which enables the possibilities of applying this technique in biological specimens [72]. The operation of MFM is similar to AFM, except for the choices of tip. MFM is based on the magnetic forces repulsion and attraction between the tip and the sample. These two SPM techniques are extremely useful for characterizing samples' properties, and have served important roles for my research projects.

`

Chapter 3. Spin Waves Excitation and Propagation in YIG Films and Py Nanowires

Spin dynamics phenomena in nanoscale have attracted much interest in recent years, especially in studies of spin waves [76]. The research and development of spin waves are the fundamental processes that drive scientists to better understand spin wave dynamics. These further understandings enable the possibilities of novel spin-based techniques and applications. Therefore, in this chapter, three important studies will be introduced to provide a great deal of contribution to the study of spin waves.

3.1. Spin wave interference in YIG cross junction [77]

This section focuses on the interference between backward volume magnetostatic spin waves (BVMSW) and magnetostatic surface spin waves (MSSW) in a magnetic cross junction. Potentially, spin wave devices may provide a route towards scalable devices convenient for in-chip integration [78]. One of the main challenges is associated with the spin wave interconnects, including orthogonal (e.g. cross shape) junctions. Currently, there are just a few experimental or theoretical works devoted to this problem. Moreover, in most of these works, spin wave interference was observed for the one type of magnetostatic spin waves possessing the same dispersion relation.

BVMSW and MSSW possess different dispersion relations, with zero frequency overlap in infinite magnetic films. However, these two different spin wave configurations may have interference observed in finite structures due to the effects of magnetic shape

`

anisotropy. **Figure 34** illustrates the conditions with infinite films and finite structures. In the following section, I conduct experiments on these two different types of magnetostatic spin wave interference in a micrometer size of YIG cross junction.

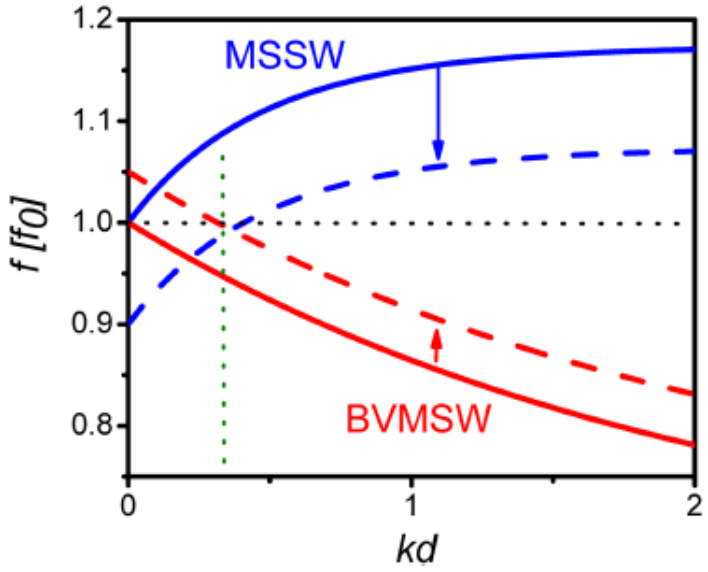

Figure 34 – A graph of numerical modeling. It is showing MSSW and BVMSW dispersion in 3.8 μm thickness YIG film. The solid curves show the only overlap point is at $k = 0$. The dashed curves illustrate the dispersion modification due to the effect of the magnetic field anisotropy leading to a non-zero overlap. [77] *AIP Adv.* 7(5), 056633 (2017), with the permission of AIP publishing under CC BY license, link: https://creativecommons.org/licenses/by/4.0/

3.1.1. Experimental procedures and results

Before the experiments begin, the overlap frequency region for BVMSW and MSSW configurations must be estimated. BVMSW possess negative group velocity $v_g < 0$, while MSSW possess positive group velocity $v_g > 0$ [79]. In the case of an infinite and uniformly magnetized film, the only overlap point between the two dispersion curves occurs at $k = 0$, which corresponds to the ferromagnetic resonance [2]. BVMSW and

`

MSSW have non-overlapping frequency ranges [ω_H, ω_0] and [ω_0, ω_S], respectively, where

$$\omega_H = 2\pi\gamma H, \qquad \omega = 2\pi f \tag{11}$$

$$\omega_0 = \sqrt{\omega_H(\omega_H + \omega_m)} \tag{12}$$

$$\omega_m = 2\pi\gamma 4\pi M_0 \tag{13}$$

$$\omega_S = \omega_H + \omega_m/2 \tag{14}$$

($\omega_H < \omega_0 < \omega_S$), γ is the gyromagnetic ratio. However, a non-zero overlap may be possible due to the effect of the magnetic field anisotropy caused by the demagnetization fields in the cross junction. In order to estimate the width of the overlap region, formalism developed for a homogeneously magnetized ellipsoid was used [79]. The demagnetization field can be related the magnetization of the sample by

$$\overrightarrow{H^m}(\vec{r}) = -\hat{N}(\vec{r})\vec{M}(\vec{r}) \tag{15}$$

where $\hat{N}(\vec{r})$ is the tensor of demagnetization coefficients. In this experiment, a cross structure is consider with $L >> w >> d$, where L is the length, w is the width, and d is the thickness of the YIG cross. In this case, one may restrict consideration by the width N_d and thickness-related N_w demagnetization fields as $N_d >> N_w >> N_L$. In addition, the long-wavelength limit (i.e. FMR frequency) of the BVMSW and MSSW can be found as follows:

`

$$\omega_0^V = \sqrt{\omega_0^2 + N_w \cdot (1 - N_w)\omega_H \omega_m} \tag{16}$$

$$\omega_0^S = \sqrt{\omega_0^2 - N_w \cdot \omega_m (3\omega_H + 2N_w \omega_m)} \tag{17}$$

The demagnetization field will increase ω_0^V while decreasing ω_0^S. Therefore, the overlap frequency region can be estimated as follows:

$$\Delta\omega_0^{V,S} \approx \frac{2N_w \omega_H \omega_m}{\omega_0} \tag{18}$$

The estimated width of the overlap region $\Delta\omega_0^{V,S}$ for the micrometer-size YIG cross (i.e. *L* is 3.65 mm; *w* is 650 μm; *d* is 3.8 μm, and N_w is 0.012) is about 70 MHz at the bias magnetic field *H* with 1 kOe. These estimates show the possibility of the frequency range overlap and provide an insight on the operational frequency range for a given structure and at a certain bias magnetic field.

The cross junction is made of single crystal YIG film epitaxially grown on top of a Gadolinium Gallium Garnett ($Gd_3Ga_5O_{12}$) substrate using the liquid phase transition process. The cross shape was obtained by laser ablation using a pulsed infrared laser (λ is 1.03 μm), with a pulse duration of ~256 ns. The YIG cross has the following dimension: the length of each waveguide is 3.65 mm; the width is 650 μm; the thin film thickness is 3.8 μm; and the saturation magnetization of $4\pi M_0$ is 1750 Oe. Next, four micro-antennas were fabricated on the edges of the cross. These antennas were fabricated from a gold wire with thickness 24.5 μm and placed directly on the top of the YIG surface. The antennas are connected to a programmable network analyzer (PNA) Keysight N5221A.

`

Two of the antennas depicted by the numbers 1 and 2 are used to generate two input spin waves for interference at the cross junction. The inductive voltage was detected by the antenna depicted by the numbers 3 and 4.

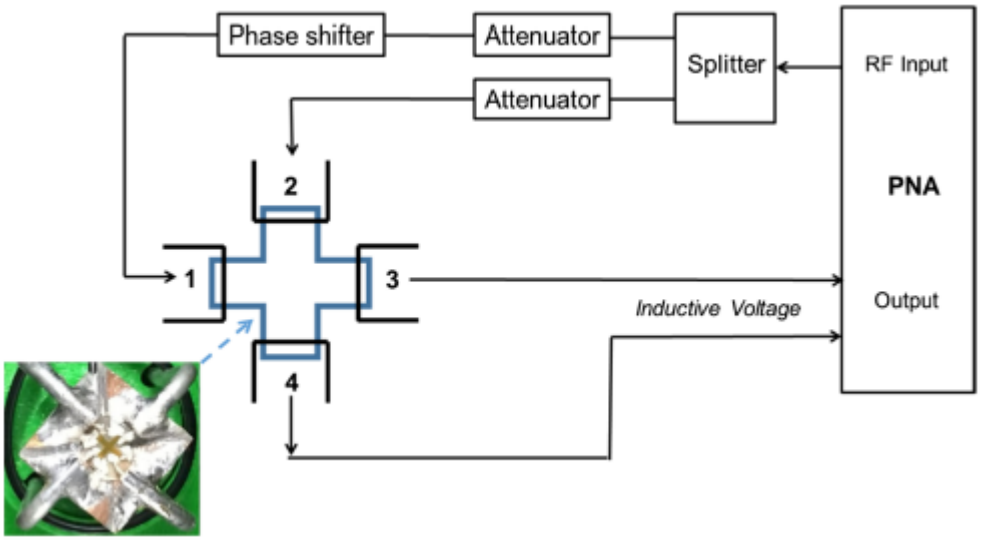

Figure 35 – The schematic of experimental setup with a photo of the YIG cross device. There are four micro-antennas fabricated at the edges of the cross marked as port 1, 2, 3, and 4. Two input spin waves are generated by the micro-antennas located at ports 1 and 2. Input power and the phase difference between the input signals are controlled by the set of attenuators and a phase shifter. The output inductive voltage is detected at port 3 or port 4. [77] *AIP Adv.* 7(5), 056633 (2017), with the permission of AIP publishing under CC BY license, link: https://creativecommons.org/licenses/by/4.0/

Figure 35 shows the schematic of the experimental setup. the measurements were performed with spin wave spectroscopy technique, as described in Chapter 2. In addition, we used a set of attenuators (PE7087) and a phase shifter (ARRA 9428A) to independently control input power and the phase difference between the input ports. All experiments are done at room temperature.

The experimental results are shown in **Figure 36** and **Figure 37.** In **Figure 36**, the inductive voltages are detected at port 3 as a function of the phase difference between the

`

spin waves excited at ports 1 and 2. The black curve shows the inductive voltage in case the bias magnetic field H = 798 Oe is directed along the virtual line connecting ports 1 and 3. In this case, there is a BVMSW type of spin wave propagating from port 1 and a MSSW type of spin wave propagating from port 2. The red curve corresponds to the case when the bias magnetic field is directed along the virtual line connecting ports 2 and 4. In this case, there is a MSSW type of spin wave propagating from port 1 and a BVMSW type of spin wave propagating from port 2. The blue curve corresponds to the case when the bias magnetic field is directed at 45˚ degrees to the virtual line connecting ports 1 and 3. The excitation frequency in all experiments was at 4.095 GHz. The collected data show prominent spin wave interference in three different cases. The interference effect disappears with the change of the operational frequency Δf is 100 MHz.

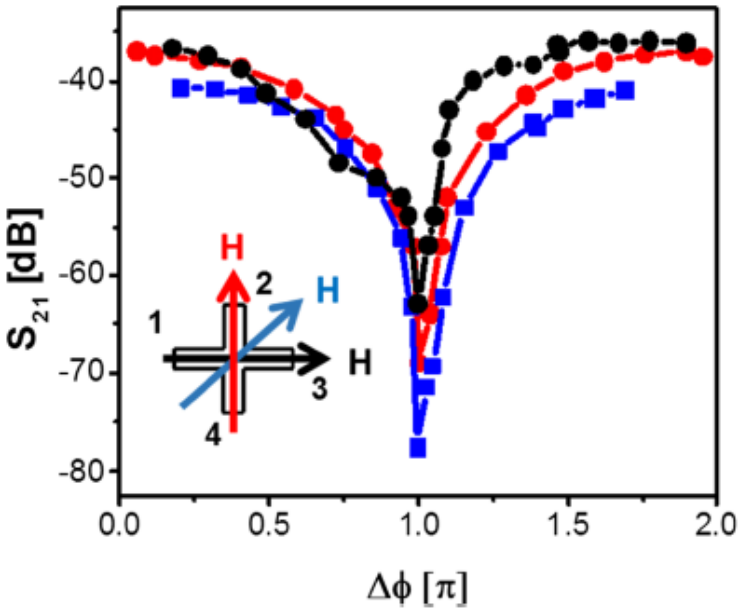

Figure 36 – Experimental data showing the change of the output signal measured at port #3 as a function of the phase difference between the waves excited at ports #1 and #2. The curves of different colors correspond to the different orientation of the bias in-plane magnetic field as illustrated in the inset. [77] *AIP Adv.* 7(5), 056633 (2017), with the permission of AIP publishing under CC BY license, link: https://creativecommons.org/licenses/by/4.0/

`

In **Figure 37**, it shows the inductive voltage detected at ports 3 and 4 as a function of the phase difference. The bias magnetic field H = 798 Oe has direction along the virtual line connecting ports 2 and 4. From the results, there is a significant asymmetry in the output characteristics. However, symmetric output characteristics are observed for the bias magnetic field directed at 45˚ degrees to the virtual line connecting ports 1 and 3. In addition, we observed significant change in the output voltages at ports 3 and 4 depending on the strength of the bias magnetic field, but this requires further experimental verification.

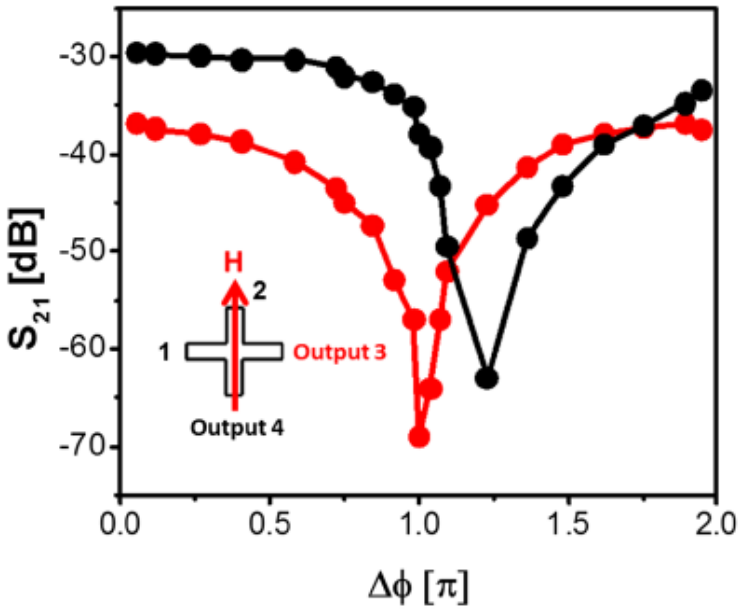

Figure 37 – Experimental data showing the change of the output signals measured at port #3 (red curve) and port #4 (black curve) as a function of the phase difference between the waves excited at ports #1 and #2. The direction of the bias magnetic field is shown in the inset. [77] *AIP Adv.* 7(5), 056633 (2017), with the permission of AIP publishing under CC BY license, link: https://creativecommons.org/licenses/by/4.0/

`

3.1.2. Significance of the obtained results

The experimental results show prominent spin wave interference effect in YIG cross junction. The maximum output voltage was observed in the case of constructive spin wave interference, when spin waves excited at ports 1 and 2 come in phase. The minimum output voltage occurs in the case of destructive spin wave interference, when two spin waves are coming with a π phase difference. The On/Off ratios (i.e. maximum voltage / minimum voltage) exceed 30 dB for all three directions of the bias magnetic field as shown in **Figure 36**. The results of experimental studies confirm the hypothesis of non-zero MSSW and BVSW overlap due to the shape magnetic anisotropy. The interference effects are observed in a narrow frequency range in agreement with equation (18). In addition, the experimental data have provided on spin wave interference in the narrow frequency range where both MSSW and BVSW type of spin wave can propagate. The obtained data are important for the design of micro- and nanometer size spin wave devices.

3.2. Spin wave excitation in sub-micrometer thick $Y_3Fe_5O_{12}$ films fabricated by pulsed laser deposition on garnet and silicon substrates: A comparative study [80]

YIG crystals are among the most promising materials due to intrinsically low magnetic damping [5]. The development of YIG nanostructures on a silicon substrate is critically important for the integration of magnonic components with conventional electronic circuits. This has led to a great deal of interest in the fabrication of high quality

`

YIG films on silicon substrates. Moreover, YIG has been grown on Si and other non-garnet substrates by a range of techniques including pulsed laser deposition (PLD) [81, 82], sputtering [83-86], chemical solution deposition [87], and chemical vapor deposition (CVD) [88].

Spin wave excitation and propagation were measured in sputtered YIG/Si and differed significantly [89] compared to that of YIG/GGG [90]. In this section, the experimental data on spin wave excitation and propagation in 700 nm thick planar $Y_3Fe_5O_{12}$ (YIG) films fabricated on gadolinium gallium garnet $Gd_3Ga_5O_{12}$ (GGG) and silicon substrates by PLD were presented. The spin wave spectroscopy technique was performed for measurements, using a set of micro-antennas placed directly on the thin film surface. Moreover, the spectra collected for YIG/GGG and YIG/Si were compared and analyzed. Understanding the mechanisms leading to the spin wave damping modification is the key to low loss spin wave devices compatible with conventional silicon-based technology.

3.2.1. Experimental procedures and results

In preparing the samples, YIG thin films were grown on GGG (111) and Si (100) substrates using PLD at 700 ˚C in 20 mTorr oxygen pressure at a growth rate of 1.15 nm per 1000 pulses. The Si substrates were lightly Boron-doped p-type Si with a resistivity of 10-20 Ω cm. Using a profilometer, the thickness of the films was 690.6 nm. The YIG/Si was processed further, and was annealed using rapid thermal annealing (RTA, Modular Process Tech, RTP-600S) from room temperature (RT, 25 ˚C) to a set point of

`

800 ˚C within 30 seconds, held for 3 minutes, and decreased to RT within 4 minutes, to crystalize the film.

The samples were characterized using AFM and SEM, as shown in **Figure 38**. The film on Si is rougher, with an rms roughness of R_{rms} = 7.7 nm, and topography which may indicate grain size of the order of 150 nm. The film on GGG appears very flat with a roughness R_{rms} < 1 nm despite the large thickness of the film. The SEM image of the film on Si reveals cracks spaced ~10 μm apart. This cracking relieves the tensile thermal mismatch strain that develops in the YIG on cooling from the anneal temperature because the thermal expansion coefficient of YIG, 10.5×10^{-6} K^{-1}, is larger than that of Si.

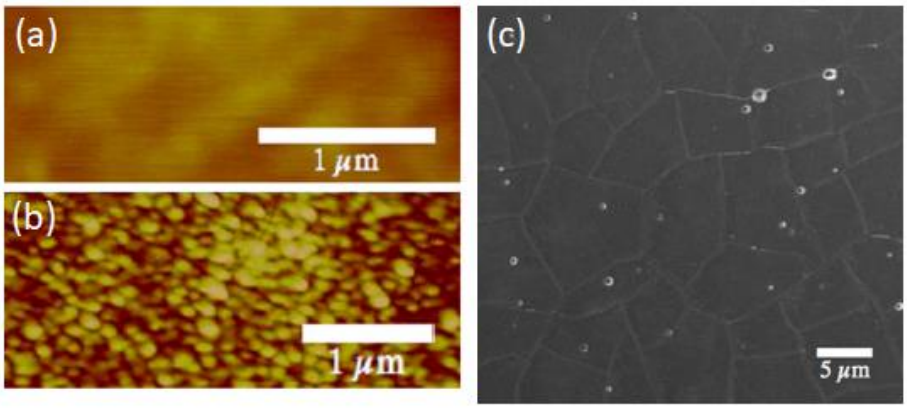

Figure 38 – (a) AFM image for YIG on GGG. (b) AFM image for YIG on Si. (c) SEM image of YIG on Si. Multiple cracks are on the surface due to thermal expansion mismatch. [80] *J. Appl. Phys.* 122(12), 123904 (2017), with the permission of AIP publishing.

The experiment was performed using the spin wave spectroscopy technique. Spin waves are excited and detected by a pair of microscale conductors (e.g. micro-antennas for transmission, or coplanar transmission lines for reflection) placed in the vicinity of the sample. **Figure 39**(a) shows the photo of the device with micro-antennas on the surface of

`

YIG. There are four conductors made of Ti/Au wires (e.g. 8 nm of Ti and 88 nm of Au). The thickness of the wires was checked by AFM. The width of the wire is about 9 μm and the length of the parallel sections is 3 mm. The antennas are placed directly on the YIG surface. The antennas are separated by 10, 50, and 500 μm as shown in **Figure 39**(b). To minimize direct coupling between the excitation and detection ports, only two antennas separated by 500 μm were used as shown in **Figure 39**(c). **Figure 39**(d) shows the complete packaged device ready for measurements.

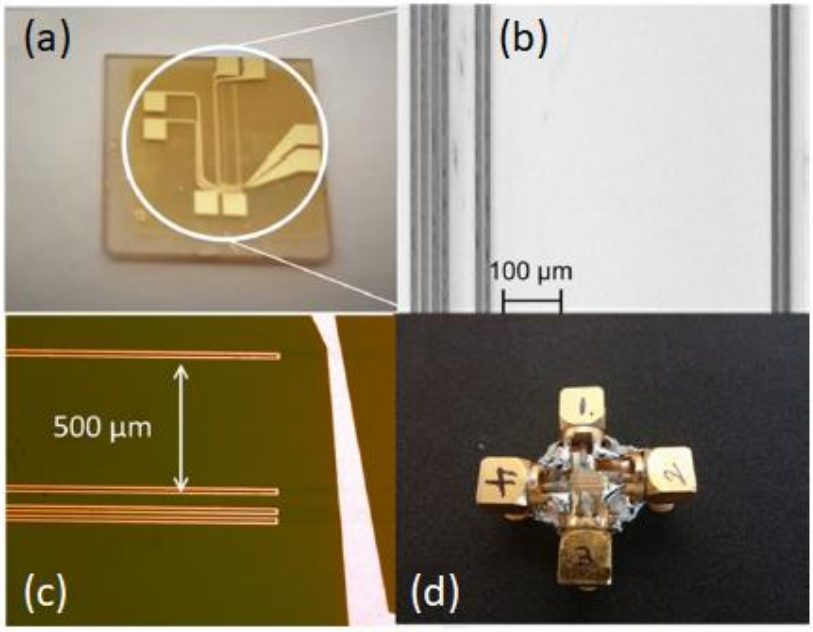

Figure 39 – (a) A photo of the device with micro-antennas on top. (b) SEM image of the sample and micro-antennas. The antennas are placed directly on the YIG surface. The antennas are separated by 10 μm, 50 μm, and 500 μm. (c) Optical image of the working area with two conductors separated by 500 μm. (d) Photo of complete packaged device. [80] *J. Appl. Phys.* 122(12), 123904 (2017), with the permission of AIP publishing.

The schematic of the experimental setup is shown in **Figure 40**. The antennas are connected to a programmable network analyzer (PNA) Keysight N5221A, and swept the

`

frequency from 0.5 GHz to 9 GHz. The device is placed inside of an electromagnet to control the bias magnetic field from -2000 Oe to +2000 Oe. The bias magnetic field is perpendicular to the spin wave vector *k*, which corresponds to Damon-Eshbach magnetostatic surface spin waves (MSSW) [2].

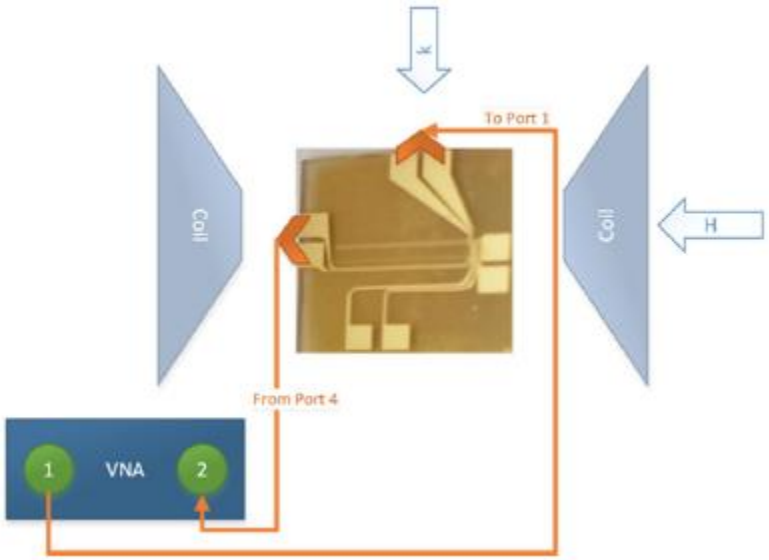

Figure 40 – Schematic of experimental setup. The device is placed in between electromagnets (coils). Bias magnetic field is applied from -2000 Oe to +2000 Oe. Micro-antennas are connected to a programmable network analyzer (VNA). The spin waves propagate perpendicular to the direction of the magnetic field (MSSW configuration). [80] *J. Appl. Phys.* 122(12), 123904 (2017), with the permission of AIP publishing.

It was observed the experimental data on microwave signal reflection (S_{11} parameter) and propagation (S_{21} parameter) in both YIG/GGG and YIG/Si, shown in **Figure 41** and **Figure 42**, respectively. Magnetic fields were applied from 0 to 2500 Oe, with frequency swept from 1.5 to 7 GHz.

`

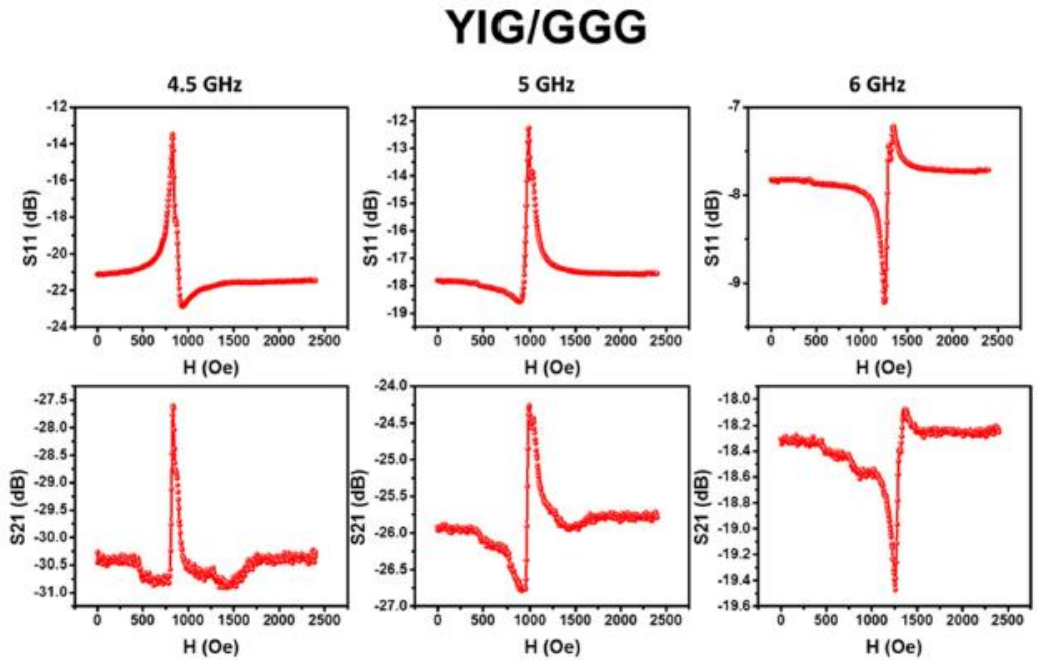

Figure 41 – Experimental results of reflection (S_{11}) and transmission (S_{21}) spectrums in YIG/GGG sample. The graphs show S_{11} and S_{21} parameters as a function of magnetic field for the selected frequencies at 4.5, 5, and 6 GHz. [80] *J. Appl. Phys.* 122(12), 123904 (2017), with the permission of AIP publishing.

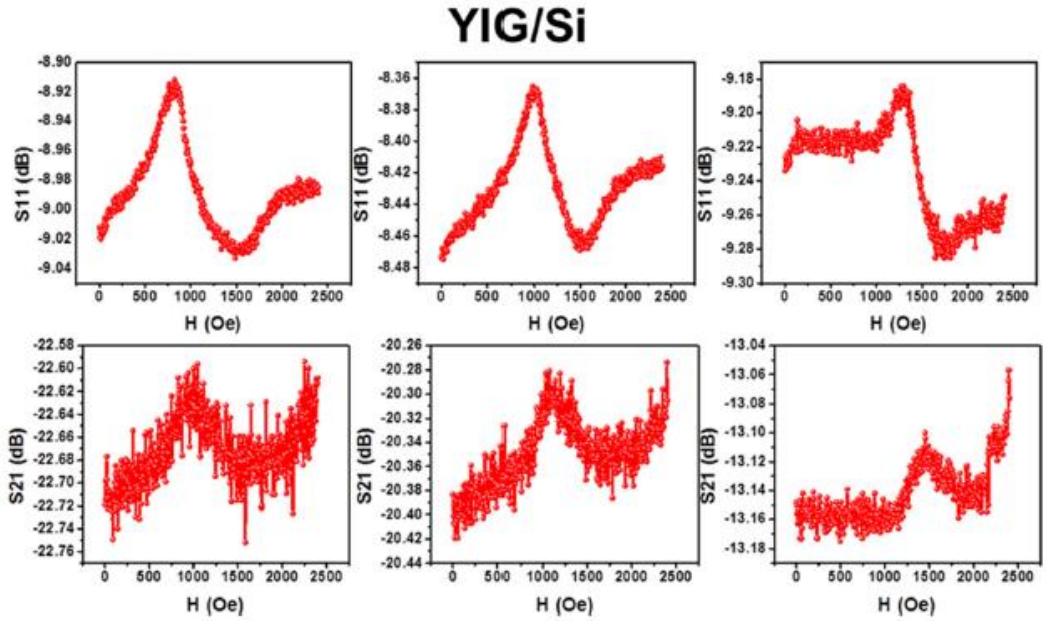

Figure 42 – Experimental results of reflection and transmission spectrums in YIG/Si. The graphs show S_{11} and S_{21} parameters as a function of magnetic field for the selected frequencies at 4.5, 5, and 6 GHz. The signals are relatively noisy than in YIG/GGG sample. [80] *J. Appl. Phys.* 122(12), 123904 (2017), with the permission of AIP publishing.

`

The peaks in the absorption spectra correspond to the frequency of the most efficient SW excitation. These frequencies increase with increasing bias magnetic field. The scalar forward gain S_{21} is the ratio of the power of the microwave signal detected on the receiving antenna to the power of the current generating the spin waves. The S_{21} parameter accounts for the losses at spin wave generation by micro-antennas, losses during propagation between the generating and detecting antennas, and losses at the detection antenna.

In **Figure 43** we present a compilation of data showing S_{11} and S_{21} in a frequency range from 0.5 GHz to 8 GHz and a bias magnetic field from 0 Oe to 2500 Oe. The color scale corresponds to the S parameters in dB. The data are shown after subtraction of the signals at zero bias magnetic fields. The subtraction allows me to exclude the effect of the direct coupling between the input/output antennas from consideration. Based on these graphs, there are a few observations must be emphasized. First, the amplitude of the spin wave signals in the YIG/Si sample is much lower compared to the YIG/GGG sample. For instance, the local peaks in the S_{21} spectra corresponding to the spin wave transmission show ~3 dB amplitude in YIG/GGG compared to ~0.1 dB in the YIG/Si. This is the same for S_{11} spectra. Second, the linewidth ΔH of the spin wave resonances is about two times larger in YIG/Si compared to YIG/GGG. The latter is a direct indication of a larger damping α.

`

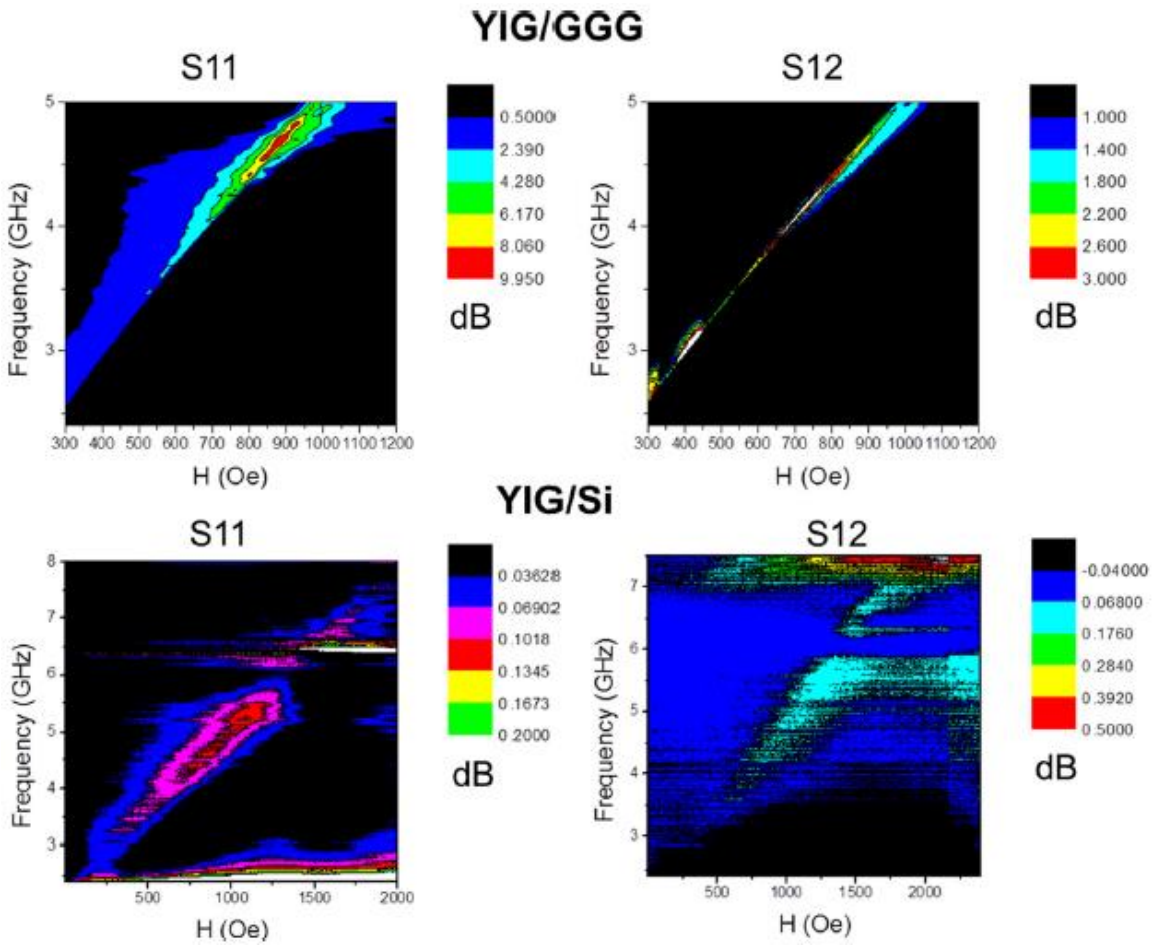

Figure 43 – Colormaps of both YIG/GGG and YIG/Si samples. Showing S_{11} and S_{21} parameters with color scale corresponds to the S parameter in dB as a function of both magnetic field and frequency. [80] *J. Appl. Phys.* 122(12), 123904 (2017), with the permission of AIP publishing.

In order to extract the value of M_{eff}, the effective magnetization, the SW frequency as a function of the bias magnetic field is plotted and shown in **Figure 44**. The blue and red markers correspond to the $k = 0$ and $k = 0.35$ μm^{-1} in the absorption spectra S_{11} presented in **Figure 43**. The low frequency field border of the spectrum is defined by $k = 0$, while the high frequency border corresponds to $k = \pi/w$, where w is the width of the microstrip antenna (e.g. $w = 9$ μm correspond to $k = 0.35$ μm^{-1}) [91]. Fitting to Kittel's

`

formula gives us $4\pi M_{eff}$ = 2060 ± 61 Oe at k = 0, and $4\pi M_{eff}$ = 1888 ± 6 Oe at k = 0.35 μm^{-1} in YIG/GGG. As for the case of YIG/Si, $4\pi M_{eff}$ = 1511 ± 172 Oe at k = 0, and $4\pi M_{eff}$ = 1678 ± 6 Oe at k = 0.35 μm^{-1}. These extracted values of are in good agreement with the results obtained from the hard-axis loops measured by VSM, which were 1850 Oe for YIG/GGG and 1500 Oe for YIG/Si.

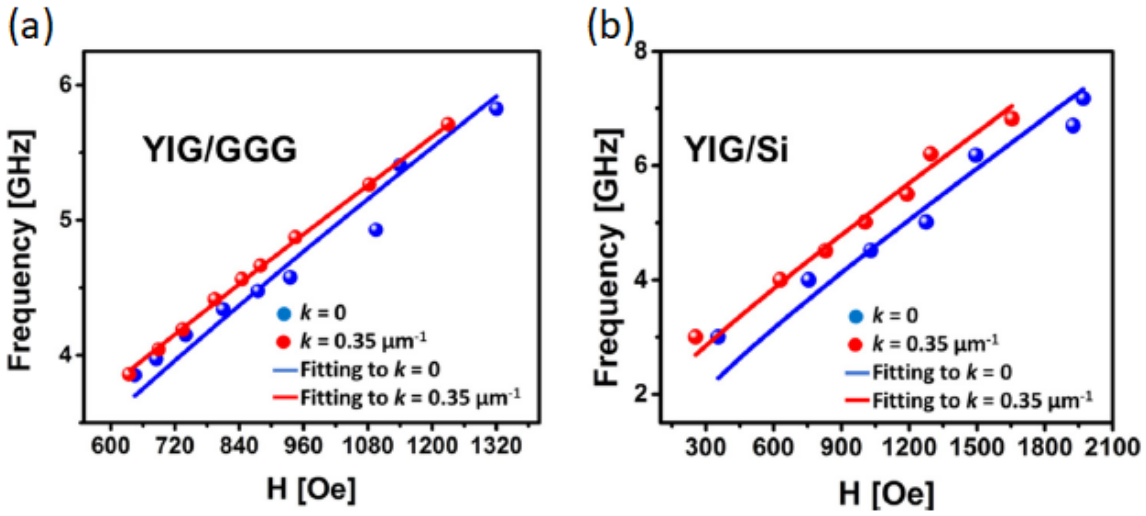

Figure 44 – Experimental data: FMR frequency as a function of the bias magnetic field for (a) YIG/GGG and (b) YIG/Si samples. The red and blue markers correspond to the center and to the low *k* edge frequencies of the FMR peak extractred from the S_{11} presented in Figure 43. The solid straight lines for both red and blue colors are based on Kittel's formula for fitting. [80] *J. Appl. Phys.* 122(12), 123904 (2017), with the permission of AIP publishing.

3.2.2. Significance of the obtained results

In section 3.2.1., the data on spin wave excitation and propagation were presented in YIG/GGG and YIG/Si samples of the same thickness fabricated by PLD. The results show significant increase of the spin wave damping in the YIG/Si sample compared to the YIG/GGG sample. The anisotropy field determined by the Kittel fitting is in good

`

agreement with the results obtained via VSM measurements. Further understanding of the mechanisms leading to the spin wave damping increase in YIG on silicon substrates, as well as management of the thermal stress in the films, is critically important for building low-loss spin wave devices compatible with conventional silicon-based technology.

3.3. Spin wave excitation and propagation in Py nanowires

YIG material is a great candidate for spin wave studies because YIG has very low spin wave damping and very long coherence length [5]. However, YIG is not compatible with CMOS technology due to current fabrication limitations. In contrast to YIG material's limitations of development, Py has the potential to be integrated into CMOS technology easily. Py has attracted many interests in spin wave study [92-95], owing to it having relatively low spin wave loss compared to other conducting materials.

There is great interest in fabricating and studying nanowires on different kinds of materials [96-98]. Nanowires have great potential for testing and understanding fundamental concepts about the roles of dimensionality and size on physical properties [99]. There are also many applications where nanowires can be exploited, including functional nanostructure materials, nanoelectronics, and biological sensing [99]. Therefore, this section aims to demonstrate spin wave excitation and propagation in Py nanowires structure for potential novel devices.

`

3.3.1. Experimental procedures and results

The Py sample was fabricated using the photolithography and lift-off technique. First, the fabrication process started off with the photolithography process to make a rectangular shape of a window (3 mm × 700 μm) on the Si substrate. Then, used the AJA sputtering system with Ar^+ gas pressure at 4.4 mTorr and RF power at 100% to deposit 60 nm of Py in the window. The lift-off process was then performed to remove undesired areas of photoresist and Py. In order to create a series of nanowires, the FIB system was operated to mill the patterns of nanowires at the center of Py sample. Each Py nanowire has the dimension 50 μm × 230 nm, with the gap between nanowires at 80 nm. **Figure 45** shows the SEM images of the Py nanowires sample.

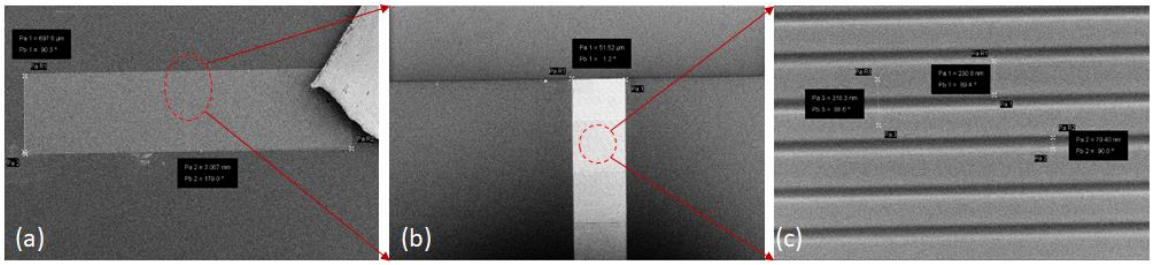

Figure 45 – SEM images of Py nanowires sample. (a) A rectangular shape of Py deposited on top of Si/SiO_2 substrate. (b) Zoom-in image on the center of Py sample. (c) Enlarged image of nanowires.

For better understanding in the magnetic properties of the Py nanowires sample, AFM and MFM were used for characterization. Detailed operation of AFM and MFM was explained in Chapter 2. The signature of magnetic properties can be revealed through the dual scanning option, enabling AFM and MFM at the same time. **Figure 46** shows the results of AFM and MFM. In this configuration, the magnetic field is applied along the

`

direction of nanowires. From the results, the domain structure was not observed. This means the magnetic moments are aligned along the direction of nanowires, because the demagnetization field is small and the nanowires resembled an infinite film, which does not require a large amount of magnetic field to align all the magnetic moments.

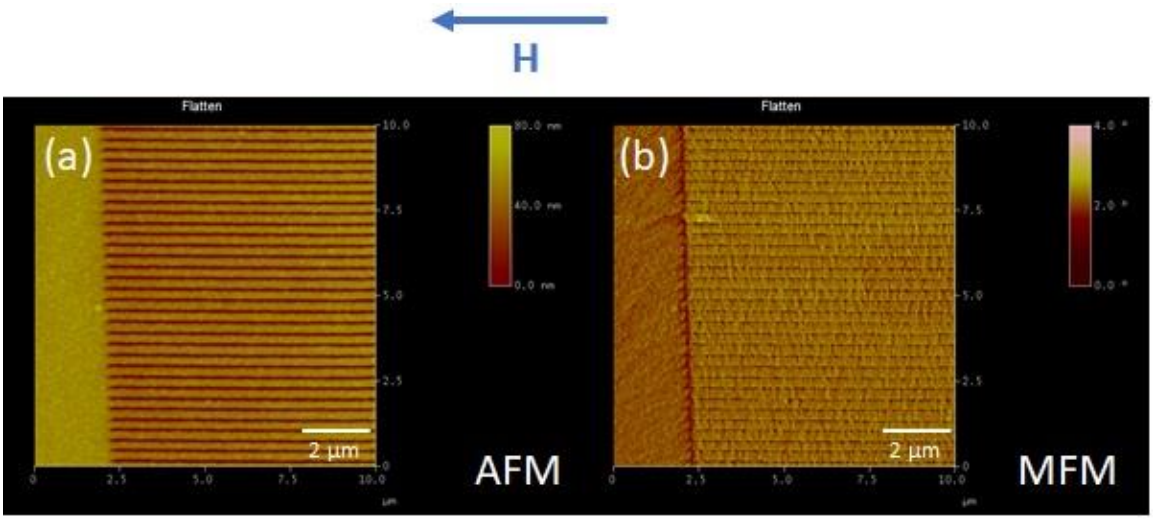

Figure 46 – Images at the junction of Py bulk and nanowires. Bias magnetic field is applied along the nanowires' direction. (a) AFM image. (b) MFM image.

Another configuration is shown in **Figure 47**. The magnetic field is applied transverse to the direction of the nanowires. From the MFM image, the domain structures can be observed, and are shown in brighter or darker spots. Since the MFM tip is magnetized, when it is scanning the surface of the nanowires, the magnetic moments will either repel or attract to the tip. As a result, they appear in brighter or darker colors, following the color scale of the phase. These domain structures are due to a larger demagnetization field and magnetic moments require a larger magnetic field to switch their directions to be the same as the bias magnetic field.

`

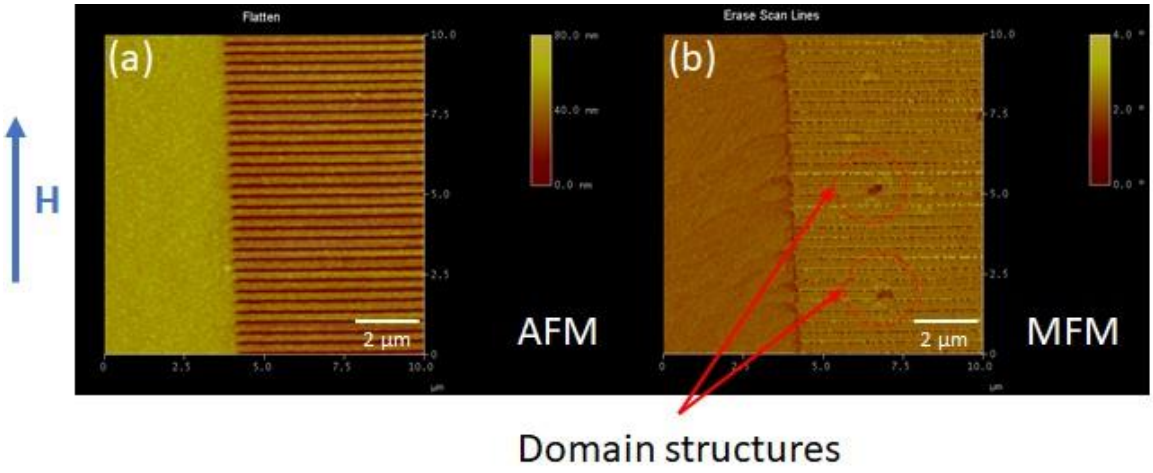

Figure 47 – Images at the junction of Py bulk and nanowires. Bias magnetic field is applied perpendicular to the nanowires' direction. (a) AFM image. (b) MFM image. Domain structures observed.

Once the basic magnetic properties of the Py nanowires sample are realized, the next step is to complete the device for spin wave study. Prior to insulator layer deposition, the sample is cleaned with acetone, methanol, and IPA. This is followed by a 500 W O_2 plasma cleaning process. SiO_2 is chosen as the sputtering target for the isolation between the Py layer and the micro-antennas. The insulator layer (SiO_2) has a thickness of 80 nm. Four micro-antennas were fabricated on the SiO_2 using E-beam lithography process to open windows. Then, Ti (10 nm) as an adhesion layer was deposited between SiO_2 and Au (200 nm) using the E-beam evaporator Temescal BJD 1800. Lastly, performed a lift-off process, and then packaged the device. **Figure 48**(a) shows the location of micro-antennas, and the antenna (P1) is patterned on top of the nanowires while antennas (P2-P4) are on top of the Py film. The packaged device, shown in **Figure 48**(c), is then placed inside of an electromagnet for the uniform magnetic field. To perform spin wave spectroscopy, the VNA was connected to two selected micro-

`

antennas of interests. For instance, to study the characteristics of spin wave transport from Py nanowires to Py thin film, we connected antenna P1 to port 1 of VNA for RF current source injection and connected antenna P3 to port 2 of VNA for inductive voltage detection. The VNA and electromagnet are shown in **Figure 48**(b) and **Figure 48**(d), respectively.

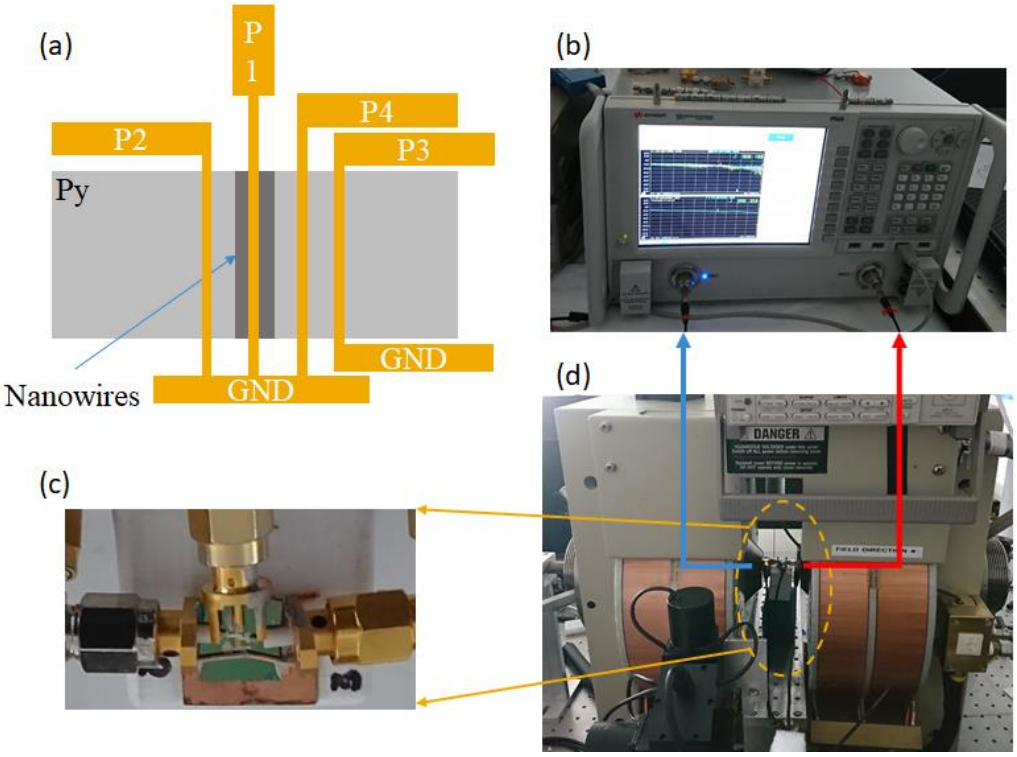

Figure 48 – (a) Schematic design of micro-antennas on the Py nanowires device. (b)-(d) Experimental setup using spin wave spectroscopy technique. (b) Photo of PNA. (c) Packaged device with SMA connectors. (d) Photo of GMW electromagnet with device inside.

The data were collected with a bias magnetic field applied from -600 Oe to +600 Oe and frequency range from 1.5 GHz to 7.5 GHz. **Figure 49**(a)-(f) show extracted data at selected frequencies for the results of reflection spectrum in Py film. The experiment was

`

performed in MSSW configuration. Based on the data, there are peaks shifting apart to different magnetic fields as the frequency increases. For better analysis, the positions of these peaks were fitted with Kittel's formula, and the results are shown in **Figure 50**. The estimated wavevector *k* is excited by one micro-strip antenna:

$$k = \sqrt{k_x^2 + k_y^2} \tag{19}$$

$$k_x \approx \frac{\pi}{w} = \frac{\pi}{10} \cdot 10^4\ cm^{-1} = 3.14 \cdot 10^3\ cm^{-1} \tag{20}$$

where *w* is 10 μm for the width of antenna.

$$k_y \approx \frac{2\pi}{\lambda} = \frac{\pi}{\beta} \cdot 10^4\ cm^{-1} = 1.365 \cdot 10^5\ cm^{-1} \tag{21}$$

where width of antenna β is 230 nm, and $k_y \gg k_x$, so k_x is negligible. Since the Py thickness $d = 60\ nm$, $kd = 0.819$. By analyzing the dispersion relation for spin waves with calculated wavevector *k*, it is reasonable to conclude that frequency of MSSW is close to FMR (Kittel's formula equation (6)). Such fitting indicates the evidence of spin wave excitation; i.e., the resonant peaks are existing at a certain magnetic field with a corresponding frequency and have strong relation to Kittel's formula. Furthermore, in **Figure 50**, the blue markers were extracted spin wave peaks from **Figure 49**(a)-(f), and these extracted peaks were fitted using Kittel's formula, shown in the red color line. From these data plots, it can be concluded that there are good agreements with experimental data and theoretical calculation at saturation magnetization ≈ 7591 Oe for the Py film.

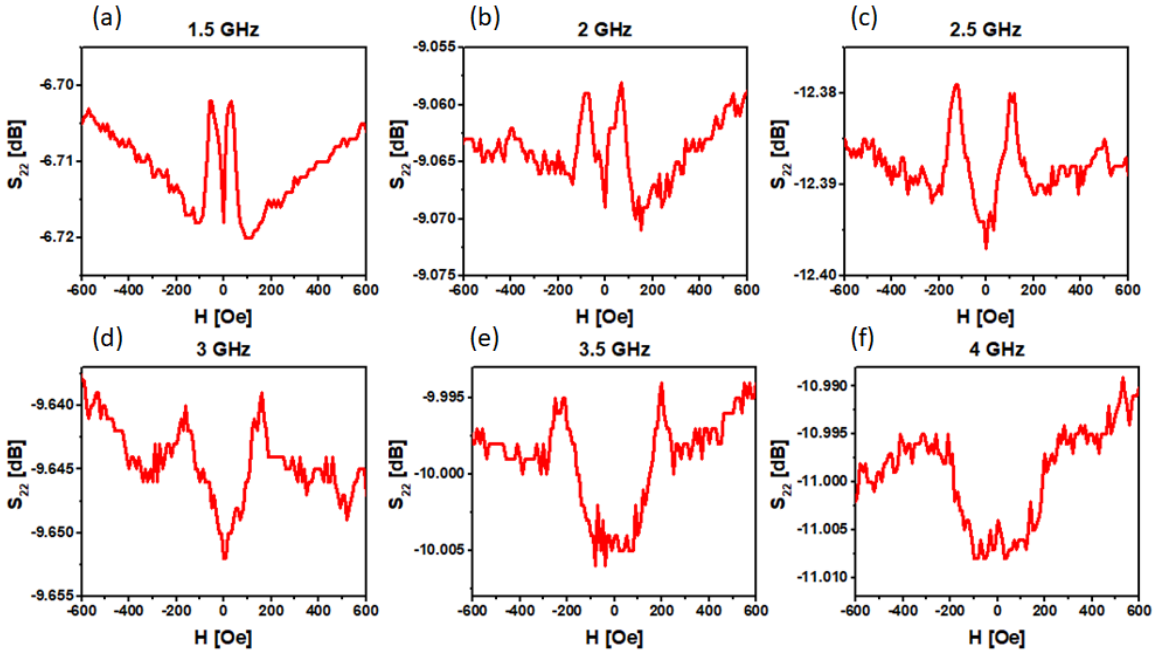

Figure 49 – (a)-(f) Experimental data of spin wave reflection (S_{22}) spectrums. The bias magnetic field is applied from -600 Oe to +600 Oe at selected frequencies: 1.5, 2, 2.5, 3, 3.5, and 4 GHz. The spin wave peaks are shifting with corresponding frequency and magnetic field.

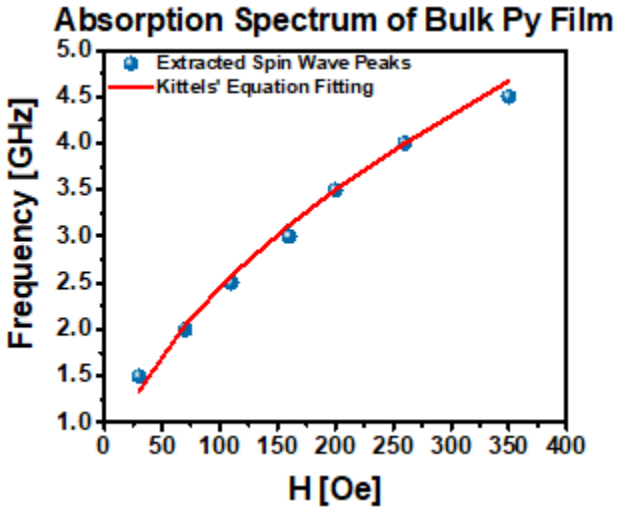

Figure 50 – Experimental data fitted with theoretical calculation. The blue markers are extracted spin wave peaks from Figure 49. The red curve is based on Kittel's equation for fitting, which gives agreement with the experimental data. The saturation magnetization is $4\pi M_s$ = 7591 ± 972 Oe.

`

In addition to spin wave excitation, the spin wave propagation from Py nanowires to Py thin film was performed. **Figure 51** shows the colormap of spin wave propagation with bias magnetic field from -150 Oe to +150 Oe and frequency range from 1.5 GHz to 3.0 GHz. To exclude the effect of the direct coupling between the antennas, the transmission spectrum has been subtracted to the value at zero bias magnetic. The blue color represents the spin wave propagation region. From the data, the signature of non-reciprocity effect was observed for the opposite direction of bias magnetic fields. One of the reasons for this is the effect of the domain structures. That is, the existence of domain structures are obstacles for the spin wave transport.

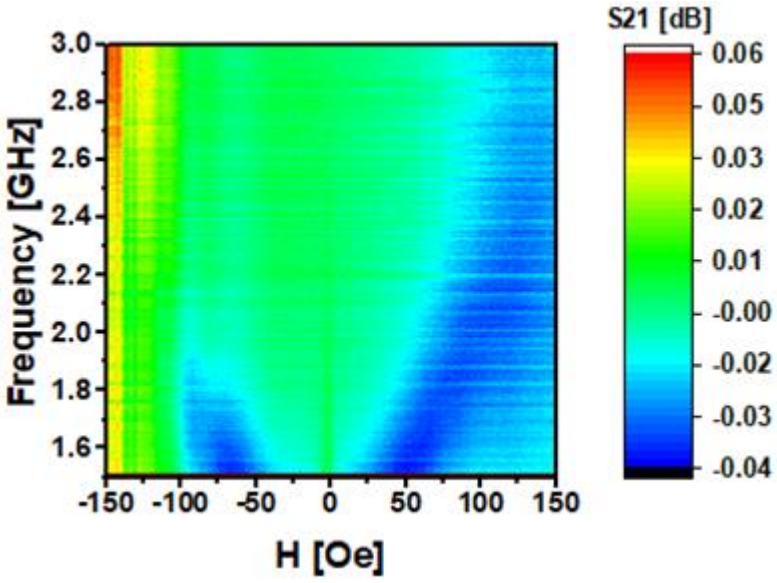

Figure 51 – Colormap of spin wave transmission (S_{21}) spectrum. The results have subtracted the value at zero bias magnetic field: $S_{21} = S_{21}(H) - S_{21}(H = 0)$ for data optimization. The blue color indicates the existence for spin wave excitation and propagation.

In order to improve spin wave detection sensitivity, another experimental setup was conducted and shown in **Figure 52**. In this setup, the device is placed inside

`

electromagnets for the bias magnetic field. Then, connect input antenna (e.g. P3) to a directional coupler's transmitted port and connect output antenna (e.g. P1) to another directional coupler's input port. Next, two directional couplers are connected to an amplifier. Lastly, the VNA sends an RF signal into one of the directional coupler's coupled port and detects inductive voltage from another one's coupled port. The active ring circuitry between the device, directional couplers, and amplifier has 0 dB loss. Moreover, the amplifier has adjusted its amplification to the threshold point to prevent auto-oscillation. Through small variation of the bias magnetic field, the amplitude of spin wave peak will change dramatically at the corresponding frequency.

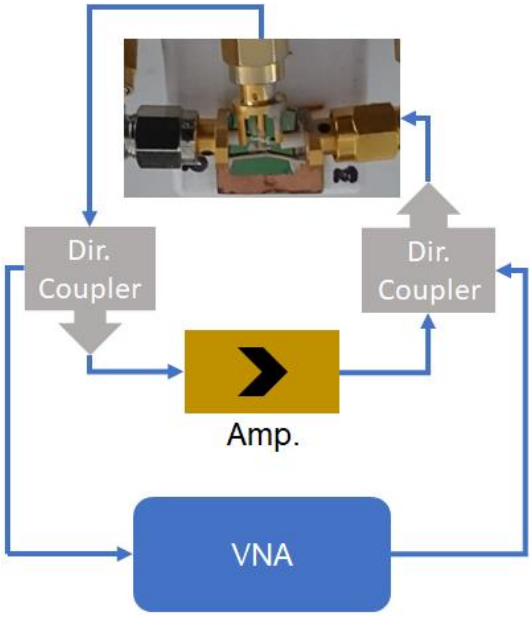

Figure 52 – Experimental setup for active ring circuitry. This setup consists extra components: two directional couplers and an amplifier. The circuitry loop of the directional couplers, the amplifier, and the device has a loss of 0 dB. The directional couplers are connected to VNA for spin wave signal generation and detection.

`

Figure 53(a) shows the experimental data of the improved spin wave detection sensitivity. The data show selected transmission spectrums with amplitudes in arbitrary units as a function of magnetic fields. The blue markers and blue curve represent the existence of spin wave propagation from Py nanowires to Py thin film. In addition, theoretical calculation is performed using Kittel's formula to fit with extracted experimental data, as shown in **Figure 53**(b).

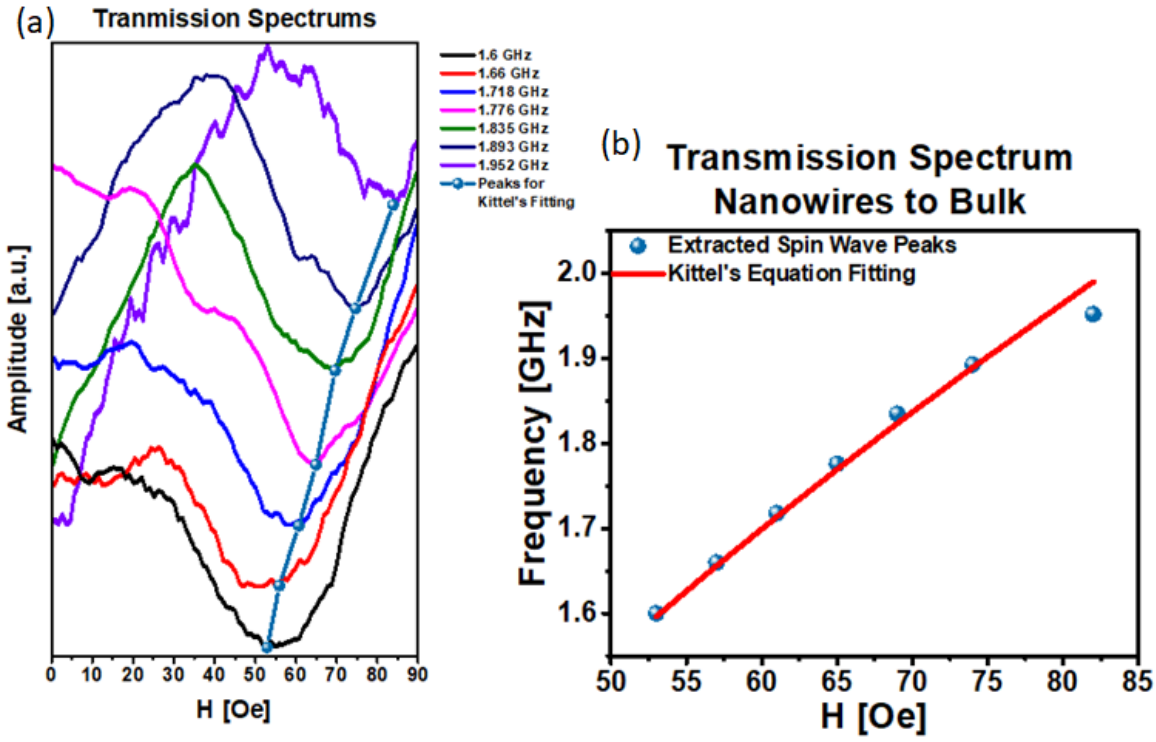

Figure 53 – (a) Experimental data for transmission spectrums using active ring setup. (b) Experimental data fitted with theoretical calculation. The blue markers are extracted from (a) for Kittel's equation fitting. The red curve is the calculation using Kittel's formula. The saturation magnetization is $4\pi M_s$ = 6079 ± 235 Oe.

The evidence of spin wave propagation between two different structures is supported by the nearly matching characteristics of the experimental data and theoretical

`

calculation. The saturation magnetization is ≈ 6079 Oe for the Py nanowires and the Py film, which is reasonable when Py nanowires have been introduced.

3.3.2. Significance of the obtained results

In this section, the spin wave excitation and propagation between two different structures, from Py nanowires to Py thin film have been presented. The domain structures were observed by characterizing the sample with AFM/MFM. For consistency of results, the images from **Figure 46** and **Figure 47** were scanned at the exact same location. Before each scan, a distinguishable mark has been located. It was created during the FIB milling process and then performed the scanning 100 μm away from it. Thus, it was to confirm the appearance of domain structures was due to the magnetic field's orientation. The selection of scanning tips for AFM/MFM is another important factor for characterization. Ultrahigh coercivity (UHC) and ultrahigh resolution (UHR) tips were used for preliminary characterization. Although the UHC tips may provide higher sensitivity, the gaps between nanowires were relatively small for the tips diameter, the observed domain structures of which were scanned by the UHR tips.

In addition, experiments based on two regions of particular interest have been carried out: at the center of the nanowires and at the junction between the nanowires and thin film. First, spin wave excitation was performed in Py thin film and Py nanowires separately. After data analysis for confirmation of spin wave excitation, spin wave propagation was performed from Py nanowires to Py thin film, and vice versa. The

`

collected S parameters have very weak spin wave signals. One of the reasons for this could be that the magnetic properties of Py nanowires were affected or reduced through the FIB milling process. The FIB injects Ar^+ ions and bombard on the surface of Py, which could damage the lattice structure of Py. For better analysis, the collected data have been subtracted from the zero bias magnetic field to remove the background signals. Besides the background removal method, the spin wave detection sensitivity was improved with the active ring setup.

Although the device has a relatively large antenna (waveguides), the spin waves were excited in lower *k*. This is because the thickness of the Py sample is small, and it may be possible to observe multiple *k* modes with larger thickness. In conclusion, the possibility of spin wave excitation and propagation in Py nanowires by spin wave spectroscopy technique was presented. The obtained results are useful for better understanding of spin wave transport in a Py nanowire structure. Further experiments may provide new routes for spin wave based applications. For instance, Py nanowires can be integrated with existing spintronics for novel logic circuits [100, 101]. Moreover, Py has low spin wave damping and can be integrated with CMOS technology easily. Therefore, spin wave study of Py nanowires is promising and cost effective for the semiconductor industry.

`

Chapter 4. Spin Wave Applications

Spintronic is a new emerging technology of electronics based on the spin degree of freedom of the electron. It is a technology that utilizes electron spin instead of electron charge to carry information, which creates new devices with the combination of conventional microelectronics with spin dependent effects [51]. Spin based applications are expanding to include, for instance, magnetic field sensors, read heads for hard drives, galvanic isolators, and magnetoresistive random access memory (MRAM) [51]. Spintronic has the potential advantages of non-volatility, increased data processing speed, decreased electric power consumption, and increased integration densities compared with conventional semiconductor devices [51]. Therefore, it is a very promising technology for both academia and industries to pursue.

4.1. Magnonic holographic imaging of magnetic microstructures [102]

This is a technique for magnetic microstructure imaging via their interaction with propagating spin waves. Magnetic micro- and nanostructures have found a wide range of practical applications starting from data storage [103] to biotechnology and medicine [104]. The understanding of magnetic dynamics is the key for building more efficient devices, including, for example, more scalable and less power consumption magnetic memory [105], accurate and robust magnetic sensors [106], and customized magnetic

`

nanoparticles for drug delivery [107]. There is a great impetus in the development of novel techniques for magnetic materials imaging and characterization.

In general, spin wave dispersion depends on the strength and direction of the bias magnetic field [79]. Even a relatively weak (e.g. tens of Oersted) magnetic field produced by a micro-scale magnet placed on top of the magnonic waveguide may result in a prominent phase shift. This phenomenon is used in Magnonic Holographic Memory [108]. In this approach, the read-out of magnetic memory elements is accomplished by measuring the inductive voltage produced by the interfering spin waves propagating through the matrix consisting of magnetic waveguides with magnetic memory elements placed on top. Furthermore, this approach to magnetic microstructures imaging is extended.

4.1.1. Experimental procedures and results

Figure 54 illustrates the ideas of magnonic holographic imaging. The testbed is a cross junction made of material with low spin wave damping. It is a four-terminal device with four micro-antennas fabricated at the edges of the cross. Two of these antennas (e.g. #1 and #3) are used for spin wave generation, while one of the other antennas (e.g. #2 or #4) is used for detecting the inductive voltage produced by the interfering spin waves. There is a microwave system which includes phase shifters and attenuators to independently control the amplitudes and the phases of the input spin waves. The object of interest is placed on the top of the junction. It may be a micro-magnet, magnetic

`

powder, or an ensemble of magnetic nanoparticles. The magnetic field produced by the object affects the propagation of spin waves through the junction and changes the output inductive voltage. The measurements are repeated for the different combinations of the input phases, where the phase at each input port is independently varied from 0 to 2π. As a result, one obtains a collection of data (Phase1, Phase 2, Inductive Voltage). Plotting the inducting voltage as a function of the input phases, a 3D image of the object in the phase-voltage space was observed.

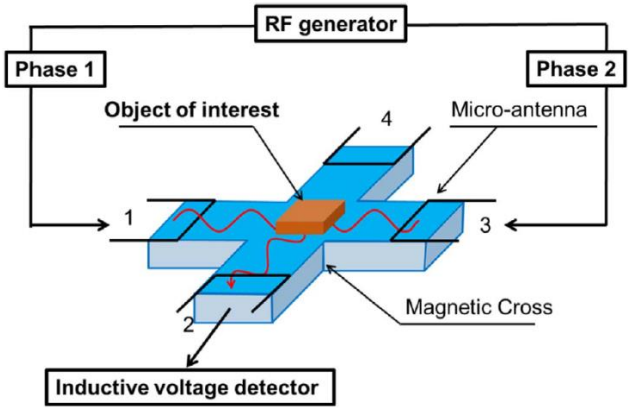

Figure 54 – Illustration of the magnonic holographic imaging technique. [102] *J. Magn. Magn. Mater.* 428 (2017), with the permission of Elsevier publishing.

The testbed is a cross junction made of single crystal YIG film grown on top of a GGG substrate using the liquid phase epitaxial method. After the films were grown, micro-patterning was performed by laser ablation using a pulsed infrared laser (λ~1.03 μm), with a pulse duration of ~256 ns and an average power of 20 W. YIG cross has the following dimensions: the length of each waveguide is 3.65 mm; the width is 650 μm; and the YIG film thickness is 3.8 μm. The saturation magnetization of the cross structure is $4\pi M_0$ = 1750 Oe. There are four Π-shaped micro-antennas fabricated on the edges of

`

the cross. Antennas were fabricated from a gold wire of thickness 24.5 μm and placed directly at the top of the YIG surface. The antennas are connected to a Keysight N5221A Programmable Network Analyzer (PNA) via a splitter, phase shifters, and attenuators. The splitter SigaTek SP542 is capable of operating at frequencies up to 18 GHz and has an insertion loss of 1.7 dB. The phase shifters are ARRA 9428 A. The phase shifters provide up to a 360 degree phase rotation at a frequency up to 8 GHz with an internal insertion loss of 0.5 dB. The step attenuators AC9011-90-11 provide an adjustable attenuation up to 10 dB with 1 dB steps. The insertion loss of the attenuators is 0.5 dB. The testbed is placed inside GMW Systems Electromagnet, which generates a uniform bias magnetic field directed in-plane with the cross surface and along the virtual line connecting antennas #1 and #3 as shown in **Figure 55**(a).

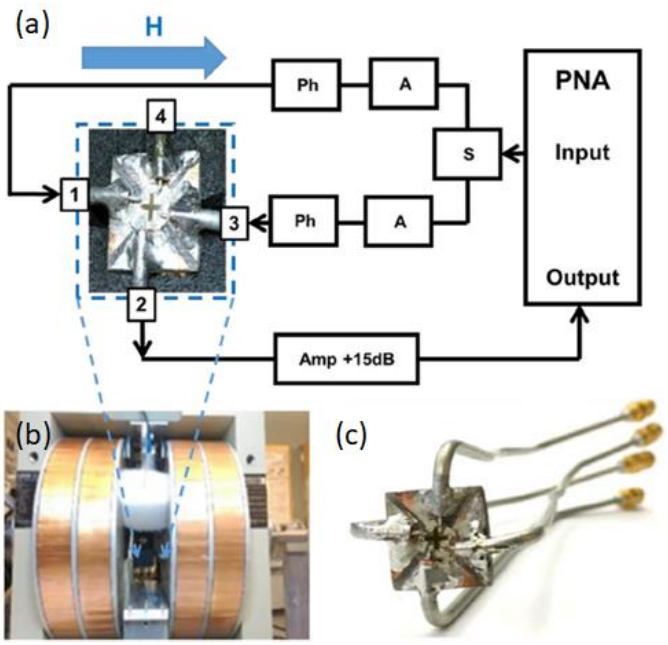

Figure 55 – (a) Schematic of experimental setup. (b) The device is placed inside of electromagnets for uniform bias magnetic field. (c) Photo of packaged device with SMA cables connected to the four ports. [102] *J. Magn. Magn. Mater.* 428 (2017), with the permission of Elsevier publishing.

`

Prior to the experiments, a combination of the operational frequency f = 3.442 GHz and the bias magnetic field H = 627 Oe were calculated, which shows prominent propagation for the BVMSW and MSSW types of waves. The maximum range of the wave numbers can be estimated as follows [79]:

$$\Delta k \leq \frac{2\pi\Delta f}{v_g} \tag{22}$$

Taking Δf = 120 MHz and $v_g = 3 \times 10^6$ cm/s, the maximum wave number k is around 120 cm^{-1}, which correspond to the wavelength of 500 μm.

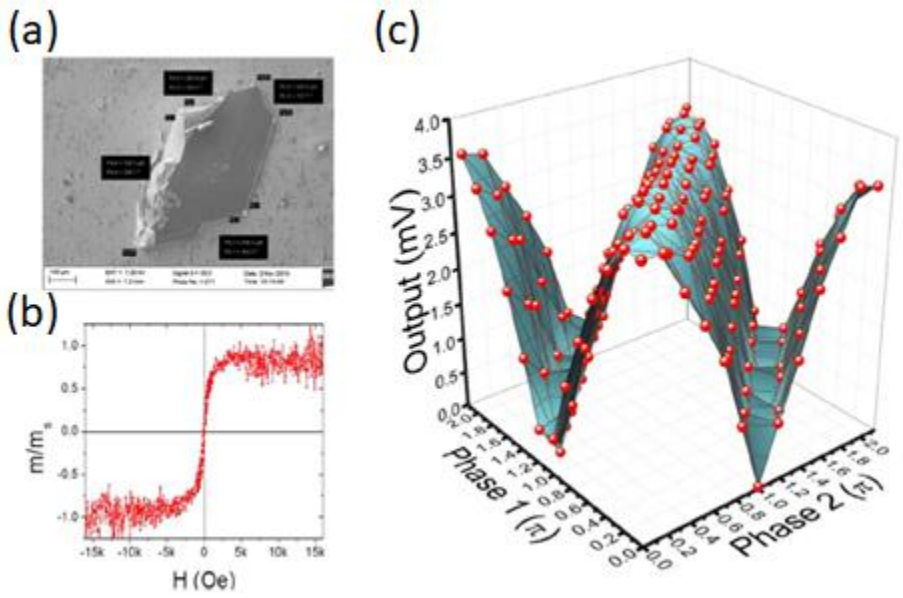

Figure 56 – (a) SEM image of a piece of MFM tip from highly doped silicon with 40 nm Co coating. (b) Results of VSM measurements showing the M-H loop of the object. The saturation magnetization is around 2500 Oe. (c) Holographic image of the object. [102] *J. Magn. Magn. Mater.* 428 (2017), with the permission of Elsevier publishing.

`

Figure 56 shows an obtained holographic image of a piece of MFM tip made from highly doped, single crystal silicon, with 40 nm Co coating (product of Nanoworld company). From **Figure 56**(a), the sample appears as trapezoidal shape. It has the following dimensions: 524.2 μm × 283.4 μm. The thickness of the sample is approximately 1 mm. There are maxima around 3.5 mV of the inductive voltage. The absolute minimum voltage corresponding to the destructive spin wave interference is 0.394 mV.

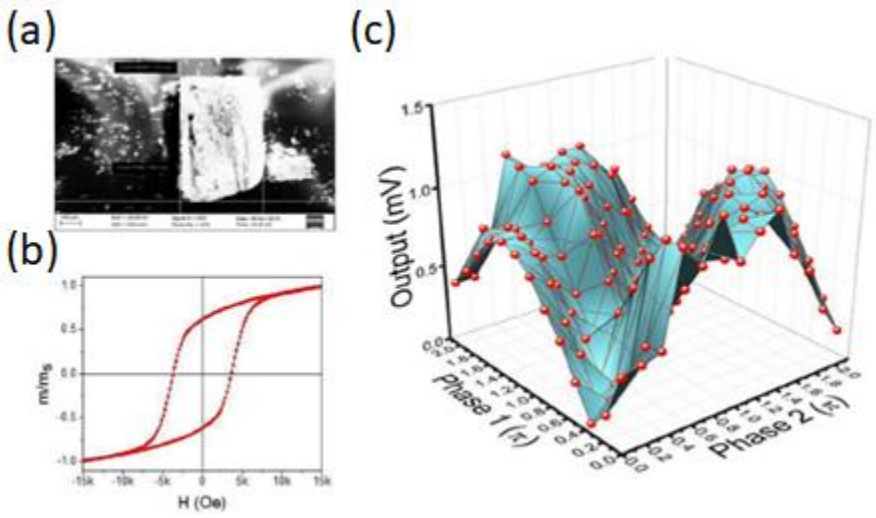

Figure 57 – (a) SEM image of $SrFe_{12}O_{19}$ sample. (b) Results of VSM measurements showing the M-H loop of the object. The saturation magnetization is around 10 kOe and coercivity at 3.6 kOe. (c) Holographic image of the object. [102] *J. Magn. Magn. Mater.* 428 (2017), with the permission of Elsevier publishing.

Figure 57 shows data obtained from a $SrFe_{12}O_{19}$ sample. $SrFe_{12}O_{19}$ is a hard-permanent magnet with dimensions 778.3 μm × 426.2 μm × 1 mm. Based on the data, there are multiple maxima and minima of non-equal height and depth, which is different from the previous data presented. The absolute maxima of inductive voltage is 1.2 mV.

`

There are multiple local maxima of the inductive voltage between 1.05 – 1.13 mV. The absolute minima voltage corresponding to the destructive spin wave interference is 0.066 m. Local minima of the inductive voltage appear at the level less than 0.5 mV. The maximum voltages are detected at symmetric phase combinations: (0.6π, 1.8π) and (1.8π, 0.6π). This sophisticated inductive voltage landscape reflects the strong and non-uniform magnetic field produced by the sample.

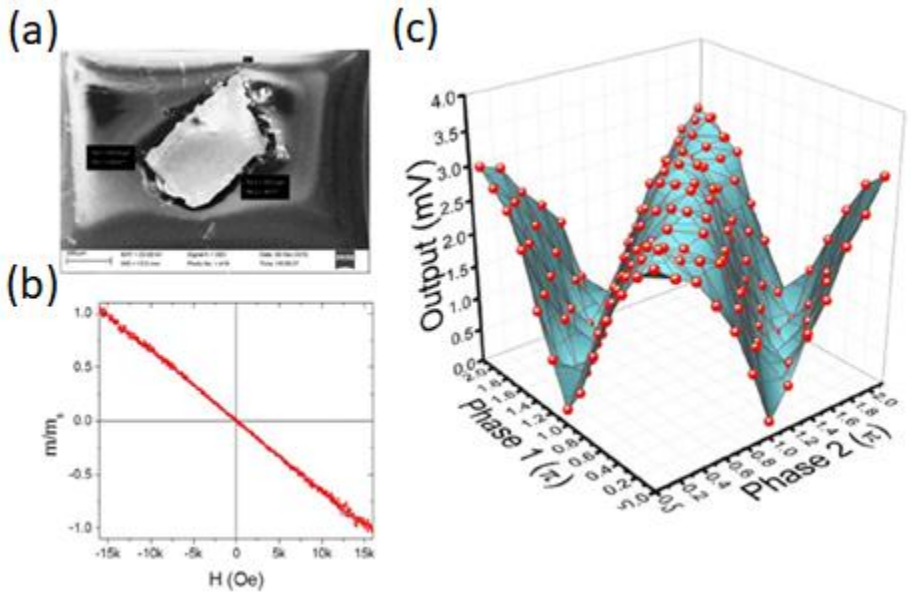

Figure 58 – (a) SEM image of the copper sample. (b) Results of VSM measurements showing the M-H loop of the object. It is a diamagnetic response. (c) Holographic image of the object. [102] *J. Magn. Magn. Mater.* 428 (2017), with the permission of Elsevier publishing.

A non-magnetic conducting sample, copper, was used to validate the hypothesis that the origin of multiple maxima and minima is due to the effect of the local magnetic field on the spin wave propagation. The sample has dimensions of 573.0 μm × 322.3 μm × 1 mm. In **Figure 58**(c), the maximum inductive voltage obtained for the copper sample is

`

3.0 mV, while imaging only the testbed is 3.7 mV. This difference can be explained by taking into account additional losses introduced to spin wave transport by the presence of the conducting material [79]. Therefore, the presence of a non-magnetic conducting material does not change the shape of the holographic image but reduces the level of the output inductive voltage.

Figure 59(a)-(c) shows the simulated holographic images for the low-coercivity Si/Co sample, high-coercivity $SrFe_{12}O_{19}$ sample, and diamagnetic copper sample, respectively. There is a good agreement in the cases of Si/Co and diamagnetic samples, which mainly resemble the image of the testbed. In the case of the "strong" high-coercivity $SrFe_{12}O_{19}$ sample, since the spin wave injected from port 1 and port 3 would be propagating in the opposite direction, for one wave there would be minimal phase shift and for another, phase shift due to the strong magnet would be at the maximum. At the output, there would be minimal amplitude where the phase of the two waves coincide from the injecting port.

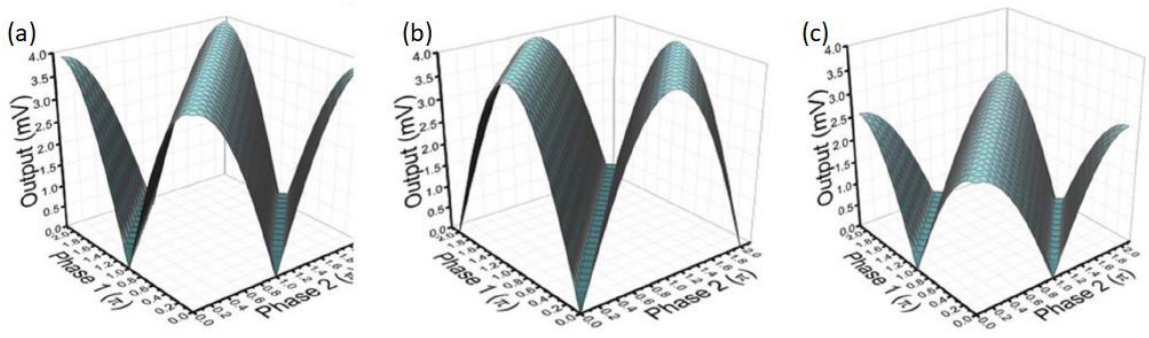

Figure 59 – Numerical modeling for holographic images of (a) MHM tip, (b) $SrFe_{12}O_{19}$ sample, and (c) copper sample. [102] *J. Magn. Magn. Mater.* 428 (2017), with the permission of Elsevier publishing.

`

Lastly, the experiments of imaging samples with different amounts of $SrFe_{12}O_{19}$ powder were carried out. **Figure 60**(c) shows the photo of different amounts of $SrFe_{12}O_{19}$ powder. The experimental data and numerical modeling results are shown in **Figure 61** for three different cases. Experimental data for a 0.3 mg sample has a maximum inductive voltage of 3.5 mV, which resembles the results for the testbed without placing the object on top. The reason can be explained by measuring the small amount of magnetic powder. The image changes significantly for the 0.75 mg sample. This difference can be explained by the asymmetry in the phase changes for the two interfering spin waves provided by the sample. The latter smashes the interference effect by lowering maxima and enhancing minima due to the dephasing. For the 1.5 mg sample, the maxima and minima correspond to the constructive and destructive spin wave interference. However, the position of maxima and minima are inverted due to the asymmetry and a π-phase shift between the interfering waves produced by the sample.

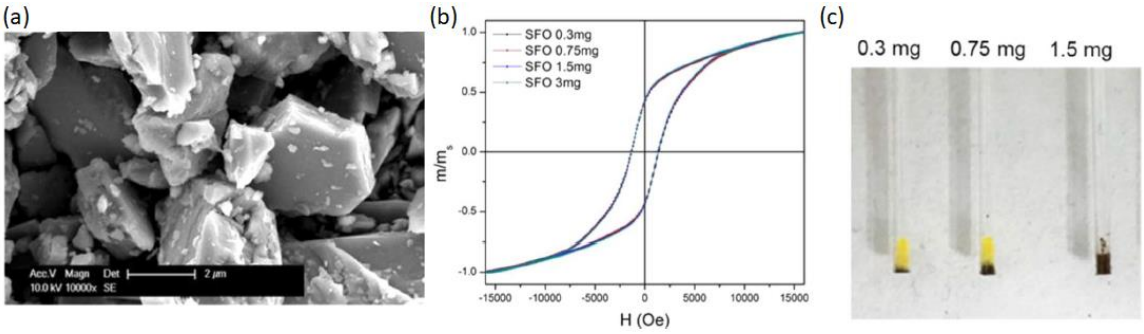

Figure 60 – (a) SEM image of the $SrFe_{12}O_{19}$ powder sample. (b) Results of VSM measurements showing M-H loop of the $SrFe_{12}O_{19}$ powder samples. The curves show the sample containing 0.3 mg, 0.75 mg, and 1.5 mg of the $SrFe_{12}O_{19}$ powder. (c) Photo of the $SrFe_{12}O_{19}$ powder samples with different amounts to be placed on the testbed. [102] *J. Magn. Magn. Mater.* 428 (2017), with the permission of Elsevier publishing.

`

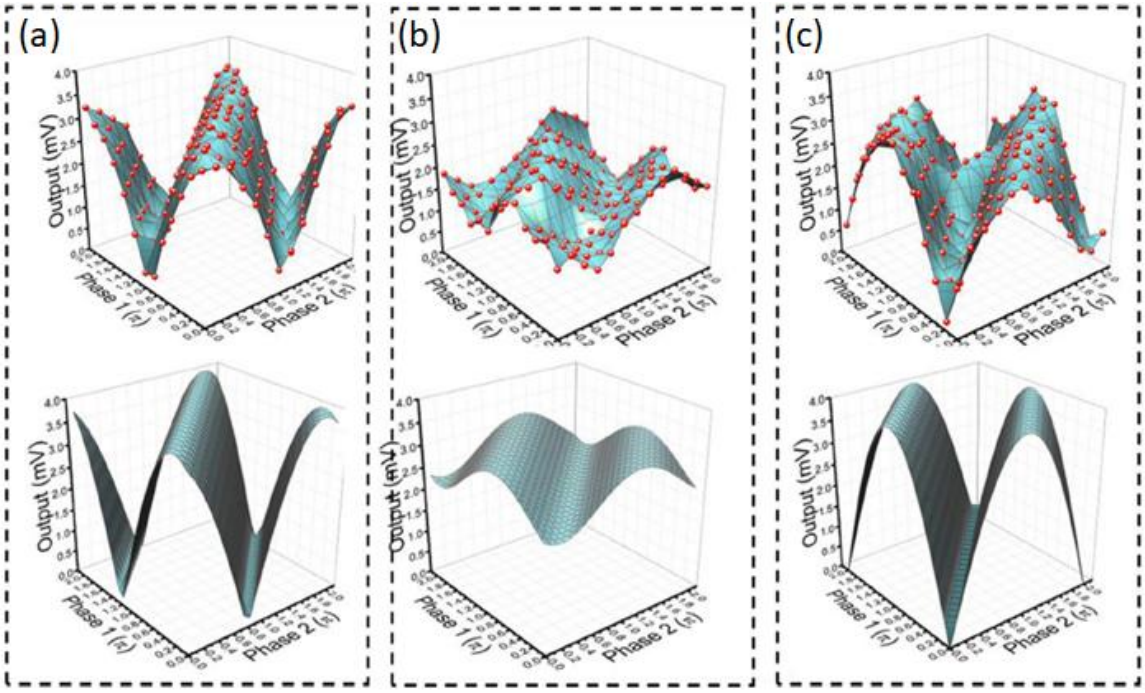

Figure 61 – Experimental and numerical modeling results showing the holographic images of the $SrFe_{12}O_{19}$ powder samples. (a) Sample with 0.3 mg of $SrFe_{12}O_{19}$ powder. (b) Sample with 0.75 mg of $SrFe_{12}O_{19}$ powder. (c) Sample with 1.5 mg of $SrFe_{12}O_{19}$ powder. [102] *J. Magn. Magn. Mater.* 428 (2017), with the permission of Elsevier publishing.

4.1.2. Significance of the obtained results

Magnonic holographic imaging is a technique based on the spin wave interaction with magnetic objects, where the magnetic field produced by the object affects the interference pattern produced by the two propagating spin waves. It allows us to visualize magnetic structures as 3D objects in a phase-inductive voltage space. This technique has a unique feature in its ability to sense magnetic objects located inside a magnetic matrix. The FMR technique also provides such a capability of resolving magnetic composites by the difference in their frequency resonance but with very limited space resolution. The

`

use of micro- and nanometer scale spin waves would preserve all the advantages of the FMR technique and complement it with ultimate space resolution. Potentially, magnonic holographic imaging may complement the existing imaging techniques and be utilized for non-destructive in-situ magnetic object characterization.

4.2. Magnetoelectric spin wave modulator based on synthetic multiferroic structure [109]

There are different approaches to spin wave signal modulation. In this section, a spin wave modulator is presented, which is a spintronic device aimed to control spin wave propagation by an electric field. The modulator consists of a ferromagnetic film serving as a spin wave bus combined with a synthetic multiferroic comprising piezoelectric and magnetostrictive materials. Multiferroics are a special type of material that possesses simultaneously electric and magnetic orders [110, 111]. This translates to the possibility to generate a magnetic field by applying an electric field. However, there are only a few room-temperature single phase multiferroic materials known today [111], e.g., $BiFeO_3$ and its derivatives. An alternative method for obtaining a structure with the magnetoelectric effect is a nanostructure consisting of two materials, a piezomagnetic film and a magnetostrictive film [112]. Magnetoelectric coupling arises as a combined effect of two phenomena: piezoelectricity and magnetostriction. In this section, a spin wave modulator consisting of a ferromagnetic film serving as spin wave bus combined with a synthetic multiferroic comprising piezoelectric and magnetostrictive materials will be presented.

`

4.2.1. Experimental procedures and results

Figure 62 shows the schematics of the spin wave modulator. From the bottom to the top, it consists of a semiconductor substrate (e.g. Si), a conducting ferromagnetic film (e.g. CoFe, NiFe), a layer of magnetostrictive material (e.g. Ni), and a piezoelectric layer (e.g. PMN-PT). The ferromagnetic film serves as a waveguide for spin waves, a spin wave bus. The metallic contact on the top of the piezoelectric layer and the conducting ferromagnetic film (ground plane) serve as a set of two electrodes to apply a voltage across the piezoelectric layer. In the absence of voltage (i.e. electric field), it is to assume that the piezoelectric layer does not influence spin wave propagation in the ferromagnetic layer. With an applied electric field *E*, the piezoelectric layer produces stress, which changes the easy-axis orientation in the magnetostrictive material. The spins of the magnetostrictive and ferromagnetic material are coupled via the exchange and dipole-dipole interactions. The magnetization change in the magnetostrictive layer influences the magnetization of the ferromagnetic layer. Thus, the stress produced by the piezo-element is equivalent to an additional external magnetic field $\vec{H}(E)$ in the ferromagnetic layer.

Spin wave propagation is well-described by the Landau-Lifshitz-Gilbert (LLG) equation [113, 114]:

$$\frac{d\vec{m}}{dt} = -\frac{\gamma}{1+\alpha^2}\vec{m} \times \left[\vec{H}_{eff} + a\vec{m} \times \vec{H}_{eff}\right] \quad (23)$$

`

where $\vec{m} = \vec{M}/M_s$ is the unit magnetization vector, M_s is the saturation magnetization, γ is the gyro-magnetic ratio, and α is the phenomenological Gilbert damping coefficient, $\vec{H}_{eff}$ is the effective magnetic field. The effective field can be expressed as [44]:

$$\vec{H}_{eff} = \vec{H}_d + \vec{H}_{ex} + \vec{H}_a + \vec{H}_b + \vec{H}(E) \tag{24}$$

where $\vec{H}_d$ is the magnetostatic field, $\vec{H}_{ex}$ is the exchange field, $\vec{H}_a$ is the anisotropy field, $\vec{H}_b$ is the external bias magnetic field, and $\vec{H}(E)$ is the effect of electric field-controlled strain-mediated coupling. The first term of equation (23) describes the precession of magnetization about the effective field and the second term describes its relaxation towards the direction of the field. Without loss of generality, I restrict the consideration to a single type of spin wave: the magnetostatic surface spin waves also known as Damon-Eshbach spin waves. The dispersion of the magnetostatic surface spin wave can be found in equation (10).

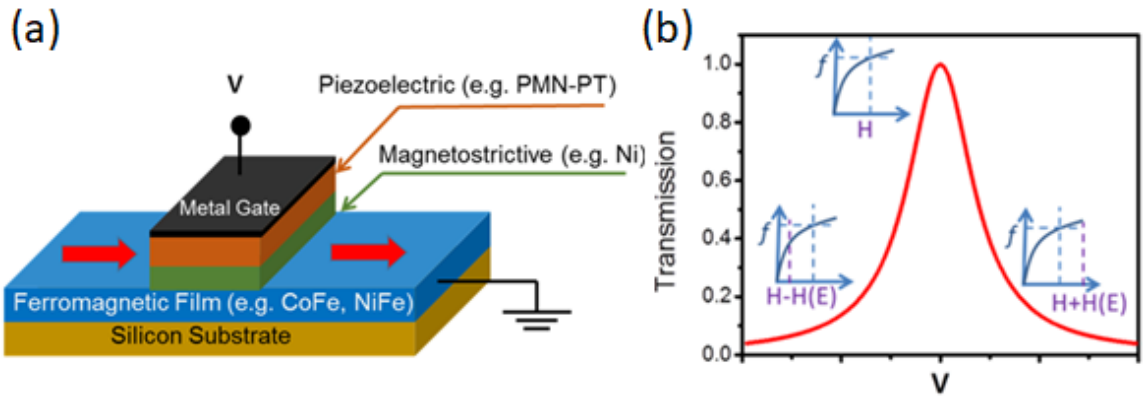

Figure 62 – (a) Schematic of the spin wave modulator. (b) Output characteristics: spin wave transmission as a function of the applied electric field. The insets illustrate the condition of switching between the spin wave conducting and non-conducting regimes. [109] *Sci. Rep.* 8, 10867 (2018), with the permission of Springer Nature publishing under CC BY license, link:
https://creativecommons.org/licenses/by/4.0/

`

First, the magnetoelectric coupling between the piezoelectric and magnetostrictive layers was studied by measuring microwave absorption in Ni as a function of the applied electric field to PMN-PT. **Figure 63** shows the schematic of the experimental setup. The sample was placed in between electromagnets GMW model 3472-70, which provides uniform magnetic field in the range from -2500 Oe to +2500 Oe. A micro-strip antenna was mechanically placed on top of the sample. The width of the antenna was 100 μm, and the length was 5 mm. The antenna was connected to a programmable network analyzer (PNA) Keysight N5221A. Using this setup, the S_{11} parameter was measured, and S_{11} parameter indicates the microwave power reflected from the sample.

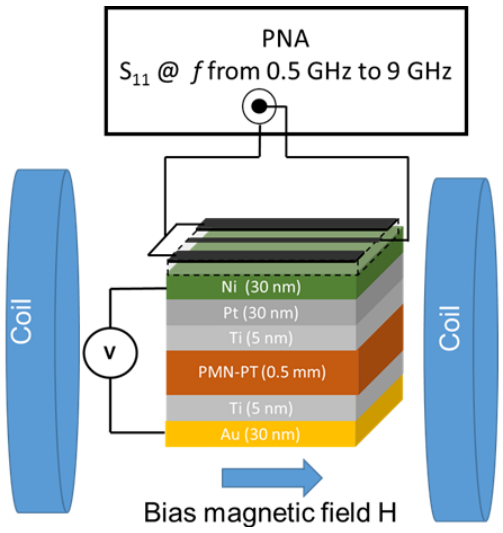

Figure 63 – Schematics of the experimental setup for microwave absorption measurements. [109] *Sci. Rep.* 8, 10867 (2018), with the permission of Springer Nature publishing under CC BY license, link: https://creativecommons.org/licenses/by/4.0/

Figure 64 shows the experimental data on microwave reflection spectrums, the S_{11} parameter. In **Figure 64**(a)-(c), the dips in the S_{11} spectra correspond to the microwave absorption in the Ni layer. There are two important notes from these data: (i) The minima

`

in S_{11} spectra shift to a higher magnetic field with increasing frequency, and this trend can be explained by equation (10). (ii) The application of an electric field increases the effective magnetic field H_{eff} because of the stress-mediated coupling. **Figure 64**(d)-(f), shows experimental data tracing the position of the peak of microwave absorption as a function of the applied electric field. In addition, the absorption peak in the S_{11} spectra follows a closed loop as a function of the applied electric field. The absorption peak shift exceeds 250 Oe in response to ± 0.6MV/m electric field.

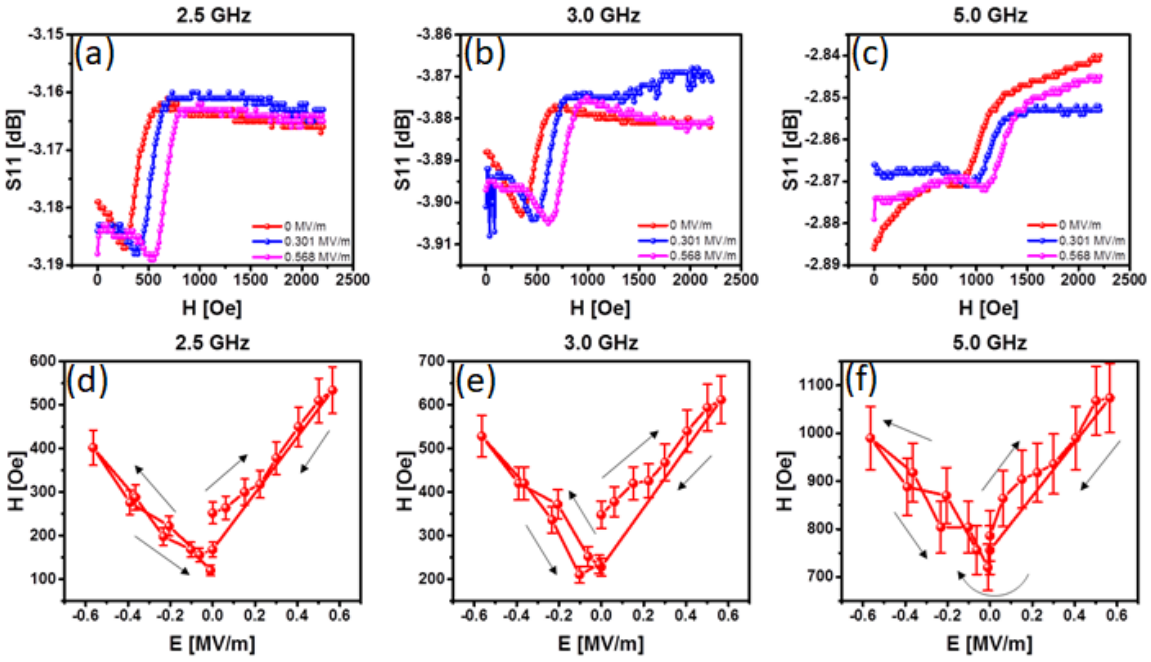

Figure 64 – Experimental data on microwave reflection spectrums, S_{11} parameter. (a)-(c) S_{11} is shown as a function of the magnetic field for three selected frequencies at 2.5, 3, and 5 GHz. The three colored curves correspond to three electric fields: 0, 0.301, and 0.568 MV/m. (d)-(f) Traces of the microwave absorption position as a function of the applied electric field. The electric field follows the path: 0 MV/m → +0.6 MV/m → 0 MV/m → -0.6 MV/m → 0 MV/m. [109] *Sci. Rep.* 8, 10867 (2018), with the permission of Springer Nature publishing under CC BY license, link: https://creativecommons.org/licenses/by/4.0/

`

Next, spin wave excitation and propagation were studied in a structure with Py spin wave bus. There are several reasons for choosing the combination of Py spin wave bus and Ni magnetostrictive layer. In contrast to Ni, Py possesses much lower spin wave damping which produces spin waves propagating over tens of microns at room temperature. Also, from the fabrication point of view, Py is well matched to Ni due to the large nickel content. The layer of magnetostrictive nickel is needed for voltage-controlled modulation as Py films maintain near-zero magnetostriction with film thicknesses above 7 nm [115].

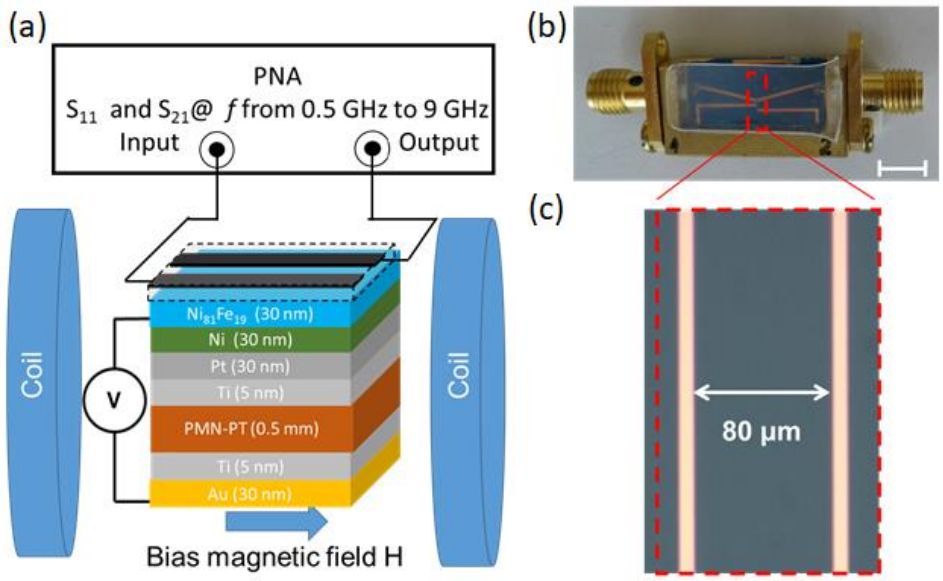

Figure 65 – (a) Schematics of the experimental setup for spin wave excitation and detection in PMN-PT/Ni/Py sample. (b) Photo of the device packaged. (c) Enlarged photo of the active area with antennas. The distance between the antennas is 80 µm. [109] *Sci. Rep.* 8, 10867 (2018), with the permission of Springer Nature publishing under CC BY license, link: https://creativecommons.org/licenses/by/4.0/

The structure of the sample is shown in **Figure 65**. The core of the structure is the same as in **Figure 63**, except for a 30 nm Py layer fabricated on top of Ni layer. To study

`

spin wave propagation, a modified micro-antennas structure was used, shown in **Figure 65** (b)-(c). One of the antennas is used for spin wave excitation, and is connected to the PNA input port. Meanwhile, the second antenna is used for inductive voltage detection and is connected to the PNA output port. The wavevector *k* of the excited spin wave can be estimated by the width of the antenna (10 μm), $k = \frac{\pi}{w} = 0.3\ \mu m^{-1}$.

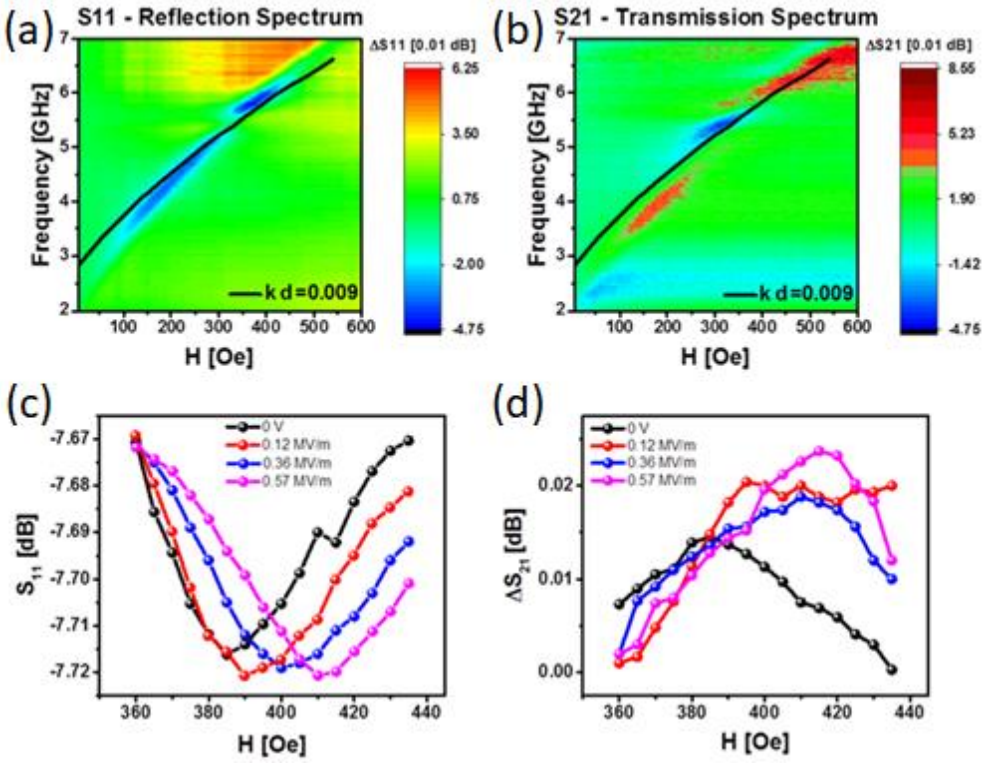

Figure 66 – Colormaps with frequency range from 2 to 7 GHz and magnetic field from 0 to 600 Oe. (a) S_{11} parameter. (b) S_{21} parameter. The black curves are results of fitting by equation (10) using parameters: $4\pi M_s$ = 7800 Oe, kd = 0.009. (c) Microwave reflection S_{11} as a function of the bias magnetic field at f = 6.0 GHz. The four curves of different colors show S_{11} variation at the applied electric field E: 0 MV/m, 0.12 MV/m, 0.36 MV/m, and 0.57 MV/m. The minima in the S_{11} spectra correspond to the microwave power absorption. (d) Transmission parameter S_{21} as a function of the bias magnetic field at f = 6.0 GHz. The four curves of different colors depict S_{21} parameter at the applied electric field E: 0 MV/m, 0.12 MV/m, 0.36 MV/m, and 0.57 MV/m. The maxima in the S_{21} spectra correspond to the spin wave propagation. [109] *Sci. Rep.* 8, 10867 (2018), with the permission of Springer Nature publishing under CC BY license, link: https://creativecommons.org/licenses/by/4.0/

`

The experimental results are shown in **Figure 66**. The red color in **Figure 66**(a) corresponds to the maximum reflection while the blue color depicts the region in the *f-H* space corresponding to the microwave absorption. The red color in **Figure 66**(b), meanwhile, corresponds to the maximum signal transmission. In **Figure 66**(c), the experimental data showing the change of the microwave reflection due to the applied electric field is presented. Similar to **Figure 64**, the applied electric field shifts the absorption peak towards a higher magnetic field. In **Figure 66**(d), the experimental data showing the change of the transmission between the antennas due to the applied electric field is presented. The maxima in the S_{21} spectra correspond to the spin wave propagation. The obtained shift towards higher frequency is consistent with the similar trend in S_{11} parameter. The application of an electric field *E* across the piezoelectric layer is equivalent to the change of the effective magnetic field H_{eff}.

Figure 67 shows the extracted experimental data demonstrating the change of the inductive voltage V_{out} as a function of the applied electric field *E*. An increase of the electric field strength is mathematically equivalent to the application of an external magnetic field, which makes spin wave propagation possible. The peak of the spin wave transmission corresponding to 1.5 mV output inductive voltage takes place around 0.3 MV/m of the applied electric field. The decrease of the output inductive voltage reflects the decrease of the spin wave amplitude as the system moves away from the spin wave resonance. The transmission decreases by more than 3 times compared to the maximum value by changing the electric field ± 0.3 MV/m. The blue curve in **Figure 67** shows the results of fitting using Lorentz line shape (i.e. $V_{out}(E)$ using $V_{out}(\max) = 1.64$ mV, and

`

E(max)= 0.264 MV/m). The results of fitting are in good qualitative agreement with the expected output characteristic shown in **Figure 62**(b).

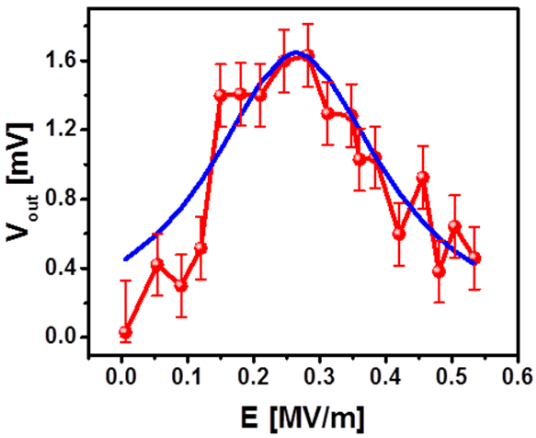

Figure 67 – Experimental data showing the output characteristics of the spin wave modulator. Red markers and red curve show the inductive voltage in mV produced by the propagating spin waves. The data are taken at the bias magnetic field of 390 Oe and the operational frequency *f* = 6.0 GHz. The blue curve shows the results of fitting by Lorentz lineshape. The distance between the excitation and detection antennas is 80 μm. [109] *Sci. Rep.* 8, 10867 (2018), with the permission of Springer Nature publishing under CC BY license, link: https://creativecommons.org/licenses/by/4.0/

4.2.2. Significance of the obtained results

In this section, a spin wave modulator was presented, and the operation of which is based on the stress-mediated coupling between piezoelectric and magnetostrictive materials. A relatively weak electric field E_{sw} (e.g. 0.6 MV/m for PMN-PT/Ni/Py device) is required to switch between the spin wave conducting and non-conducting regimes. The energy dissipated in the multiferroic element *E* can be estimated as follows:

$$E = \frac{1}{Q}\frac{CV^2}{2} = \frac{\varepsilon_0 \varepsilon S d_e}{2Q} E_{sw}^2 \qquad (25)$$

`

where C is the capacity of the multiferroic element, V is the voltage applied, Q is the quality factor of the piezoelectric oscillator, $\varepsilon_0 = 8.854 \times 10^{-12}\ \mathrm{F \cdot m^{-1}}$ is the electric constant, ε is the dielectric permittivity of the piezoelectric, S is the plate area, and d_e is the thickness of the piezoelectric layer. Assuming the switching electric field E_{sw} is constant, one can estimate energy dissipation in sub-micrometer size devices. Taking ε = 2000, S = 100 nm × 100 nm; d_e = 20nm, and Q = 1, the energy dissipated per one modulation is less than 10 aJ neglecting line losses and substrate clamping. As a result, the proposed modulator may be more efficient than the VCMA-based devices [116, 117] as it requires much weaker electric field for operation.

The further development of the spin wave modulator is mainly associated with the scaling down of the multiferroic element. One of the major questions is related to the effect of scaling to the switching electric field E_{sw} required for spin wave modulation. Scaling down the dimensions of the multiferroic element with constant E_{sw} would benefit its operation in all figures of merit. Moreover, it will be important to study the effect of the strain-mediated coupling on the different types of spin waves (e.g. BVMSW). In conclusion, the demonstration of the spin wave modulator shows a possible solution to the problems associated with a short spin diffusion length. The proposed magnetoelectric modulator can be utilized in spin-wave logic and memory devices by offering ultra-low power consumption and fast modulation speed.

`

Chapter 5. Summary

In order to achieve my research objectives, I have dedicated myself to conducting many experiments in spin waves studies as well as researching potential applications of spin waves. Below is a table of my preceding works [77, 80, 102, 109, 118-128]. These preceding works have attracted much attention from researchers who share similar interests in the spintronics field. As such, these published works are the recognition of my contribution to the magnonic community.

`

Publications	Magnetic Structures Explored	Obtained Results	Significance	My Contributions
#1 (2016) Parallel Read-Out and Database Search With Magnetic Holographic Memory (IEEE Trans. Magn.)	YIG four crosses with magnetic bits; ***t***: 3.6 μm	Collection of inductive voltages with spin wave propagates in both BVMSW and MSSW at ***f***: 4.165 GHz and ***H***: 760 Oe	Demonstrated practical feasibility of MHM and capabilities for parallel read-out and database search	Data extraction and analysis using MATLAB and Origin software
#2 (2016) Prime Factorization Using Magnonic Holographic Devices (J. of Appl. Phys.)	YIG double crosses ***t***: 3.6 μm $4\pi M_s$: 1750 Oe	Collection of S_{12} spectrum, spin wave propagates in both BVMSW and MSSW at ***f***: 4.165 GHz and ***H***: 760 Oe	Sped up prime factorization procedure for conventional digital computers using spin wave interference	Data extraction and analysis using MATLAB and Origin software
#3 (2016) Parallel Data Processing With Magnonic Holographic Co-Processor (IEEE ICRC)	YIG four crosses – 8 terminals ***t***: 3.6 μm	Correlation between the input phase patterns and the output inductive voltage. Spin waves generated through antennas at ***f***: 5.4 GHz	Presented experimental data on parallel data processing, with coding information into phase of propagating waves (wave superposition)	Data extraction and analysis using MATLAB and Origin software
#4 (2016) Magnonic Holographic Imaging of Magnetic Microstructures (Journal of MMM)	YIG cross with four Π shaped antennas; ***t***: 3.8 μm	Collection of S_{21} spectrum at ***f***: 3.442 GHz and ***H***: 627 Oe, with 2 phase shifters to create 3D images of objects in phase-voltage space	Demonstrated a novel technique for magnetic microstructures imaging and visualized them as 3D objects. Provided better spatial resolution than FMR	Characterized samples with SEM, VSM; performed experiments; data extraction and analysis in Origin
#5 (2016) Perpendicularly Magnetized YIG-Film Resonators and Waveguides With High Operating Power (AIP Advances)	YIG film, with resonators and waveguides ***t***: 30 μm	FVMSW excitations with collection of S_{11} (resonator) and S_{21} (waveguide) spectrums, ***f***: 1.8 to 5.1 GHz and ***H***: 2250 to 3600 Oe	Demonstrated the use of TIR phenomenon of FVMSW in metalized YIG films that lead to new design of resonators and waveguides	Performed experiments; data extraction and analysis in Origin
#6 (2017) Magnonic Interferometric Switch for Multi-Valued Logic Circuits (J. of Appl. Phys.)	YIG cross with four Π shaped antennas; ***t***: 3.8 μm	Output inductive voltage modulation by the phase difference between terminals. BVMSW and MSSW excitations, at ***f***: 4.095 GHz and ***H***: 798 Oe	On/Off ratio over 13 dB at room temperature. Noise density S_v/V^2 from output was 10^{-11} 1/Hz, useful for low-noise, low-power designs	Performed experiments; data extraction in MATLAB and analysis in Origin

`

#7 (2017) Spin Wave Interference in YIG Cross Junction (AIP Advances)	YIG cross with four Π shaped antennas; ***t***: 3.8 μm	Collection of S_{21} spectrums with spin waves interference of BVMSW and MSSW at ***f***: 4.095 GHz and ***H***: 798 Oe	On/Off ratio exceeded 30 dB for all directions of magnetic fields. Non-zero ***k*** overlap for BVMSW and MSSW	Device packaging; conducted experiments; data extraction in Origin
#8 (2017) A Magnetometer Based on a Spin Wave Interferometer (Scientific Reports)	YIG cross with waveguides ***ℓ***: 3.65 mm, ***w***: 650 μm; ***t***: 3.8 μm	Collection of S_{21} spectrum, at ***f***: 4.95 GHz and ***H***: 1074 Oe. Data: output inductive voltages with spin wave phase differences	Comparable sensitivity (attotesla) with SQUID. Has advantages of compactness, fast data acquisition, and wide temperature operating range	Device packaging; conducted experiments; data extraction in MATLAB and analysis in Origin
#9 (2017) Spin Wave Excitation in Sub-Micrometer Thick $Y_3Fe_5O_{12}$ Films Fabricated by Pulsed Laser Deposition on Garnet and Silicon Substrates: A Comparative Study (J. of Appl. Phys.)	YIG/GGG and YIG/Si films ***t***: 700 nm Micro-antennas have gap of 10, 50, and 500 μm	Spin wave spectroscopy to collect S_{11} (reflection) and S_{21} (transmission) spectrums, with ***f***: 0.5-7 GHz and ***H***: -2500 to +2500 Oe	Demonstrated spin wave excitation and propagation in YIG on Si substrate. Enabled integration of magnonic components with conventional electronic circuits	Device fabrication and packaging; conducted experiments; data extraction in MATLAB and analysis in Origin
#10 (2017) Brillouin-Mandelstam Spectroscopy of Standing Spin Waves in a Ferrite Waveguide (AIP Advances)	YIG film ***t***: 9.6 μm With two micro-antennas, ***w***: 100 μm	Spin wave spectroscopy to collect S_{21} and S_{12} spectrums, with ***f***: 6-6.5 GHz and ***H***: -2000 to +2000 Oe. BMS to collect spin wave signals (intensity) at ***f***: 6.16 GHz and ***H***: 1410 Oe	Presented BMS study of spin wave interference in YIG waveguide, and spin wave propagates distance of 7.5 mm. Contributed to remote control of spin currents	Device fabrication and packaging; conducted spin wave experiments; assisted in BMS measurements
#11 (2017) Effects of the Magnetic Field Variation on the Spin Wave Interference in a Magnetic Cross Junction (AIP Advances)	YIG cross with four Π shaped antennas ***t***: 3.8 μm $4\pi M_s$: 1750 Oe	Collection of S_{21} spectrums at ***f***: 3-6 GHz and ***H***: 750 to 1350 Oe. Magnetic field variation: collection of S_{21} spectrums at ***f***: 5.1 GHz and ***H***: 1140 Oe	High sensitivity of spin wave interference, 30 dB / 1 Oe. Switching between cons. and des. interference (≤ 1 Oe) had amplitude difference of 50 dB	Antennas fabrication and packaging; conducted experiments; data extraction in MATLAB and analysis in Origin
#12 (2018) Realization of Spin Wave Switch for Data Processing (AIP Advances)	YIG film ***t***: 42 μm Gold wires as antennas,	Collection of all S-parameter spectrums at ***f***: 3-6 GHz and ***H***: 600 to 1650 Oe. Collection of cons. and des. spin wave	Demonstrated spin wave switch with linear spin wave superposition as input and outputs non-linear inductive voltage.	Antennas fabrication and packaging; conducted experiments; data extraction

`

	24.5 μm thickness	signals at ***f***: 4.5 GHz and ***H***: 987 Oe	On/Off ratio exceeded 20 dB at room temperature	in MATLAB and analysis in Origin
#13 (2018) Reversible Magnetic Logic Gates Based on Spin Wave Interference (J. of Appl. Phys.)	YIG cross with four waveguides ***ℓ***: 3.65 mm, ***w***: 650 μm; ***t***: 3.8 μm	Spin wave spec. to collect S_{21} spectrums for inductive voltage detection with ***H***: 1107 and 1131 Oe (magnetic field applied through cross at 45˚)	Presented the experimental data of magnetic reversible logic gates using spin wave interference. On/Off ratio exceeded 45 dB at room temp. Low energy per operation (< ***kT***)	Antennas fabrication and packaging; conducted experiments; data extraction in MATLAB and analysis in Origin
#14 (2018) Magnetoelectric Spin Wave Modulator Based on Synthetic Multiferroic Structure (Scientific Reports)	Ni and Ni/Py films ***t***: 30 nm (Ni) 30 nm (Py)	Spin wave spec. to collect S_{11} and S_{21} spectrums, ***f***: 0.5-9 GHz and ***H***: -2400 to +2400 Oe. Collection of inductive voltages vs. applied ***E*** fields	Demonstrated a spin wave modulator, over 300% modulation depth with 80 μm from excitation port. Controlled spin wave bus with applied ***E*** field. Ultra-low power dissipation and fast modulation speed (at room temp.)	Sample charact. with VSM; device fabrication and packaging; conducted experiments; data extraction in MATLAB and analysis in Origin
#15 (2018) Spin Wave Excitation and Propagation in Py Nanowire Structure (AIP Advances) (Submitted)	Py film and nanowires ***ℓ***: 50 μm, ***w***: 230 nm, ***t***: 60 nm; SiO_2 (80 nm) for isolation between Py and four micro-antennas	Spin wave spec. to collect all S-parameter spectrums, ***f***: 1.5-7.5 GHz and ***H***: -600 to +600 Oe. Active ring setup: collection of S21 spectrums, ***f***: 1.5-2.7 GHz and ***H***: -150 to +150 Oe. (Sensitivity improvement)	Domain structures observed, useful for applications. Presented spin wave excitation and propagation in Py nanowires, and non-reciprocity effect. Demonstrated a complementary technique for spin wave studies	Sample charact. with AFM, MFM; device fabrication and packaging; conducted experiments; data extraction in MATLAB and analysis in Origin

Table 3 – Published and submitted works.

Deeper understanding and important features of spin wave mechanisms in micro- and nanostructures, in addition to the exploration of new materials for spintronics, have in this dissertation revealed themselves to be important tasks. Throughout this dissertation, I have investigated spin wave excitation and propagation in both ferrimagnetic and ferromagnetic materials. In addition, I have extended these studies to

`

the level of spin wave interference and control in novel structural design. The obtained results can lead to more efficient nanoscale of spin wave excitation, propagation, and control, with benefits for various practical applications.

Spin wave spectroscopy is one of the remarkable techniques that I used frequently for my research. It possesses several dominant features, such as providing coherent excitation, having high sensitivity, allowing phase control, having high frequency resolution, and being highly suitable for magnon logic. As a result, it was shown that spin wave spectroscopy provides high signal resolution and introduces wave phases for advanced Boolean/non-Boolean logics. Micro- and nanostructures are the building blocks for spintronics. Through a fundamental understanding of fabrication processes, I have optimized various methods and techniques in order to construct state of the art spintronics.

In conclusion, the results presented in this dissertation demonstrate the most recent experimental data on spin wave excitation and detection obtained in magnetic micro- and nano-structures. These results are important for the development of a new generation of memory and logic devices with functional capabilities far beyond the scaled CMOS.

`

Chapter 6. References

1. Chumak, A.V., et al., *Magnon spintronics.* Nature Physics, 2015. **11**(6): p. 453-461.

2. Damon, R.W. and J.R. Eshbach, *Magnetostatic modes of a ferromagnet slab.* Journal of Physics and Chemistry of Solids, 1961. **19**(3-4): p. 308-320.

3. Owens, J.M., J.H. Collins, and R.L. Carter, *SYSTEM APPLICATIONS OF MAGNETOSTATIC WAVE DEVICES.* Circuits Systems and Signal Processing, 1985. **4**(1-2): p. 317-334.

4. Adam, J.D., *ANALOG SIGNAL-PROCESSING WITH MICROWAVE MAGNETICS.* Proceedings of the Ieee, 1988. **76**(2): p. 159-170.

5. Serga, A.A., A.V. Chumak, and B. Hillebrands, *YIG magnonics.* Journal of Physics D-Applied Physics, 2010. **43**(26): p. 16.

6. Minno, M. *Magnetism Lab.* [cited 2018 May 20]; Available from: http://www.magnet.okayama-u.ac.jp/sjis_index.html.

7. Kalinikos, B.A., *Excitation of propagating spin waves in ferromagnetic films.* IEE Proceedings-H Microwaves, Optics, and Antennas, 1980. **127**(1): p. 4-10.

8. Kalinikos, B.A. and A.N. Slavin, *Theory of dipole-exchange spin wave spectrum for ferromagnetic films with mixed exchange boundary conditions.* Journal of Physics C-Solid State Physics, 1986. **19**(35): p. 7013-7033.

9. Chumak, A.V., A.A. Serga, and B. Hillebrands, *Magnonic crystals for data processing.* Journal of Physics D-Applied Physics, 2017. **50**(24): p. 20.

10. Schneider, T., et al., *Phase reciprocity of spin-wave excitation by a microstrip antenna.* Physical Review B, 2008. **77**(21): p. 5.

11. Au, Y., et al., *Resonant microwave-to-spin-wave transducer.* Applied Physics Letters, 2012. **100**(18): p. 5.

12. Au, Y., et al., *Excitation of propagating spin waves with global uniform microwave fields.* Applied Physics Letters, 2011. **98**(12): p. 3.

13. Bracher, T., et al., *Parallel parametric amplification of coherently excited propagating spin waves in a microscopic $Ni_{81}Fe_{19}$ waveguide.* Applied Physics Letters, 2014. **104**(20): p. 5.

`

14. Chumak, A.V., et al., *Bose-Einstein condensation of magnons under incoherent pumping.* Physical Review Letters, 2009. **102**(18): p. 4.

15. Kalarickal, S.S., et al., *Ferromagnetic resonance linewidth in metallic thin films: Comparison of measurement methods.* Journal of Applied Physics, 2006. **99**(9): p. 7.

16. Kennewell, K.J., et al., *Interpretation of magnetisation dynamics using inductive magnetometry in thin films.* Surface Science, 2007. **601**(24): p. 5766-5769.

17. Ordonez-Romero, C.L., et al., *Mapping of spin wave propagation in a one-dimensional magnonic crystal.* Journal of Applied Physics, 2016. **120**(4): p. 6.

18. Smith, K.R., et al., *Spin wave propagation in spatially nonuniform magnetic fields.* Journal of Applied Physics, 2008. **104**(4): p. 6.

19. Demidov, V.E. and S.O. Demokritov, *Magnonic waveguides studied by microfocus Brillouin Light Scattering.* IEEE Transactions on Magnetics, 2015. **51**(4): p. 15.

20. Chumak, A.V., et al., *Spin-wave propagation in a microstructured magnonic crystal.* Applied Physics Letters, 2009. **95**(26): p. 3.

21. Bauer, H.G., et al., *Coupling of spinwave modes in wire structures.* Applied Physics Letters, 2014. **104**(10): p. 4.

22. Allwood, D.A., et al., *Magneto-optical Kerr effect analysis of magnetic nanostructures.* Journal of Physics D-Applied Physics, 2003. **36**(18): p. 2175-2182.

23. Chumak, A.V., et al., *Direct detection of magnon spin transport by the inverse spin Hall effect.* Applied Physics Letters, 2012. **100**(8): p. 3.

24. Bass, J. and W.P. Pratt, *Spin-diffusion lengths in metals and alloys, and spin-flipping at metal/metal interfaces: an experimentalist's critical review.* Journal of Physics-Condensed Matter, 2007. **19**(18): p. 41.

25. Demidov, V.E., S. Urazhdin, and S.O. Demokritov, *Direct observation and mapping of spin waves emitted by spin-torque nano-oscillators.* Nature Materials, 2010. **9**(12): p. 984-988.

26. Cornelissen, L.J., et al., *Long-distance transport of magnon spin information in a magnetic insulator at room temperature.* Nature Physics, 2015. **11**(12): p. 1022-1027.

`

27. Collet, M., et al., *Generation of coherent spin-wave modes in yttrium iron garnet microdiscs by spin-orbit torque.* Nature Communications, 2016. **7**: p. 8.

28. Demidov, V.E., et al., *Magnetic nano-oscillator driven by pure spin current.* Nature Materials, 2012. **11**(12): p. 1028-1031.

29. Kajiwara, Y., et al., *Transmission of electrical signals by spin-wave interconversion in a magnetic insulator.* Nature, 2010. **464**(7286): p. 262-U141.

30. Zografos, O., et al., *Design and Benchmarking of Hybrid CMOS-Spin Wave Device Circuits Compared to 10nm CMOS*. 2015 Ieee 15th International Conference on Nanotechnology. 2015, New York: Ieee. 686-689.

31. Rugar, D., et al., *Single spin detection by magnetic resonance force microscopy.* Nature, 2004. **430**(6997): p. 329-332.

32. Stowe, T.D., et al., *Attonewton force detection using ultrathin silicon cantilevers.* Applied Physics Letters, 1997. **71**(2): p. 288-290.

33. Mozyrsky, D., et al., *Theory of spin relaxation in magnetic resonance force microscopy.* Applied Physics Letters, 2003. **82**(8): p. 1278-1280.

34. Mamin, H.J., et al., *Detection and manipulation of statistical polarization in small spin ensembles.* Physical Review Letters, 2003. **91**(20): p. 4.

35. Klein, O., et al., *Ferromagnetic resonance force spectroscopy of individual submicron-size samples.* Physical Review B, 2008. **78**(14): p. 17.

36. Bauer, G.E.W., et al., *Nanoscale magnetic heat pumps and engines.* Physical Review B, 2010. **81**(2): p. 11.

37. Jungfleisch, M.B., et al., *Heat-induced damping modification in yttrium iron garnet/platinum hetero-structures.* Applied Physics Letters, 2013. **102**(6): p. 4.

38. An, T., et al., *Unidirectional spin-wave heat conveyer.* Nature Materials, 2013. **12**(6): p. 549-553.

39. Rhoads, J.F., S.W. Shaw, and Asme, *THE EFFECTS OF NONLINEARITY ON PARAMETRIC AMPLIFIERS*. Detc2008: Proceedings of the Asme International Design Engineering Technical Conference and Computers and Information in Engineering Conference , Vol 4. 2009, New York: Amer Soc Mechanical Engineers. 593-597.

`

40. Kos, A.B., T.J. Silva, and P. Kabos, *Pulsed inductive microwave magnetometer.* Review of Scientific Instruments, 2002. **73**(10): p. 3563-3569.

41. Madami, M., et al., *Application of Microfocused Brillouin Light Scattering to the Study of Spin Waves in Low-Dimensional Magnetic Systems*, in *Solid State Physics, Vol 63*, R.E. Camley and R.L. Stamps, Editors. 2012, Elsevier Academic Press Inc: San Diego. p. 79-150.

42. Demokritov, S.O., B. Hillebrands, and A.N. Slavin, *Brillouin light scattering studies of confined spin waves: linear and nonlinear confinement.* Physics Reports-Review Section of Physics Letters, 2001. **348**(6): p. 441-489.

43. Stiles, M.D. and A. Zangwill, *Anatomy of spin-transfer torque.* Physical Review B, 2002. **66**(1): p. 14.

44. Covington, M., T.M. Crawford, and G.J. Parker, *Time resolved measurement of propagating spin waves in ferromagnetic thin films.* Physical Review Letters, 2002. **89**(23): p. 4.

45. Silva, T.J., et al., *Inductive measurement of ultrafast magnetization dynamics in thin-film Permalloy.* Journal of Applied Physics, 1999. **85**(11): p. 7849-7862.

46. Jamali, M., et al., *Spin wave nonreciprocity for logic device applications.* Scientific Reports, 2013. **3**: p. 5.

47. Pearson, G.L. and J. Bardeen, *ELECTRICAL PROPERTIES OF PURE SILICON AND SILICON ALLOYS CONTAINING BORON AND PHOSPHORUS.* Physical Review, 1949. **75**(5): p. 865-883.

48. Jungfleisch, M.B., et al., *Large spin-wave bullet in a ferrimagnetic insulator driven by the spin Hall effect.* Physical Review Letters, 2016. **116**(5): p. 6.

49. Cherepov, S., et al., *Electric-field-induced spin wave generation using multiferroic magnetoelectric cells.* Applied Physics Letters, 2014. **104**(8): p. 5.

50. Khitun, A. and K.L. Wang, *Non-volatile magnonic logic circuits engineering.* Journal of Applied Physics, 2011. **110**(3): p. 11.

51. Wolf, S.A., et al., *Spintronics: A spin-based electronics vision for the future.* Science, 2001. **294**(5546): p. 1488-1495.

52. Jaeger, R.C., *Introduction to microelectronic fabrication*. 2 ed. Vol. 5. 2002: Prentice Hall.

`

53. Lamrani, S., et al., *Morphology, structure and magnetic study of permalloy films electroplated on silicon nanowires.* Journal of Magnetism and Magnetic Materials, 2015. **396**: p. 263-267.

54. Heywang, W. and K.H. Zaininger, *Silicon: the semiconductor material*. 2004, Berlin, Heidelberg: Springer-Verlag.

55. Schneider, T., et al., *Realization of spin-wave logic gates.* Applied Physics Letters, 2008. **92**(2): p. 3.

56. Chiang, W.C., et al., *FMR studies Of Y3Fe5O12/Gd3Ga5O12 (YIG/GGG) superlattices and YIG thin films.* Journal of Magnetism and Magnetic Materials, 2002. **239**(1-3): p. 332-334.

57. Shao, D.B. and S.C. Chen, *Surface-plasmon-assisted nanoscale photolithography by polarized light.* Applied Physics Letters, 2005. **86**(25): p. 3.

58. *Center for Nanoscale Science and Engineering*. [cited 2018 May 20]; Available from: http://www.cnse.ucr.edu/.

59. Tseng, A.A., et al., *Electron beam lithography in nanoscale fabrication: recent development.* Ieee Transactions on Electronics Packaging Manufacturing, 2003. **26**(2): p. 141-149.

60. Ghandhi, S.K., *VLSI fabrication principles: silicon and gallium arsenide*. 2 ed. 1994, New York: Wiley-Interscience.

61. Shul, R.J., et al., *Inductively coupled plasma etching of GaN.* Applied Physics Letters, 1996. **69**(8): p. 1119-1121.

62. Betancourt, T. and L. Brannon-Peppas, *Micro- and nanofabrication methods in nanotechnological medical and pharmaceutical devices.* International Journal of Nanomedicine, 2006. **1**(4): p. 483-495.

63. Gao, H.Y., et al., *Improvement of the performance of GaN-based LEDs grown on sapphire substrates patterned by wet and ICP etching.* Solid-State Electronics, 2008. **52**(6): p. 962-967.

64. Inc., A.I. *Evaporation Systems*. [cited 2018 May 5]; Available from: http://www.ajaint.com/what-is-e-beam-evaporation.html.

`

65. Monaco, G. *Coating technology: evaporation vs sputtering – Satisloh, Italy*. [cited 2018 May 5]; Available from: http://www.satisloh.com/fileadmin/contents/Whitepaper/Evaporation-vs-Sputtering-Coating_EN.pdf.

66. Instruments, A.S. *SEM & imaging: the applications and practical uses of scanning electron microscopes*. [cited 2018 May 8]; Available from: https://www.atascientific.com.au/sem-imaging-applications-practical-uses-scanning-electron-microscopes/.

67. Foner, S., *VERSATILE AND SENSITIVE VIBRATING-SAMPLE MAGNETOMETER.* Review of Scientific Instruments, 1959. **30**(7): p. 548-557.

68. Foner, S., *VIBRATING SAMPLE MAGNETOMETER.* Review of Scientific Instruments, 1956. **27**(7): p. 548-548.

69. Cryotronics, L.S. *7400-S Series VSM*. [cited 2018 May 8]; Available from: https://www.lakeshore.com/products/Vibrating-Sample-Magnetometer/7400-S-Series-VSM/Pages/Overview.aspx.

70. Rugar, D. and P. Hansma, *ATOMIC FORCE MICROSCOPY.* American Institute of Physics - Physics Today, 1990. **43**(10): p. 23-30.

71. Thornton, J., et al., *SPM training notebook*. E ed. 2003: Veeco Instruments Inc.

72. BioImaging, T. *Atomic force microscopy – Turku BioImaging*. [cited 2018 May 10]; Available from: http://www.bioimaging.fi/methods/atomic-force-microscopy/.

73. Vesna, V. *Atomic force microscopy*. [cited 2018 May 10]; Available from: http://artsci.ucla.edu/BlueMorph/contact.html.

74. NanoWorld. *High speed atomic force microscopy*. [cited 2018 May 10]; Available from: http://www.nanoworld.com/blog/more-papers-on-high-speed-atomic-force-microscopy-list-of-references-updated/.

75. *AFM image quality*. [cited 2018 May 10]; Available from: http://www.nanophys.kth.se/nanophys/facilities/nfl/afm/icon/bruker-help/Content/SPM%20Training%20Guide/Atomic%20Force%20Microscopy%20(AFM)/AFM%20Image%20Quality.htm.

76. Neusser, S. and D. Grundler, *Magnonics: Spin Waves on the Nanoscale.* Advanced Materials, 2009. **21**(28): p. 2927-2932.

`

77. Balinskiy, M., et al., *Spin wave interference in YIG cross junction.* Aip Advances, 2017. **7**(5): p. 5.

78. Kruglyak, V.V., S.O. Demokritov, and D. Grundler, *Magnonics.* Journal of Physics D-Applied Physics, 2010. **43**(26): p. 14.

79. Gurevich, A.G. and G.A. Melkov, *Magnetization Oscillations and Waves*. 1996, New York: CRC Press Inc.

80. Balinskiy, M., et al., *Spin wave excitation in sub-micrometer thick Y3Fe5O12 films fabricated by pulsed laser deposition on garnet and silicon substrates: A comparative study.* Journal of Applied Physics, 2017. **122**(12): p. 6.

81. Kumar, N., et al., *Magnetic properties of pulsed laser ablated YIG thin films on different substrates.* Journal of Magnetism and Magnetic Materials, 2004. **272**: p. E899-E900.

82. Goto, T., M.C. Onbasli, and C.A. Ross, *Magneto-optical properties of cerium substituted yttrium iron garnet films with reduced thermal budget for monolithic photonic integrated circuits.* Optics Express, 2012. **20**(27): p. 28507-28517.

83. Sung, S.Y., X.Y. Qi, and B.J.H. Stadler, *Integrating yttrium iron garnet onto nongarnet substrates with faster deposition rates and high reliability.* Applied Physics Letters, 2005. **87**(12): p. 3.

84. Yang, Q.H., et al., *Effects of off-stoichiometry and density on the magnetic and magneto-optical properties of yttrium iron garnet films by magnetron sputtering method.* Journal of Applied Physics, 2010. **108**(7): p. 5.

85. Yang, Q.H., et al., *Effect of post-annealing on the magnetic properties of Bi : YIG film by RF magnetron sputtering on si substrates.* Ieee Transactions on Magnetics, 2007. **43**(9): p. 3652-3655.

86. Goto, T., et al., *Vacuum annealed cerium-substituted yttrium iron garnet films on non-garnet substrates for integrated optical circuits.* Journal of Applied Physics, 2013. **113**(17): p. 3.

87. Guo, X., et al., *Growth and characterization of yttrium iron garnet films on Si substrates by Chemical Solution Deposition (CSD) technique.* Journal of Alloys and Compounds, 2016. **671**: p. 234-237.

88. Stadler, B., et al., *Integration of magneto-optical garnet films by metal-organic chemical vapor deposition.* Ieee Transactions on Magnetics, 2002. **38**(3): p. 1564-1567.

`

89. Stognij, A.I., et al., *Growth and spin-wave properties of thin Y3Fe5O12 films on Si substrates.* Journal of Applied Physics, 2015. **118**(2): p. 7.

90. Onbasli, M.C., et al., *Pulsed laser deposition of epitaxial yttrium iron garnet films with low Gilbert damping and bulk-like magnetization.* Apl Materials, 2014. **2**(10): p. 8.

91. Maksymov, I.S. and M. Kostylev, *Broadband stripline ferromagnetic resonance spectroscopy of ferromagnetic films, multilayers and nanostructures.* Physica E-Low-Dimensional Systems & Nanostructures, 2015. **69**: p. 253-293.

92. Demidov, V.E., et al., *Excitation of coherent propagating spin waves by pure spin currents.* Nature Communications, 2016. **7**: p. 6.

93. Khitun, A. and K.L. Wang, *Nano scale computational architectures with Spin Wave Bus.* Superlattices and Microstructures, 2005. **38**(3): p. 184-200.

94. de Loubens, G., et al., *Magnetic resonance studies of the fundamental spin-wave modes in individual submicron Cu/NiFe/Cu perpendicularly magnetized disks.* Physical Review Letters, 2007. **98**(12): p. 4.

95. Wintz, S., et al., *Magnetic vortex cores as tunable spin-wave emitters.* Nature Nanotechnology, 2016. **11**(11): p. 948-953.

96. Chang, W., et al., *Hard gap in epitaxial semiconductor-superconductor nanowires.* Nature Nanotechnology, 2015. **10**(3): p. 232-236.

97. Chan, C.K., et al., *High-performance lithium battery anodes using silicon nanowires.* Nature Nanotechnology, 2008. **3**(1): p. 31-35.

98. Liu, Z., et al., *Flexible electronics based on inorganic nanowires.* Chemical Society Reviews, 2015. **44**(1): p. 161-192.

99. Zhang, A.Q., G.F. Zheng, and C.M. Lieber, *Emergence of Nanowires*, in *Nanowires: Building Blocks for Nanoscience and Nanotechnology*. 2016, Springer International Publishing Ag: Cham. p. 1-13.

100. Gertz, F., et al., *Magnonic Holographic Read-Only Memory.* Ieee Magnetics Letters, 2016. **7**: p. 4.

101. Gong, S., et al., *A wearable and highly sensitive pressure sensor with ultrathin gold nanowires.* Nature Communications, 2014. **5**: p. 8.

`

102. Gutierrez, D., et al., *Magnonic holographic imaging of magnetic microstructures.* Journal of Magnetism and Magnetic Materials, 2017. **428**: p. 348-356.

103. Terris, B.D. and T. Thomson, *Nanofabricated and self-assembled magnetic structures as data storage media.* Journal of Physics D-Applied Physics, 2005. **38**(12): p. R199-R222.

104. Yadollahpour, A., *Magnetic Nanoparticles in Medicine: A Review of Synthesis Methods and Important Characteristics.* Oriental Journal of Chemistry, 2015. **31**: p. 271-277.

105. Baker, K.F., *A REVIEW OF MAGNETIC-BUBBLE MEMORIES AND THEIR APPLICATIONS.* Radio and Electronic Engineer, 1981. **51**(3): p. 105-116.

106. Tumanski, S., *Modern magnetic field sensors – a review.* Przeglad Elektrotechniczny, 2013. **89**(10): p. 1-12.

107. Kim, T. and T. Hyeon, *Applications of inorganic nanoparticles as therapeutic agents.* Nanotechnology, 2014. **25**(1): p. 14.

108. Gertz, F., et al., *Magnonic Holographic Memory.* Ieee Transactions on Magnetics, 2015. **51**(4): p. 5.

109. Balinskiy, M., et al., *Magnetoelectric Spin Wave Modulator Based On Synthetic Multiferroic Structure.* Scientific Reports, 2018. **8**: p. 10.

110. Smolenskii, G.A. and I.E. Chupis, *Ferroelectromagnets.* Soviet Physics - Uspekhi, 1982. **25**: p. 475-493.

111. Zheng, H., et al., *Multiferroic BaTiO3-CoFe2O4 nanostructures.* Science, 2004. **303**(5658): p. 661-663.

112. Eerenstein, W., N.D. Mathur, and J.F. Scott, *Multiferroic and magnetoelectric materials.* Nature, 2006. **442**(7104): p. 759-765.

113. Landau, L.D. and E.M. Lifshitz, *Theory of the dispersion of magnetic permeability in ferromagnetic bodies.* Phys. Z. Sowietunion, 1935. **8**.

114. Gilbert, T.L., *A Lagrangian formulation of the gyromagnetic equation of the magnetic field.* Physical Review, 1955. **100**: p. 1243.

115. Kim, Y.K. and T.J. Silva, *Magnetostriction characteristics of ultrathin permalloy films.* Applied Physics Letters, 1996. **68**(20): p. 2885-2886.

`

116. Verba, R., et al., *Excitation of propagating spin waves in ferromagnetic nanowires by microwave voltage-controlled magnetic anisotropy.* Scientific Reports, 2016. **6**: p. 9.

117. Chen, Y.J., et al., *Parametric Resonance of Magnetization Excited by Electric Field.* Nano Letters, 2017. **17**(1): p. 572-577.

118. Gertz, F., et al., *Magnonic holographic memory update.* IEEE Transactions on Magnetics - Conference, 2016.

119. Gertz, F., et al., *Parallel Read-Out and Database Search With Magnonic Holographic Memory.* Ieee Transactions on Magnetics, 2016. **52**(7): p. 4.

120. Khivintsev, Y., et al., *Prime factorization using magnonic holographic devices.* Journal of Applied Physics, 2016. **120**(12): p. 6.

121. Balynsky, M., et al., *Parallel Data Processing With Magnonic Holographic Co-Processor*. 2016 Ieee International Conference on Rebooting Computing. 2016, New York: Ieee.

122. Balinskiy, M., et al., *Perpendicularly magnetized YIG-film resonators and waveguides with high operating power.* Aip Advances, 2017. **7**(5): p. 6.

123. Balynsky, M., et al., *Magnonic interferometric switch for multi-valued logic circuits.* Journal of Applied Physics, 2017. **121**(2): p. 12.

124. Balynsky, M., et al., *A Magnetometer Based on a Spin Wave Interferometer.* Scientific Reports, 2017. **7**: p. 11.

125. Balinskiy, M., et al., *Brillouin-Mandelstam spectroscopy of standing spin waves in a ferrite waveguide.* Aip Advances, 2018. **8**(5): p. 5.

126. Balynskiy, M., et al., *Effects of the magnetic field variation on the spin wave interference in a magnetic cross junction.* Aip Advances, 2018. **8**(5): p. 5.

127. Balinskiy, M., H. Chiang, and A. Khitun, *Realization of spin wave switch for data processing.* Aip Advances, 2018. **8**(5): p. 5.

128. Balynskiy, M., et al., *Reversible magnetic logic gates based on spin wave interference.* Journal of Applied Physics, 2018. **123**(14): p. 9.